Non-linear x-ray diffraction from ferromagnetic thin-films

vorgelegt von
Diplom-Ingenieur
Michael Schneider

von der Fakultät II - Mathematik und Naturwissenschaften
der Technischen Universität Berlin
zur Erlangung des akademischen Grades
Doktor der Naturwissenschaften
– Dr. rer. nat. –

genehmigte Dissertation

Promotionsausschuss:

Vorsitzender: Prof. Dr. Mario Dähne
Gutachter: Prof. Dr. Stefan Eisebitt
Gutachter: Prof. Dr. Olav Hellwig

Tag der wissenschaftlichen Aussprache: 04. September 2018

Berlin 2019

Für A. S.

Contents

Abstract xi

Zusammenfassung xiii

Preface xv

I. Fundamentals 1

1. Introduction 3

2. Methods 9
- 2.1. Overview 9
- 2.2. Diffraction geometry 9
- 2.3. XMCD contrast 10
- 2.4. General experimental setup 13
- 2.5. Diffraction setup at the FERMI FEL 13
  - 2.5.1. Time structure of the FEL pulse at FERMI 15
  - 2.5.2. Wave-front sensing 15
  - 2.5.3. Ablation imprints 16
- 2.6. Sample Fabrication 19
  - 2.6.1. Sputter deposition 19
  - 2.6.2. Focused ion beam milling 19
- 2.7. Numerical simulations of the diffracted field 20
  - 2.7.1. Exit-wave and illumination function 21
  - 2.7.2. Fraunhofer diffraction 22
  - 2.7.3. Free-space propagation 22

II. In-situ fluence monitoring 25

3. Influence of the spatial fluence distribution 27

4. Development of the grating monitors 29
- 4.1. Derivation of the distorted grating formula 29
- 4.2. Relationship between grating design and resolution limits 31
  - 4.2.1. Relationship to zone-plates 31
  - 4.2.2. Fraunhofer simulations on Fresnel- and hyperbolic gratings 33

4.2.3. Zone-plate perspective . . . 33
4.2.4. Grating perspective . . . 37
4.3. Aberrations . . . 38
4.3.1. In the near-field . . . 38
4.3.2. Geometric Distortion . . . 39

5. Experimental Results **43**
5.1. Grating fabrication . . . 43
5.2. Synchrotron experiments . . . 43
5.2.1. Matching the diffracted intensities . . . 43
5.2.2. Aperture-defined illumination profiles . . . 44
5.2.3. Large area segmented gratings . . . 46
5.2.4. Interleaved gratings with spatially allocatable diffraction . . . 47
5.3. In-situ fluence monitoring of FEL pulses . . . 49

6. Outlook and Summary **55**
6.1. Applicability at higher photon energies . . . 55
6.2. Summary . . . 55

III. Fluence-dependent diffraction **57**

7. XMCD diffraction from magnetic domains **59**
7.1. Experiment description . . . 60
7.2. Experimental Results . . . 61
7.2.1. Diffraction image features and analysis . . . 61
7.2.2. Non-linearity of the XMCD signal . . . 65
7.3. Spatial fluence distribution in the sample plane . . . 66
7.3.1. Obtaining the spatial fluence distribution . . . 68
7.3.2. Sample acceptance . . . 68
7.3.3. Definition of the fluence axis . . . 70
7.4. Phenomenological model of the non-linear XMCD diffraction cross-section 75
7.4.1. Sample description . . . 76
7.4.2. FEL pulse propagation . . . 77
7.4.3. Influence of the model parameters . . . 78
7.4.4. Role of the spatial fluence distribution . . . 81
7.5. Modeling the experimental data . . . 82
7.5.1. Pulse length variation . . . 84
7.6. Summary . . . 86

8. Fluence dependent absorption in Cobalt **89**
8.1. Experiment description . . . 90
8.2. Diffraction image evaluation . . . 90
8.3. Spatial fluence distribution . . . 92

8.4. Fluence dependence of the grating diffraction 93
8.5. Summary 95

IV. Summary and Outlook **97**

A. Source code of the demagnetization model **103**

List of Figures

2.1. Diffraction geometry and coordinate systems in the sample and detector plane. 11
2.2. Magnetic domains in a multi-layer sample. 12
2.3. Schematic layout of an XUV and soft x-ray diffraction experiment. 14
2.4. Wave-front sensor measurement 16
2.5. Spatial fluence distribution from ablation imprints. 18
2.6. Schematic of the simulation process. 22
2.7. Near-field propagation of a double slit. 24

3.1. Examples of spatial fluence distribution estimates. 28

4.1. Experiment geometry and sample design. 30
4.2. Schematic evolution of our grating design from regular gratings. 30
4.3. Grating monitors as zone-plate segments. 32
4.4. Simulated Fraunhofer diffraction of Fresnel- and hyperbolic gratings. . . . 34
4.5. Simulation of the object plane shift along the propagation axis. 36
4.6. Resolution estimate in the grating picture. 37
4.7. Near-field evolution of the grating diffraction. 40

5.1. Topography of the fabricated gratings. 44
5.2. Diffraction images with magnetic and grating diffraction. 45
5.3. Fluence maps of aperture-defined illuminations. 47
5.4. Diffraction and scanning electron microscopy (SEM) image of a large segmented grating. 48
5.5. Sketch of a fluence mapping experiment with distinguishable gratings. . . 48
5.6. Spatial fluence map from tiled gratings. 50
5.7. Single- and multi-shot fluence distributions. 51
5.8. Map of the spatial jitter. 52
5.9. Single-shot spatial fluence distributions along the beam propagation axis. 53

7.1. Schematic of the sample layer structure. 60
7.2. Example single-shot diffraction images. 62
7.3. Diffraction image evaluation. 63
7.4. FEL Shot-energy dependence of the grating diffraction cross-section. . . . 65
7.5. Shot-energy dependence of the X-ray magnetic circular dichroism (XMCD) diffraction cross-section. 66
7.6. Distorted spatial fluence map in the diffraction images. 67
7.7. Spatial fluence distribution during first experiment. 69

7.8. Determining the sample acceptance from membrane damage. 71
7.9. Definition of the nominal fluence. 72
7.10. Spatial fluence distributions and average fluence conversion factors. 74
7.11. Fluence ordering of the measured diffraction cross-sections. 75
7.12. Fluence dependence of the XMCD diffraction cross-section 76
7.13. Model components for ultrafast demagnetization during the FEL pulse . . 78
7.14. Temporal superposition of demagnetization curves in a single sample slice. 79
7.15. Simulated magnetization profile. 80
7.16. Influence of the different model parameters. 81
7.17. Influence of the spatial fluence distribution on the fluence dependence of the XMCD signal. 82
7.18. Fit of the demagnetization model with individual fluence information. . . 83
7.19. Demagnetization model fit using nominal fluence distributions. 85

8.1. Experiment and sample design to detect stimulated emission 91
8.2. Diffraction images from a double-grating sample. 92
8.3. Spatial fluence distribution in the sample plane 94
8.4. Diffracted single-shot fluence maps of front- and backside grating. 95
8.5. Diffraction cross-section ratios of front- and backside grating. 96
8.6. Schematic sketch of a single-shot measurement of fluence-dependent absorption. 102
8.7. Example calculation for a single-shot absorption cross-section measurement. 102

Acronyms

AFM atomic force microscopy. 9, 16, 17, 42, 57, 65–67, 90

CCD charge-coupled device. 12–15, 41, 43, 59, 61, 62, 90, 91, 93

DC direct current. 9, 18, 58
DiProI Diffraction and Projection Imaging. 13–15, 45, 54, 57, 62

FEL free-electron laser. xi, xii, 3–6, 9, 11, 13–18, 27, 41, 45, 48, 51, 54, 57–66, 68, 71, 73–84, 87, 88, 90, 91, 94, 97–99
FERMI "Free Electron laser Radiation for Multidisciplinary Investigations". 9, 14, 15, 45, 54, 57, 82, 84
FFT fast Fourier-transform. 21
FIB focused ion beam. 9, 18, 19, 41, 44, 45, 58, 62, 88, 89, 91, 98
FLASH Free-Electron Laser in Hamburg. 6, 50
FWHM full width at half maximum. 33, 34, 49, 75, 76, 82, 84, 100

GMD gas monitor detector. 14, 59, 61–63, 73, 80

HHG high-harmonic generation. 3, 4
HV high vacuum. 5, 12

IR infra-red. 14

KB Kirkpatrick-Baez. 5, 13, 14, 51

LCLS Linear Coherent Light Source. 6, 50

MFM magnetic force microscopy. 9, 12
MOKE magneto-optical Kerr effect. 82

PMA perpendicular magnetic anisotropy. 11, 12
PMMA poly(methyl methacrylate). 65, 67

RF radio frequency. 9, 18
ROI region of interest. 59, 61

SASE self-amplified spontaneous emission. 5, 50
SEM scanning electron microscopy. vii, 9, 45–47, 57, 65, 66, 68, 90, 100
SNR signal-to-noise ratio. 41, 43
SRIM "Stopping and Range of Ions in Matter". 19

UV ultra-violet. 5, 59

WFS wave-front sensor. 14, 15, 54, 57, 65–67, 70, 72, 79, 80, 90–92

XMCD X-ray magnetic circular dichroism. vii, xi, 6, 11, 41–43, 47, 57, 60, 61, 63, 64, 73, 75–80, 82–85, 87, 88, 94, 97, 98

XUV extreme ultra-violet. xi, xii, 3–7, 9, 11–14, 16, 19, 33, 41, 57, 58, 73, 74, 77, 82, 84, 87, 97–99

Abstract

In this thesis, fluence-dependent absorption and diffraction from solid-state samples in the extreme ultra-violet (XUV) regime is investigated. At these wavelengths, fluence dependent effects occur predominantly in experiments at free-electron laser (FEL) sources and attract considerable interest as they have important implications for the conclusiveness of studies performed at these light sources. The central question in this context is whether an experiment probes the electronic states intended, or if the sample suffers electronic damage during the femtosecond FEL pulse. At XUV wavelengths, this problem is currently unique to FEL-based experiments since here the number of photons per unit time and area impinging on the sample is about nine orders of magnitude higher than at synchrotron sources. This results in experimental situations in which a significant number of sample atoms interacts with more than one photon per pulse, giving rise to non-linear light–matter interactions.

The first part of this thesis demonstrates that an accurate characterization of fluence-dependent effects in FEL-based experiments requires measuring the spatial fluence distribution accepted by the sample on a single-shot basis, i.e. simultaneously with the actual diffraction experiment. None of the currently existing methods for obtaining the spatial fluence distribution allows such a simultaneous measurement on the sample under study. The reason for this is the fact that there can be substantial shot to shot variations and that in many experiments the sample is destroyed with a single FEL shot. Thus, a new fluence monitoring concept is developed. It is based on purposely distorted diffraction gratings that are monolithically integrated into carrier membranes. Such membranes are routinely used as sample support in soft x-ray and XUV experiments on solid samples. After the derivation of the distorted grating formula, theoretical calculations and numerical simulations are presented that explore the resolution and possible aberrations of the fluence maps obtained. This results in clear design principles for the grating specifications, based on directly accessible experimental parameters. Experiments using synchrotron and FEL radiation verify the theoretic findings and demonstrate the outstanding usefulness of the approach, especially for FEL-based experiments. A possible extension of the concept to hard x-rays is discussed.

The second part of this thesis employs the developed *in-situ* fluence monitoring concept to measure integral FEL pulse energies in an investigation of the fluence-dependence of resonant, XMCD-based diffraction signals at the $\mathrm{Co\,M}_{2,3}$ absorption resonance. The experiment reveals a breakdown of the resonant magnetic diffraction cross-section over the entire fluence range investigated. These experiments would have benefited greatly from the ability of spatially resolving the fluence distribution. However, gratings with the required specifications were not available for these experiments. Consequentially, the fluence map had to be inferred in a much more complicated process via additional measurements in combination with the fluence information from the sample-integrated grating monitors. A spatially and temporally discrete, numerical model was developed to understand the origin of the fluence dependence. It is based on the assumption that XUV-induced ultrafast demagnetization occurs during the propagation of the FEL pulse through the sample. The model reproduces the data measured very well, suggesting that ultrafast demagnetization is the dominant cause of the fluence dependence observed.

A follow-up experiment investigates to what extent stimulated emission may be responsible for a decrease of the magnetic scattering cross-section with increasing fluence, similar to the effects observed here. Reports in literature suggest that, at the $\mathrm{Co\,L_{2,3}}$ absorption resonance, this effect is responsible for similar findings to the ones in the first experiment of this thesis. The follow-up experiment uses spatially resolving grating monitors to check for a fluence dependence of non-resonant diffraction signals that are followed by resonant scattering events. The fluence range investigated is similar to the one in the first fluence-dependent experiment of this thesis. No evidence of stimulated emission is found, which suggests that stimulated emission does not play a major role for the fluence dependence observed at the $\mathrm{Co\,M_{2,3}}$ resonance and corroborates the purely demagnetization-based model introduced previously.

Zusammenfassung

Diese Arbeit befasst sich mit der Fluenzabhängigkeit von Absorption und Streuung an Festkörperproben im extremen ultraviolett (XUV) Spektralbereich. Bei diesen Wellenlängen können fluenzabhängige Effekte praktisch ausschließlich in Experimenten an Freie-Elektronen-Lasern (FEL) beobachtet werden. Solchen Experimenten kommt eine große Aufmerksamkeit zu, da ihre Ergebnisse die Aussagekraft vieler weiterer FEL-basierter Experimente betreffen. Der Grund dafür ist, dass für viele FEL-Experiment die Frage im Raum steht, ob die im Experiment untersuchte elektronische Struktur noch dem erwarteten Zustand entspricht, oder ob der intensive, nur Femtosekunden kurze FEL Puls diese Struktur bereits während der Messung zerstört. Dieses Problem stellt sich im XUV Bereich zur Zeit nur für FEL-basierte Experimente. Der Grund dafür ist die, gegenüber Synchrotronstrahlung, um neun Größenordnungen höhere Photonendichte (also die Anzahl der Photonen pro Zeit und Fläche). Durch solche hohen Photonendichten kommt es im Experiment dazu, dass ein signifikanter Anteil der Atome in der Probe innerhalb eines einzigen Lichtpulses mit mehr als einem Photon wechselwirkt, was zu nichtlinearen Licht–Materie Wechselwirkungen führt.

Im ersten Teil dieser Arbeit wird demonstriert, dass die Interpretation fluenzabhängiger Experimente an FELs zwingend eine präzise Messung der mit der Probe wechselwirkenden, räumlichen Fluenzverteilung erfordert. Diese Messung muss für jeden einzelnen FEL Schuss, d.h. zeitgleich mit der eigentlichen Messung des Streusignals, erfolgen. Keines der aktuell verwendeten Messverfahren ist in der Lage, für Festkörperproben solch eine simultane Messung durchzuführen. Daher wurde ein neues Messkonzept entwickelt, das diese Aufgabe erfüllt. Die Grundlage dieses Verfahrens bilden speziell designte Gitterstrukturen, die direkt in die Trägermembranen der Dünnschichtproben geschrieben werden. Streuexperimente im XUV und weichen Röntgenbereich nutzen diese Membranen standardmäßig als Substrate für die zu untersuchenden Proben.

Nach der Herleitung der Gittergleichung werden die Abbildungseigenschaften der Gittermonitore anhand von theoretischen Betrachtungen und numerischen Simulationen diskutiert. Daraus werden klare Prinzipien mit direkter Verbindung zu relevanten experimentellen Parametern für das Gitterdesign abgeleitet. Die theoretischen Vorhersagen werden durch Synchrotron- und FEL Experimente verifiziert. Im Weiteren wird die Anwendbarkeit des Konzepts im harten Röntgenbereich diskutiert.

Der zweite Teil dieser Arbeit verwendet das zuvor entwickelte Konzept zur *in-situ* Fluenzmessung um die Fluenzabhängigkeit von Streuung auf Basis des Röntgenzirkulardichroismus (XMCD-Effekt) an der Co $\mathrm{M}_{2,3}$ Absorptionsresonanz zu untersuchen. Dieses Experiment würde im besonderen Maße von einer gleichzeitigen Messung der räumlichen Fluenzverteilung auf der Probe profitieren. Leider waren für diese Messung noch keine räumlich auflösenden, sondern nur integrierende Gittermonitore verfügbar. Daher muss-

te die Fluenzverteilung mit deutlich aufwendigeren Mitteln aus zusätzlichen Messungen bestimmt werden. Im Experiment zeigt sich eine deutliche, fluenzabhängige Abnahme des Streuquerschnitts. Ein numerisches Modell wurde entwickelt, um die Ursache dieser Abhängigkeit zu identifizieren. Es basiert nur auf der Annahme, dass der XUV FEL Puls beim Durchgang durch die Probe einen ultraschnellen Entmagnetisierungsprozess in Gang setzt. Die Modellvorhersagen stimmen sehr gut mit den experimentellen Beobachtungen überein, was die Schlussfolgerung nahelegt, dass ultraschnelle Entmagnetisierung im vorgestellten Experiment hauptverantwortlich für die Fluenzabhängigkeit des XMCD Streuquerschnittes ist.

In einem zweiten Experiment wird der Frage nachgegangen, ob, und zu welchem Grad, stimulierte Emission eine Rolle für die Ergebnisse des ersten Experiments spielen kann. In Veröffentlichungen zur Fluenzabhängigkeit von XMCD-basierten Streusignalen an der Co $L_{2,3}$ Absorptionskante wird stimulierte Emission als zugrundeliegender Effekt identifiziert. Das in dieser Arbeit entwickelte Experiment verwendet die zuvor entwickelten, räumlich auflösenden Gittermonitore. Sie werden eingesetzt, um die zu erwartende Fluenzabhängigkeit nicht-resonanter Streusignale im Beisein von resonanter Absorption zu detektieren. Das Experiment erstreckt sich über einen vergleichbaren Fluenzbereich, wie das zuvor durchgeführte. Dabei werden keine Anzeichen von stimulierter Emission festgestellt. Entsprechend kann geschlussfolgert werden, dass stimulierte Emission im untersuchten Fluenzbereich an der Co $M_{2,3}$ Absorptionskante keine entscheidende Rolle spielt.

Preface

Parts of this thesis have been published in peer-reviewed journals. The text and figures might have been slightly modified to fit the context in which they appear in this work. Such paragraphs and figures are marked as follows:

- # Schneider, M., Günther, C. M., von Korff Schmising, C., Pfau, B. & Eisebitt, S. Curved gratings as an integrated photon fluence monitor in x-ray transmission scattering experiments. *Opt. Express* **24,** 13091 (2016), DOI: 10.1364/OE.24.013091
- † Schneider, M., Günther, C. M., Pfau, B., Capotondi, F., Manfredda, M., Zangrando, M., Mahne, N., Raimondi, L., Pedersoli, E., Naumenko, D. & Eisebitt, S. In situ single-shot diffractive fluence mapping for X-ray free-electron laser pulses. *Nat. Commun.* **9,** 214 (2018), DOI: 10.1038/s41467-017-02567-0
- ‡ Schneider, M., Günther, C. M., Pfau, B., Capotondi, F., Manfredda, M., Zangrando, M., Mahne, N., Raimondi, L., Pedersoli, E. & Eisebitt, S. In-situ single-shot diffractive fluence mapping for X-ray free-electron laser pulses. *Arxiv.* arXiv: `1705.03814` (2017)

The symbol ‡specifically denotes the pre-print version. It contains several short sections that are no longer included in the final print version, but will stay accessible under the given arXiv document number.

The author of this thesis (MS) is also the principal author of these publications. In particular, MS, BP, CMG and SE conceived the experiments. MS derived the grating formula and performed the simulations. MS and CMG prepared the samples. MS and all authors conducted the experiments. MS analyzed the data and developed the theoretical models. MS drafted the manuscripts with input from all authors.

Part I.

Fundamentals

1. Introduction

The concept of a linear interaction, i.e. of a reaction that is directly proportional to its cause, is fundamental for our scientific understanding of the world around us. Linear approximations are often necessary – not only in high-school physics – to derive analytical solutions and thereby gain an instructive understanding of the underlying physics. Such solutions are accurate as long as the system stays in the regime for which the approximation has been made. In the case of interactions between light and matter, this regime is characterized by the linear susceptibility – the direct proportionality between an external electric field and the induced polarization in the material. The invention of the laser in 1960 enabled new experiments that are governed by higher-order susceptibilities. Already in 1961, Franken *et al.* [4] demonstrated second harmonic generation on the basis of the newly available light source. This marks the starting point for the study of non-linear light–matter interaction. It quickly developed into an extensively studied field at optical and near-optical wavelengths with a plethora of advances in fundamental research as well as application development.

Comparable light sources to the optical laser for the extreme ultra-violet (XUV) (20 eV to 200 eV) and soft (200 eV to 2000 eV) as well as the tender- and hard x-ray regime (2000 eV to 5000 eV and higher) have become available comparably recently, with the development of the x-ray free-electron laser (FEL) in the last 20 years [5]. These new light sources have never been considered “a solution looking for a problem”, as their optical counterparts have been termed for a brief period of time after their development. Instead, the FEL’s unprecedented combination of femtosecond pulses of spatially coherent x-ray photons with several µJ pulse energy has immediately been hugely attractive for researchers working on, e.g. protein crystallography, chemical bond formation and dissociation, or fundamental light–matter interactions (see [5, 6] and references therein).

One of the main reasons for this interest is the fact that x-ray based techniques using synchrotron radiation have been hugely successful in the investigation of sample structures on an atomic and nanometer scale. However, these investigations have largely been limited to static structures or to temporal resolutions of several picoseconds. In contrast, optical lasers routinely achieve pulse durations in the femtosecond regime, but lack the spatial resolution of x-ray techniques due to their longer photon wavelength of several 100 nm. X-ray and XUV FELs are able to combine the high spatial resolution of small wavelengths with femtosecond temporal resolution, which often is a prerequisite for dynamic investigations of the relationship between structural properties and functionality on atomic, molecular and nanoscopic length scales [5].

In addition to FELs, the last decade has seen the development of laboratory-scale sources of XUV radiation based on intense femtosecond optical laser pulses. These optical pulses are focused into noble gas targets. The ensuing high-harmonic generation

(HHG) process creates a photon pulse with several photon energies that are integer multiples of that of the driving laser's [7]. The photon flux and maximum energy reachable is steadily increasing due to improved driving lasers and optimized HHG setups. Currently, these table-top sources reach µJ pulse energies, which is within 1 % of the pulse energy of an XUV FEL source for the same wavelength [8]. Thus, HHG sources are an increasingly important alternative to FELs at XUV and, progressively, soft x-ray wavelengths. However, especially at photon energies above 50 eV, typical values for XUV FEL sources are still much higher at 10 µJ to some 100 µJ pulse energies. In the context of this thesis, high single-shot pulse energies are paramount. The experiments described here investigate the fluence-dependence of diffraction signals at XUV wavelengths. They require pulse energies of several 10 µJ and can thus only be performed at an FEL source.

The experiments presented in this thesis are fluence-dependent. In other words, the signal detected depends non-linearly on the number of photons per unit time and area interacting with the sample. In FEL-based experiments, such a situation easily arises, as the following simplified estimate shows. Assume an FEL beam with a typical number of 10^{12} photons/pulse, focused on a 10 µm × 10 µm area of a Si sample. At a photon energy of 100 eV (i.e. in resonance with the Si $L_{2,3}$ absorption resonance), the sample absorbs 97 % of the photons within a depth of 200 nm [9]. Given the molar volume of Si, every atom absorbs (on average) two photons per pulse. The life-time of the resulting core-hole vacancy is on the 10 fs time-scale [10]. With typical pulse durations for XUV FELs of 30 fs to 100 fs, it is to be expected that a significant number of photons encounters an excited Si atom and thus yields a modified scattering signal compared to the Si ground state.

Even at lower fluences than such a simplistic estimate suggests, the electronic system of a sample is subject to *electronic damage* on a fs time scale [11]. This is typically not an issue when probing structural properties, i.e. atomic sites or the topography of a solid sample. Here, the atomic bodies' inertia ensures that their positions are measured correctly, even though the atoms may subsequently be stripped of their electrons within the sub-100 fs FEL pulse. The large amount of deposited energy destroys the sample in a Coulomb explosion [11], which coined the name "diffract-before-destroy" for this concept [12].

Conversely, experiments that aim to investigate the electronic structure of a sample intact, are especially susceptible to photon-induced damage. Here, the photon beam may disturb the sample under study to such an extent, that the whole experiment is compromised since it cannot probe the electronic system in the ground- or a deliberately prepared excited state. It is thus of pivotal importance to identify at which photon density such a significant deviation from the intended state occurs for the particular system under study, and what the principal mechanisms are, that govern this deviation. This is only possible with an intricate knowledge, and precise control of the spatial fluence distribution on the sample. Many measurements that require fs temporal resolution and the contrast mechanisms or spatial resolution offered by x-ray and XUV radiation are necessarily performed at FEL sources. This makes a significant difference to the optical regime. Optical lasers with an intensity profile that is stable from shot to shot are commonly available. They can provide fs pulses at shot energies of several mJ. In addition, efficient refractive optics, beam splitters and mirrors of extremely high quality are also routinely available. Thus, the spatial fluence distribution in the sample plane is typically smooth and stable over time. This makes it easy to accurately measure this distribution separately from the actual experiment and to accommodate it in model calculations.

In contrast to that, FELs are, inherently, highly fluctuating light sources. In the self-amplified spontaneous emission (SASE) scheme, the amplification process randomly starts from noise [5]. Thus, every photon pulse has a slightly different spectrum and spatial position. Even in seeded FELs – where an external ultra-violet (UV) laser determines the central wavelength – the spatial beam position varies. The large scale of FEL facilities of several hundred meters to kilometers amplifies slight angular pointing instabilities that occur e.g. due to thermal gradients and vibrations. For the experiments presented in this thesis, this results in shot-to-shot changes of the beam position on the sample of several µm, which is comparable to the footprint of the focused beam on the sample. At the soft x-ray and XUV wavelengths used in the experiments performed, several factors combine that further exacerbate this inherent instability: (i) There are typically no refractive optics available, since the refractive index at these wavelengths is very close to unity for virtually all materials. (ii) The absorption length for XUV and soft x-ray photons in ambient air is in the sub-mm range, and only sub-µm for solid samples (and several orders of magnitude less at absorption resonances). This necessitates a high vacuum (HV) environment and limits the thickness of transmissive optical elements, such as filters, to typically less than 1 µm. (iii) Diffractive optics require high-resolution lithography with structure sizes of less than 50 nm for good performance. This entails elaborate manufacturing processes and effectively limits the total size of such optical elements to the sub-mm regime. (iv) Reflective optics only work as multi-layer, Bragg-type mirror for a certain wavelength, or at grazing incidence. The latter makes them large and requires precise control of the shape and surface finish to wavelength-scale accuracy over length scales of several 10 cm. (v) The surface roughness of optical elements is comparable to the photon wavelength. This introduces aberrations and further reduces the efficiency.

In the context of the XUV experiments in this thesis, the absence of refractive optics – and the resulting prevalence of their diffractive and reflective counterparts – is likely the most significant. Such elements are indispensable for the beam delivery and focusing, e.g. in Kirkpatrick-Baez (KB) mirror units [13]. Due to their limited size and lithographic imperfections, they introduce diffraction artifacts into the beam. Such artifacts manifest in complex periodic patterns and steep intensity gradients over less than 1 µm at the sample position. Thus, focused FEL spots often have a complicated internal structure and suffer from spatial jitter, i.e. shot-to-shot changes of the beam position.

Consequentially, fluence-dependent experiments at FELs require sophisticated control of the sample illumination. This includes the *in-situ* monitoring of the focus position and, possibly, the precise alignment of several FEL beams. An exact knowledge of the number of photons per unit time and area on the sample is crucial to interpret the measurements. A number of well-established techniques exist to estimate these pivotal parameters. Gas monitor detectors (GMD) are able to measure the total photon number in a single, few-femtosecond pulse [14], but cannot account for the intensity distribution within the focal spot on the sample. This distribution is typically measured – separately from the actual experiment – using wave-front sensing [15–17], ablative imprints [18, 19], or by detecting the transmitted intensity through a small aperture or behind a sharp knife-edge scanned across the beam in the sample plane [20, 21]. These approaches are highly invasive and cannot be performed in tandem with the majority of FEL experiments. They are in particular incompatible with all scattering experiments in the forward direction and cannot account for the finite acceptance of a sample smaller than the beam size or for the beam position on a larger and potentially inhomogeneous sample. This leads to significant uncertainties, especially in diffract-and-destroy experiments, where a new sample is aligned after every single shot [12, 22, 23]. †

The first part of this thesis describes the development of a novel *in-situ* fluence monitoring scheme that is especially suitable for the XUV and soft x-ray regime, and extensible to hard x-rays. This approach is subsequently used to investigate the fluence dependence of the X-ray magnetic circular dichroism (XMCD)-based scattering signal from ferromagnetic samples. The XMCD effect is routinely exploited as a contrast mechanism in XUV, as well as soft and hard x-ray experiments to study magnetization-related effects, such as ultrafast demagnetization [24, 25], magnetization reversal [26] and dynamics of magnetic domains and spin structures [27].

In 2012, Wang *et al.* observed first indications of a fluence-dependent XMCD diffraction cross-section for Co-based magnetic multi-layer samples. Their experiments at the Linear Coherent Light Source (LCLS) FEL facility exploit the XMCD contrast at the Co $\mathrm{L}_{2,3}$ absorption resonance (780 eV). With non-destructive fluences of up to $30\,\mathrm{mJ/cm^2}$, they find a reduced diffraction cross-section for 360 fs pulses, but not for shorter, 80 fs, pulse lengths. The reduction at $30\,\mathrm{mJ/cm^2}$ is about 10 % for the longer pulses. Wang *et al.* suggest x-ray induced demagnetization of the sample as a reason for the observed fluence dependence. [28]

Following this, Müller *et al.* performed a diffraction experiment that exploits the XMCD effect at the Co $\mathrm{M}_{2,3}$ absorption resonance using the Free-Electron Laser in Hamburg (FLASH) FEL source. In this experiment, the Co-based multi-layer sample is subject to a single, 100 fs, destructive shot of $5000\,\mathrm{mJ/cm^2}$. For this high-fluence shot, the XMCD diffraction cross-section drops to about 5 %, i.e. a 95 % reduction with respect to the low-fluence case. Here, the authors suggest that high ionization levels of the Co atoms shift the Co $\mathrm{M}_{2,3}$ absorption resonance within the first few femtoseconds of the FEL pulse. Then, the subsequent parts of the FEL beam cannot contribute to the resonant diffraction signal. [29]

In 2016, Wu *et al.* suggested stimulated emission to be responsible for the fluence dependence of XMCD-based diffraction signals at the Co $\mathrm{L}_{2,3}$ resonance. This experiment covers fluences from $1\,\mathrm{mJ/cm^2}$ to $300\,\mathrm{mJ/cm^2}$ at 50 fs FEL pulse length. The samples used are designed for lensless imaging experiments. The diffraction pattern of these samples consists not only of the resonant magnetic contribution, but also of non-resonant diffraction from a gold mask that is necessary for the lensless imaging scheme. Surprisingly, the non-resonant, non-magnetic diffraction cross-section also diminishes at higher fluences. Wu *et al.* demonstrate that enhanced forward scattering due to stimulated emission is able to quantitatively explain the simultaneous reduction of both scattering signals. [30]

The goal of this thesis is to provide systematic and reliable data on the fluence dependence of the XMCD diffraction cross-section. Such data is essential to unravel the diverse observations and suggested explanations already in existence. The experiments in this work concentrate on XUV photon wavelengths, i.e. on the Co $\mathrm{M}_{2,3}$ absorption resonance. Up to the time of writing, the only published data in this energy range is the experiment of Müller *et al.* – that is, two data points at $7.5\,\mathrm{mJ/cm^2}$ and $5000\,\mathrm{mJ/cm^2}$, respectively. Recording the entire fluence dependence over three orders of magnitude, as done in this thesis, provides a reliable basis for theoretical modeling. This will ultimately reveal, which of the proposed effects predominantly governs the fluence dependence. The experimental concepts developed in this thesis directly transfer to the study of the fluence dependence of other signals, such as resonant absorption at XUV and soft x-ray wavelengths.

2. Methods

2.1. Overview

This section describes the necessary tools to plan, prepare, conduct and analyze the experiments in this thesis. The development of the methods presented is not part of this work, and their description is accordingly brief. Their basic concepts are typically only mentioned to provide an overview and serve as a starting point for further reading in the references provided.

In this thesis, diffraction experiments in transmission geometry at soft x-ray and XUV photon energies are performed at the BESSYII synchrotron source and the Free Electron laser Radiation for Multidisciplinary Investigations (FERMI) FEL. The basis of the samples are commercially available Si_3N_4 membranes, etched into Si frames [31], with sizes ranging from $20\,\mu\text{m} \times 20\,\mu\text{m}$ to $200\,\mu\text{m} \times 200\,\mu\text{m}$ and thicknesses from 30 nm to 200 nm. The membranes provide a transparent support structure for the sample under study. Their transmission at 60 eV and 30 nm thickness is 55 %, and 86 % for 780 eV photons and 100 nm thickness [9]. Additional sample layers are deposited by thermal evaporation, as well as direct current (DC) and radio frequency (RF) magnetron sputtering [32]. An FEI Helios Nanolab 600 focused ion beam (FIB) provides a flexible way to nano-structure the samples. Apart from the diffraction experiments, samples are characterized via standard scanning electron microscopy (SEM), atomic force microscopy (AFM) and magnetic force microscopy (MFM) measurements. Numerical simulations of the electric field propagation in the near- and far-field approximation are used to predict and understand the sample's diffraction behavior.

2.2. Diffraction geometry

Fig. 2.1a schematically shows a diffraction experiment in transmission geometry on a prototypical periodic structure. Throughout this thesis, coordinates in the sample plane are denoted (ξ, η), while coordinates in the detector plane are (x, y). The distance between both planes is z_{det}.

The incident FEL beam with wavelength λ impinges on the sample at normal incidence. In solids, non-resonant absorption lengths ($1/e$ attenuation) are typically less than 100 nm for XUV photons, and under $1\,\mu\text{m}$ for soft x-ray wavelengths. Accordingly, the samples in this thesis are only some ten nanometer thin. Within the sample, local inhomogeneities manifest as a phase- or absorption contrast for the incoming beam. Consequentially, parts of the beam are diffracted away from the original propagation direction. The diffraction angle θ, i.e. the azimuthal angle relative to the undeflected beam, is related to the spatial period p of the diffracting structure. In the Fraunhofer approximation, it is given by [33]

$$\sin\theta = \frac{\lambda}{p} \tag{2.1}$$

This fundamental relation between structural periodicity and diffraction angle is of pivotal importance to virtually all diffraction experiments, irrespective of the utilized radiation. In the experiment, θ translates to a (x, y) position of the diffraction in the detector plane,

$$\theta = \arctan\left(\frac{\sqrt{x^2 + y^2}}{z_{\mathrm{det}}}\right) \tag{2.2}$$

The Fourier transform ($\mathcal{F}$) links a given structure and its corresponding diffraction pattern [33]. Fig. 2.1b illustrates this relationship. In the example shown, a regular grating in the sample plane (with periodicity p) produces two distinct spots – the positive and negative diffraction order – at $\pm\Delta q$ in addition to the undeflected part of the beam at $q = 0$. Δq is the in-plane component of the momentum transfer, given by

$$\Delta q = \frac{2\pi}{\lambda}\sin\theta = \frac{2\pi}{p} \tag{2.3}$$

The Fourier transform yields the Fraunhofer diffraction pattern, not just for periodic gratings, but for arbitrary structures. This makes it an indispensable tool to devise and plan the diffraction experiments in this work.

2.3. XMCD contrast

Apart from regular non-resonant or resonant x-ray absorption, the XMCD effect is the most important contrast mechanism for the diffraction experiments in this work. This effect modifies the absorption cross-section of a magnetic material, depending on the magnetization direction and polarization of the incident x-ray or XUV photons [34]. For the ferromagnetic 3d transition metals – iron, nickel and cobalt – this contrast is largest at the $\mathrm{L}_{2,3}$ absorption resonances (700 eV to 900 eV), but is also routinely exploited at the $\mathrm{M}_{2,3}$ edges [35]. In both cases, the resulting magnetic contrast enables soft x-ray and XUV imaging [36–38] as well as spectroscopy experiments [39–42]. For the photons, different magnetization directions (and magnitudes) act, in good approximation, as an absorption grating. This gives rise to a diffraction signal in very much the same way as a topographic structure would [39]. Analogous to the grating discussed in the previous section, the diffraction angle is directly related to the in-plane periodicity of the magnetic structure. The XMCD absorption asymmetry is only observable in the transmitted beam using circular polarized photons. However, linear polarized light still gives rise to

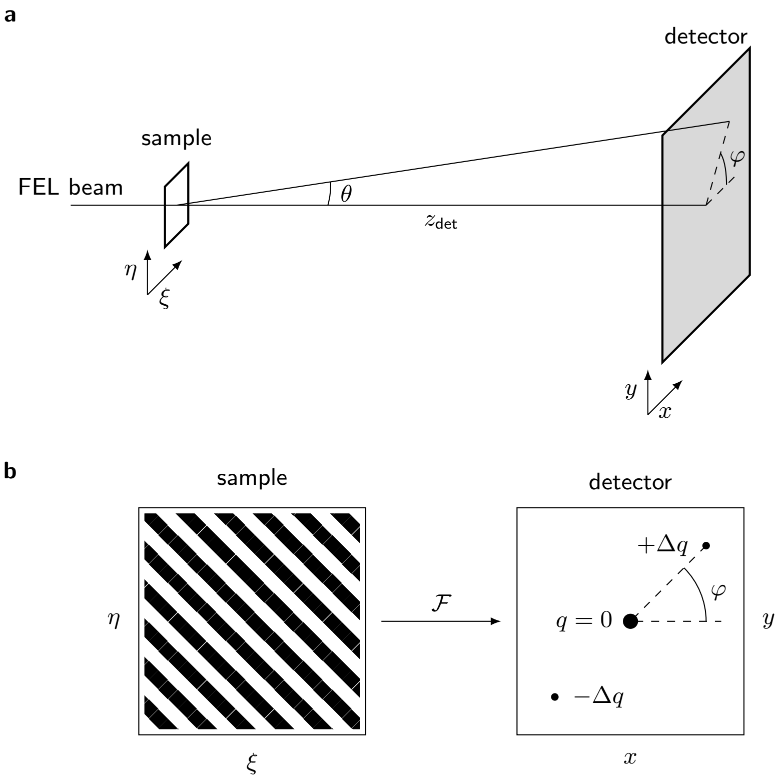
a
detector
sample
FEL beam
θ
z_{det}
φ
η
ξ
y
x
b
sample
detector
η
ξ
$\mathcal{F}$
$+\Delta q$
φ
$q = 0$
$-\Delta q$
y
x

Figure 2.1.: Diffraction geometry and coordinate systems in the sample and detector plane. a) Schematic sketch of the experiment geometry with sample plane (ξ, η) at $z = 0$ and detector plane (x, y) at $z = z_{\mathsf{det}}$. The diffraction angle θ is directly related to the photon wavelength and the periodicity of the diffracting structure, as discussed in the main text. The polar angle φ corresponds to the orientation of the diffracting structure. **b)** Relationship between structure and diffraction pattern. Here, the sample is a regular grating with 45° orientation. The corresponding diffraction pattern in the detector plane is the Fourier transform $(\mathcal{F})$ of the grating transmission. It consists of the directly transmitted beam $(q = 0)$ and the grating's positive and negative diffraction orders with an in-plane momentum transfer $\pm\Delta q$.

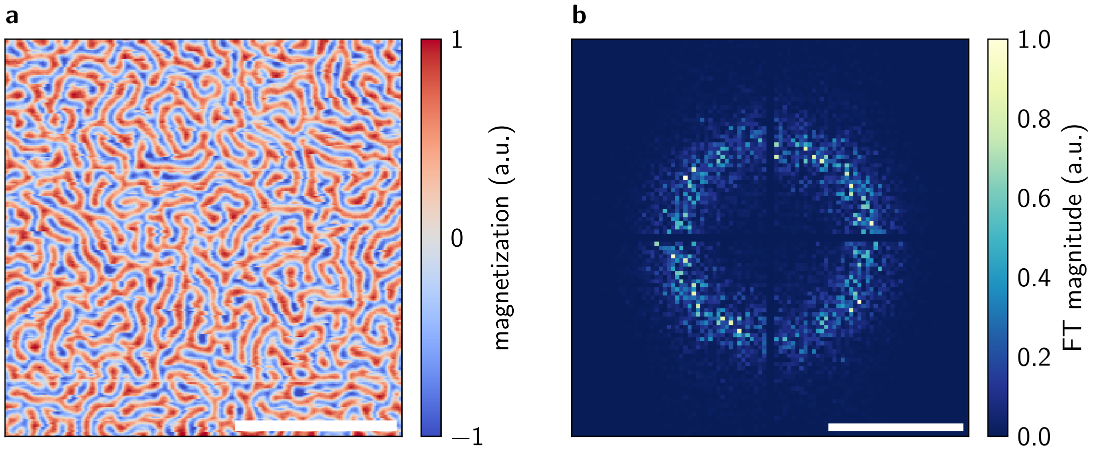

Figure 2.2.: Magnetic domains in a multi-layer sample. a) MFM raster scan of a typical PMA sample as used in this work. The MFM is only sensitive to magnetization directions perpendicular to the image plane. Red and blue color denotes magnetization vectors pointing in and out of the image plane, respectively. Within the field of view, the domains are unaligned and have a homogeneous width of about 100 nm. Scale bar is 2 μm. **b)** Fourier-transform (FT) of the domain pattern. The ring-shaped structure indicates isotropic domains. Scale bar is 40 μm^{-1}

a diffraction signal from a magnetically inhomogeneous sample, as the opposing circular components that comprise the linear polarization scatter independently. The intensity of this diffraction signal is proportional to the sample magnetization squared [39]. In their book, Stöhr & Siegmann give a comprehensive overview on this topic [34].

The magnetic absorption asymmetry is proportional to the scalar product of the magnetization vector and the photon propagation direction. In other words, its magnitude is largest when the magnetization is parallel or anti-parallel to the helicity vector of the circularly polarized radiation and vanishes in between. For the thin-film samples in this thesis, the magnetization is along the sample normal. In the experiment, they are oriented such that the FEL beam is parallel to the sample normal, maximizing the XMCD-based absorption contrast. The class of such perpendicular magnetic anisotropy (PMA) materials is ubiquitous in modern magnetic storage media and a subject of intense fundamental and technological research. Commonly, they are multi-layers with a composition of alternating ferromagnetic and non-magnetic layers and additional seed- and cap-layers of various materials. Typical thicknesses of the individual layers are 4 Å to 15 Å. Their properties are thus dominated by surface and interface effects, which align the magnetization perpendicular to the film (see [43, 44] and references therein). Both Co/Pt and Co/Pd multi-layers are used for the experiments in this thesis. Without an external magnetic field, the magnetization of these layers forms an isotropic, labyrinthian pattern in the sample plane as a low-energy configuration (Fig. 2.2a). Additionally, Fig. 2.2b shows the corresponding ring-shaped diffraction pattern, obtained by a Fourier-transform of the domain image.

2.4. General experimental setup

All diffraction experiments in this work are in normal incidence transmission geometry and detect the scattered XUV or soft x-ray radiation as a function of momentum transfer. The incident photons interact resonantly as well as non-resonantly with the sample and a charge-coupled device (CCD) camera measures the diffracted intensity further downstream. Fig. 2.3 schematically shows this basic experimental layout. The absorption length for 60 eV photons in ambient air is only 65 µm [9], necessitating an HV environment.

A Princeton Instruments MTE 2048B back-illuminated CCD camera with 2048 × 2048 pixel of 13.5 µm × 13.5 µm pixel size records the diffracted intensity behind the sample. Any absorbed x-ray photon generates a number of electron–hole pairs in the separated quantum wells that comprise the CCD pixels. The exact number of generated electrons is a function of the photon energy. In our case, a single 780 eV (60 eV) photon generates approximately 130 (20) electrons. The full-well capacity of a single detector pixel is about 1×10^5 electrons [45]. Due to this, the detector has a limited dynamic range and limited linear regime in which the measured intensity is proportional to the incident photon number.

When read-out- and detector-noise is considered as well, the actual dynamic range, i.e. the maximum attainable ratio of lowest and highest detected intensity, quickly drops to approximately 1:100. Due to this, and to prevent permanent damage, the camera needs to be protected from the intense zero-order (i.e. directly transmitted) beam and potential scattering from the membrane edges by a cross-shaped beam-stop.

2.5. Diffraction setup at the FERMI FEL

The FEL experiments in this work follow the same basic principles as outlined in the previous section. However, several features of these experiments are specific to FEL facilities and have direct bearing on the matter of this thesis. All fluence-dependent XUV diffraction experiments are performed at the Diffraction and Projection Imaging (DiProI) end-station of the FERMI@Elettra FEL [46, 47]. The FEL generates highly intense photon pulses in the XUV regime (i.e. below 100 eV) with several tens of µJ shot energy, variable polarization and pulse lengths on the order of 50 fs [13, 48]. A KB bendable mirror optic focuses the photon beam down to a – typically non-Gaussian – spot with a size of 10 µm × 10 µm and below in the sample plane [49]. With such a tight focus and shot energies in the µJ range, fluences in excess of several J/cm^2 are possible and allow the study of non-linear light–matter interactions.

On-line diagnostic of the incident shot energy is provided by a gas monitor detector (GMD) [14]. This device measures the integral energy per photon pulse, which is an important parameter for fluence-dependent studies. However, it cannot account for the spatial fluence distribution *within* the focal spot in the sample plane. This distribution is typically measured – separately from the actual experiment – using wave-front sensing [15–17], ablative imprints [18, 19], or by detecting the transmitted intensity through a

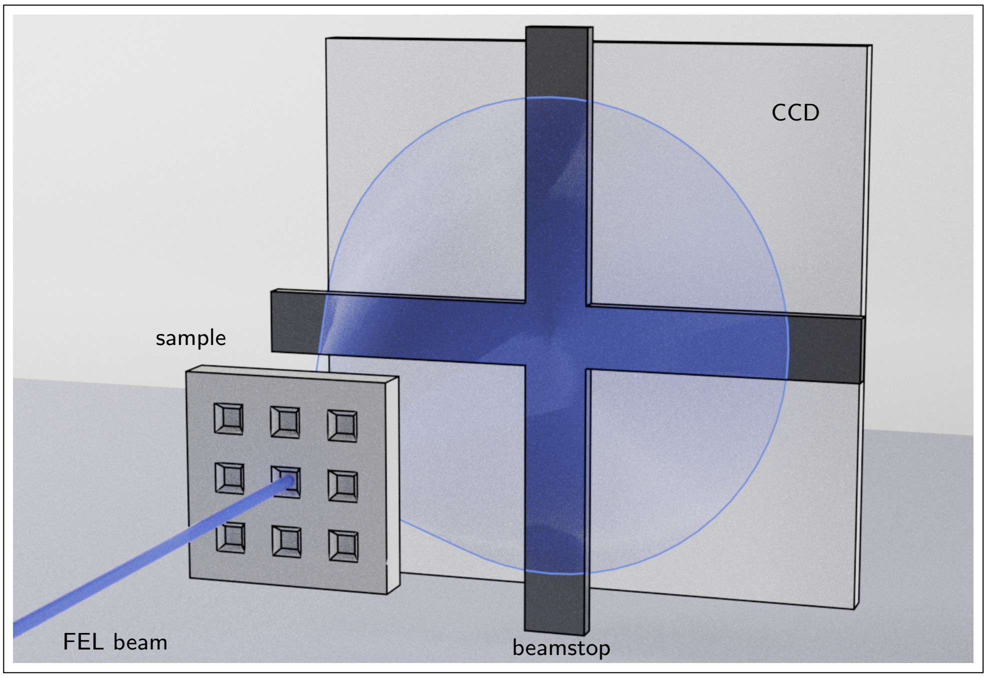

Figure 2.3.: Schematic layout of an XUV and soft x-ray diffraction experiment. The sample is a Si chip with several Si_3N_4 windows etched into it. Typically, we deposit the actual sample layer under study on the flat sample side (not shown). One of the sample membranes is aligned to the incident FEL beam (blue). A CCD camera (large rectangular area) detects the diffracted intensity. The dark cross-shaped structure in front of the camera is the beamstop. It protects the camera from the intense direct beam and light which scatters off the membrane edges.

small aperture scanned across the beam in the sample plane. A key aspect of this work is to develop a method that measures the fluence on the sample in a transparent manner, i.e. such that it does not interfere with the primary experiment. †

2.5.1. Time structure of the FEL pulse at FERMI

When investigating fluence-dependent effects, the temporal pulse profile, i.e. the number of photons per unit time, is a critical parameter. Finetti *et al.* performed cross-correlation measurements to directly measure the FERMI pulse length. In their experiments, they overlap an external visible or infra-red (IR) pulse with the XUV FEL pulse on gaseous and solid samples. Both the IR and visible laser pulses are generated by the seed laser to minimize arrival-time jitter. In a He gas jet, the XUV photons generate photoelectrons at the electron binding energy E_0. A temporally overlapping IR pulse with photon energy $h\nu$ causes side bands at $E_0 \pm h\nu$ to appear in the photoelectron spectrum. Since the duration of the IR pulse is known, scanning the time-delay between both pulses yields the FEL pulse length [50]. A second experiment exploits the XUV-induced transmission change of a Si_3N_4 membrane for visible light. Here, the wave-front of the XUV pulse is tilted with respect to the sample normal. Thus, spatial positions on the sample translate to different time delays. The XUV photons transiently increase the transmission for visible light. This directly encodes the FEL pulse's temporal structure into the spatial intensity profile of the transmitted light [50].

Both measurements show, that the FEL pulse length (τ_{fel}) follow the relation

$$\tau_{\mathrm{fel}} = \frac{7}{6}\tau_{\mathrm{uv}} \cdot n^{-\frac{1}{3}}\,, \tag{2.4}$$

with the seed pulse length τ_{uv} and the harmonic conversion factor $n = \lambda_{\mathrm{uv}}/\lambda_{\mathrm{fel}}$. For the experimental parameters in this work, the FEL pulse lengths are between 70(20) fs and 140(20) fs [50].

2.5.2. Wave-front sensing

As mentioned, a bendable KB mirror pair at the DiProI end-station provides an adjustable focus with spot-sizes of 10 µm and below [49]. Adjusting the correct mirror deformation to achieve a smooth spatial intensity distribution for a given spot size in the focal plane is a complex task that requires detailed and, ideally, instantaneous feedback. A wave-front sensor (WFS) is able to provide this crucial feedback by measuring the local intensity and curvature of the FEL beam.

The utilized Hartmann WFS consists of an opaque plate with an array of small, circular holes in it. Downstream of this Hartmann-plate, a CCD camera measures the intensity of the radiation that passes the hole array. Each illuminated hole in the Hartmann-plate produces a distinct spot on the CCD detector. The local curvature of the wave-field directly translates to a shift of the spot with respect to the position that a plane wave with normal incidence would produce. The WFS thus measures an array of local curvature and intensity, from which the beam parameters and the electromagnetic field,

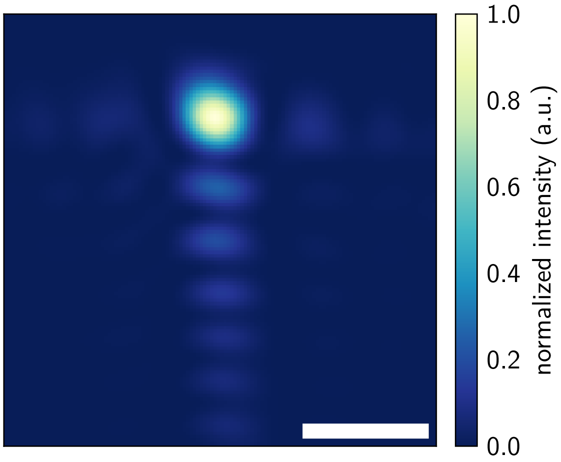

Figure 2.4.: Wave-front sensor measurement Spatial fluence distribution near the focal position at the DiProI end-station of the FERMI FEL. Extrapolated from a single-shot WFS measurement. Scale bar is 10 µm.

including the phase, can be calculated [51]. This measurement scheme is incompatible with focal sizes in the sub-millimeter range. Therefore, the WFS is typically placed on the order of 1 m downstream of the focus. Here, the beam footprint is large enough to facilitate a high-quality measurement. The intensity distribution in the focal plane is then numerically extrapolated [51]. Fig. 2.4 displays an example of such an extrapolated spatial fluence distribution.

It is obvious, that these spatial requirements make wave-front sensing incompatible with most diffraction experiments in the forward direction, as the detector for the diffracted intensity needs to be removed. A notable exception to this are detectors that feature a central aperture and thereby allow a "transparent" diffraction experiment with downstream beam diagnostic. However, such highly specialized detectors are not widely available and typically require much larger effort for operation than commercial detectors [52, 53].

2.5.3. Ablation imprints

The FEL beam induces permanent damage when focused tightly onto a solid sample surface. Thermal melting is the dominant process at moderate fluences of less than $0.1\,\mathrm{J/cm^2}$, with considerable differences between substrate materials. However, when the fluence exceeds approximately $1\,\mathrm{J/cm^2}$, non-thermal melting, or ablation, is the principal damage mechanism and differences between substrate materials are smaller [54, 55].

During the fluence-dependent experiments in the second part of this thesis, ablation imprints are continuously generated in the Si substrate alongside the primary experiment. These imprints allow for evaluation of the FEL focus after the experiment. They provide the spatial beam profile at the sample position and document slow changes of the beam focus as well as shot-to-shot variations. It is important to note, that these imprints never belong to the same FEL shot that causes the diffraction signal on the detector. The information they yield is only valid when the spatial fluence distribution does not change between FEL shots. Furthermore, the evaluation of these imprints requires time-consuming AFM scans of each damage crater and thus cannot provide *in-situ* feedback during the experiment.

The spatial fluence distribution $F(\xi, \eta)$ is related to the AFM-measured height profile $z_{\mathrm{AFM}}(\xi, \eta)$:

$$F(\xi, \eta) \propto \exp\left(\frac{z_{\mathrm{AFM}}(\xi, \eta)}{l_{\mathrm{at}}}\right) \tag{2.5}$$

Here, l_{at} is the absorption length of the XUV radiation in the substrate material. This assumes that the absorption in the substrate follows the Beer-Lambert law (i.e. exponential attenuation) and that the beam profile does not change substantially within the absorption length [18]. The AFM image shown in Fig. 2.5a shows such an ablation imprint. Most of the damage crater is due to ablation and delineates the three-dimensional iso-surface up to which the local fluence exceeds the ablation threshold. Droplets of substrate material form around the crater edges due to thermal melting in regions of lower fluence, such as the beam tails. These need to be removed manually before the beam profile can be retrieved (Fig. 2.5b).

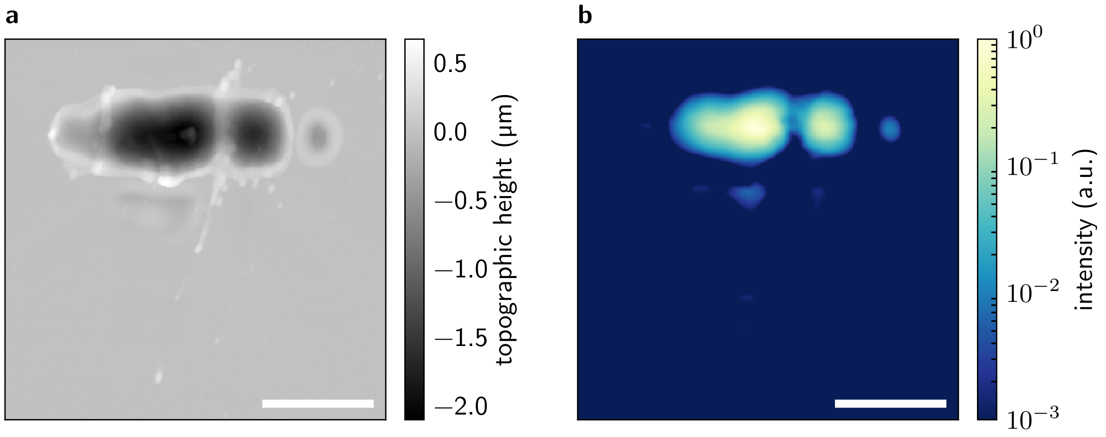

Figure 2.5.: Spatial fluence distribution from ablation imprints. **a)** AFM scan of a crater, produced by a focused 10 µJ FEL shot in Si. Apart from the non-thermal ablation, the topography also shows signs of redeposition and thermal melting. These need to be removed manually before the fluence distribution can be calculated according to Eq. (2.5). **b)** Spatial fluence distribution calculated from the AFM profile, assuming an absorption length of 350 nm for 60 eV photons in Si [9]. The final fluence map chiefly consists of the spots with highest fluence. Low-fluence sections are cropped due to the high ablation threshold of Si. This cannot easily be circumvented by higher indentation shot energies, since these also increase the amount of redeposition droplets and thermal melting. Thus, ablation imprints in the substrate material are most useful to detect qualitative changes in the spatial fluence distribution. Scale bars correspond to a length of 10 µm.

2.6. Sample Fabrication

The experimental geometry in this work is conceptually quite simple, as shown in the general experimental layout (Section 2.4). In principle, it requires only the photon beam, a detector, and the sample. The sophistication of the fluence-dependent experiments in this thesis lies within the sample design and fabrication. This is greatly beneficial considering that FEL beamtimes impose tight constraints on the experiment's schedule. Such constraints apply to a much lesser degree during sample preparation. This fact is, for example, also exploited in lensless imaging experiments at FEL and synchrotron sources in which the sample unifies the object under study, the imaging setup and additional experiment-related functionality [25, 56]

The following sections outline the manufacturing steps that are necessary to prepare the samples used in this work. All techniques are well-established and often industry-standard. Their description is accordingly brief.

2.6.1. Sputter deposition

The samples in the experiments of this work are thin multi-layers of specific composition and thickness. Depositing these layers requires control of each individual layer's properties. DC and RF magnetron sputtering is a suitable and well-established deposition technique for conducting and insulating target materials, respectively. It yields layers with a thickness precision of single atomic layers and has a plethora of applications from fundamental research to large-scale industrial fabrication. It is furthermore compatible with virtually all solid target materials, since it relies on the direct momentum-transfer between the Ar^+-ions that serve as sputtering agent and the target atoms[32]. The angular distribution of the material deposition is cosine-shaped. As a result, the growth-rate of the sputtered material on the substrate depends strongly on the distance between target and substrate. A small separation leads to higher growth-rates and efficient use of the target material at the expense of film homogeneity [32].

The sputtering system employed in this work allows several sputter targets to be used simultaneously or in succession. This enables the preparation of complex alloy and multi-layer structures. Apart from such direct material variations, there are a number of process variables that influence the final layer's properties. These include, e.g. the residual gas pressure and composition in the sputtering chamber, or the substrate temperature. In the case of magnetic thin-films, the different materials, thickness variations and process variables form a large parameter space, the exploration of which constitutes its own branch of material science. The material development is beyond the scope of this thesis and all utilized multi-layers follow established recipes. In particular, the experiments discussed utilize Co/Pd and Co/Pt multi-layers.

2.6.2. Focused ion beam milling

We use direct FIB-writing with a nominal lateral resolution of 10 nm to mill nanostructures into our samples. The FEI Helios 600 FIB employed provides a beam of

Ga^+-ions at acceleration voltages of up to 30 kV and beam currents in the pA to nA range. A series of electrostatic and electromagnetic lenses focuses the ion beam to a spot size of less than 10 nm. An additional pair of electrostatic deflection plates scans the focused beam over the sample. Here, the comparably heavy Ga^+ ions transfer energy and momentum to the sample atoms. This results, among other effects, in sputtered sample atoms, secondary electrons and characteristic x-ray radiation. The sputtering allows to directly write patterns into the sample, while the latter two serve as signal sources in raster images.

As a primarily momentum-based sputter process, FIB-milling has a low element specificity. Different materials do have noticeably different mill rates according to their respective hardness, however. For a given focal size, the ion current (i.e. the number of ions per area and unit time) governs the mill speed. A higher current increases the mill speed, but reduces the attainable resolution, since the ions repel each other due to the Coulomb force. Thus, FIB-milling a pattern is always a trade-off between resolution and manufacturing time [57].

The material to be structured needs to be conductive, in order to prevent charge build-up from the Ga^+ ions. This is not an issue for metallic samples. In contrast to that, insulating samples will often require a conductive coating for milling or imaging. Typically, a few nanometer of thermally evaporated or sputtered chromium suffices and adheres well on all solid materials used in this thesis.

Ga^+-ion may penetrate the Si_3N_4 membrane and affect subsequent sample layers. The principal damage mechanisms are sputtering and intermixing of layers due to the comparably large energy and momentum transfer [57]. This is an important consideration, especially for the thin magnetic multi-layers in this work. The Stopping and Range of Ions in Matter (SRIM) software package [58] reliably simulates the ion range and atomic displacement in solid targets. The depth distribution of Ga^+ ions at 30 keV has its maximum around 20 nm, but extends up to 60 nm which significantly exceeds the membrane thickness of 30 nm used for XUV experiments. Consequentially, a modification of the actual sample layer on the backside of the membrane is to be expected for sensitive samples due to ion-implantation. Milled structures thus have to be fabricated prior to the deposition of the sample layer on the membrane. This is the case in most XUV experiments in transmission geometry, where thicker substrates are impractical due to their high absorption. #

2.7. Numerical simulations of the diffracted field

Using numerical algorithms, we are able to quickly calculate the diffraction of arbitrary, two-dimensional structures. When done carefully and with their respective restrictions in mind, these simulations are a reliable tool to assess different sample designs and test their performance without elaborate sample preparation and diffraction experiments.

We perform numerical simulations using a regular, complex-valued grid that represents the electric field. The available memory limits the total size and resolution of the simulation area. Given a typical grid-size of 4096 × 4096 (8192 × 8192) points and a simulated sample size of 35 µm × 35 µm, the resolution is about 8.5 nm (4.3 nm). This exceeds the FIB resolution of 10 nm and is thus sufficient to simulate most of the structures that we are capable to prepare experimentally.

2.7.1. Exit-wave and illumination function

The starting point for all our simulations is the exit-wave, i.e. the electric field's amplitude and phase immediately after the diffracting object. For thin films, the exit-wave is the incident illumination, multiplied by the object's complex transmission function $T(\xi, \eta)$ [59]:

$$E(\xi, \eta) = E_0(\xi, \eta) \cdot T(\xi, \eta) \tag{2.6}$$

with

$$T(\xi, \eta) = \exp\left(-iknz(\xi, \eta)\right) . \tag{2.7}$$

Here, (ξ, η) are the coordinates in the sample plane, n is the complex index of refraction, $k = 2\pi/\lambda$ is the wave-vector and $z(\xi, \eta)$ the local sample thickness.

Often, a plane wave sufficiently models the incident illumination:

$$E_0 = \text{const.} \tag{2.8}$$

This is particularly the case for weakly focused beams or when the distance to the focal position is sufficiently large.

Gaussian beams are useful when it is necessary to include the evolution of a focused beam into the simulation. Such a beam – propagating along the z-axis and with a waist diameter w_0 at z_0 – is given by [33]:

$$E_\mathrm{G}(r, z) = \frac{w_0}{w(z)} \exp\left(-\frac{r}{w(z)}\right)^2 \exp\left(-i\frac{kr^2}{2R(z)}\right) \tag{2.9}$$

with $r = \sqrt{\xi^2 + \eta^2}$ and

$$w(z) = w_0\sqrt{1 + \left(\frac{z - z_0}{z_\mathrm{R}}\right)^2} \tag{2.10}$$

$$R(z) = z\left(1 + \frac{z_\mathrm{R}}{z}\right)^2 \tag{2.11}$$

$$z_\mathrm{R} = 2\pi\frac{w_0^2}{\lambda} \tag{2.12}$$

Here, $w(z)$ is the waist diameter at position z, $R(z)$ is the curvature of the wave-front and z_R the Rayleigh-length.

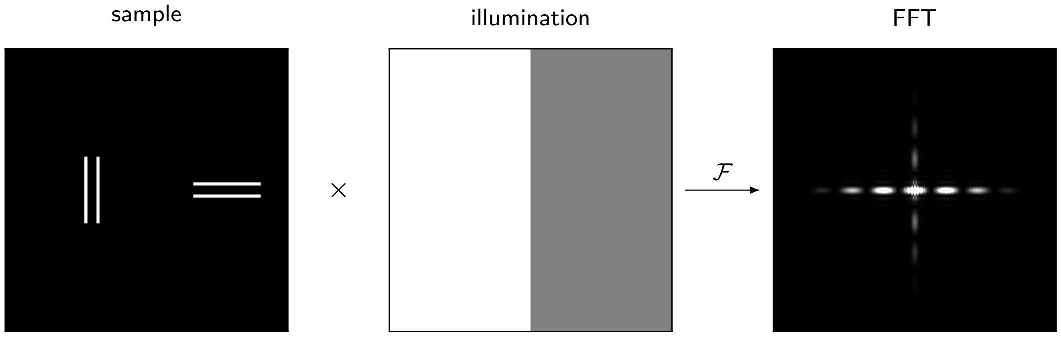

Figure 2.6.: Schematic of the simulation process. We multiply a given sample transmission (left) with an illumination function (center). The Fourier-transform ($\mathcal{F}$) of this product yields the far-field diffraction pattern (right). In the shown example, two equivalent double slits with perpendicular orientation produce a horizontal and vertical diffraction pattern. The vertical stripes in the diffraction image correspond to the horizontal double slit. Since the illumination on this part of the simulated sample is weaker, the corresponding diffraction is less bright as well.

2.7.2. Fraunhofer diffraction

Within the Fraunhofer approximation, the scattered intensity in reciprocal space is the squared magnitude of the exit-wave's Fourier transform. For a round aperture with diameter D and a photon wavelength λ, this approximation requires that the detector distance z_{det} satisfies [33]

$$z_{\text{det}} > \frac{2D^2}{\lambda}\,. \tag{2.13}$$

In order to calculate the diffraction pattern for a given sample, we generate a numerical grid of $N \times N$ points to represent the sample plane. With the total sample size s, the real-space resolution (i.e. the pixel size) is

$$d_{\text{px}} = s/N\,. \tag{2.14}$$

Conversely, the maximum momentum transfer in the simulation is

$$k_{\text{max}} = \pm\pi/d_{\text{px}}\,. \tag{2.15}$$

We employ the fast Fourier-transform (FFT) algorithm to numerically calculate the far-field diffraction pattern for a given sample. Fig. 2.6 schematically illustrates the simulation procedure for a double slit sample with inhomogeneous illumination.

2.7.3. Free-space propagation

The far-field condition of Eq. (2.13) – although not a strict boundary – defines the minimum detector distance for which the diffraction pattern of a sample is given by the Fourier transform of the exit-wave. Many of the experiments in this thesis use samples of 35 µm × 35 µm size and a photon wavelength of 20.4 nm. Here, the required object–detector distance already exceeds 12 cm, limiting the detectable momentum transfer to $\pm 35\,\mu\text{m}^{-1}$. In order to increase this range, these experiments use a smaller detector distance and deviations from the calculated Fraunhofer diffraction pattern are to be expected. Moreover, some experiments in this work employ apertures in close vicinity to the sample in order to define the incident illumination. In such cases, near-field diffraction governs the effective illumination function on the sample.

Free-space propagation [33] yields the electric field $E(\mathbf{r}, z)$ in the $\mathbf{r} = (x, y)$ plane at distance z after the diffracting object:

$$E(\mathbf{r}, z) = \mathcal{F}^{-1}\left[\mathcal{F}\left[E(\mathbf{r}, 0)\right] \exp\left(-ik_z(k, k_x, k_y)z\right)\right] \tag{2.16}$$

where

$$k_z(k, k_x, k_y) = -i\sqrt{k_x^2 + k_y^2 - k^2} \tag{2.17}$$

$$k = \frac{2\pi}{\lambda} \tag{2.18}$$

$\mathcal{F}$ ($\mathcal{F}^{-1}$) denotes the (inverse) Fourier transform, $k_{x,y}$ is the momentum transfer corresponding to a given coordinate in the (x, y) plane and λ is the photon wavelength.

This allows us to numerically calculate the near-field diffraction for arbitrary two-dimensional structures. The fixed pixel resolution in the simulation effectively limits the maximum propagation distance as the simulated area needs to be large enough to accommodate the diffracted intensity. As an example, Fig. 2.7 shows the diffracted intensity after a double slit structure at various positions in the near-field.

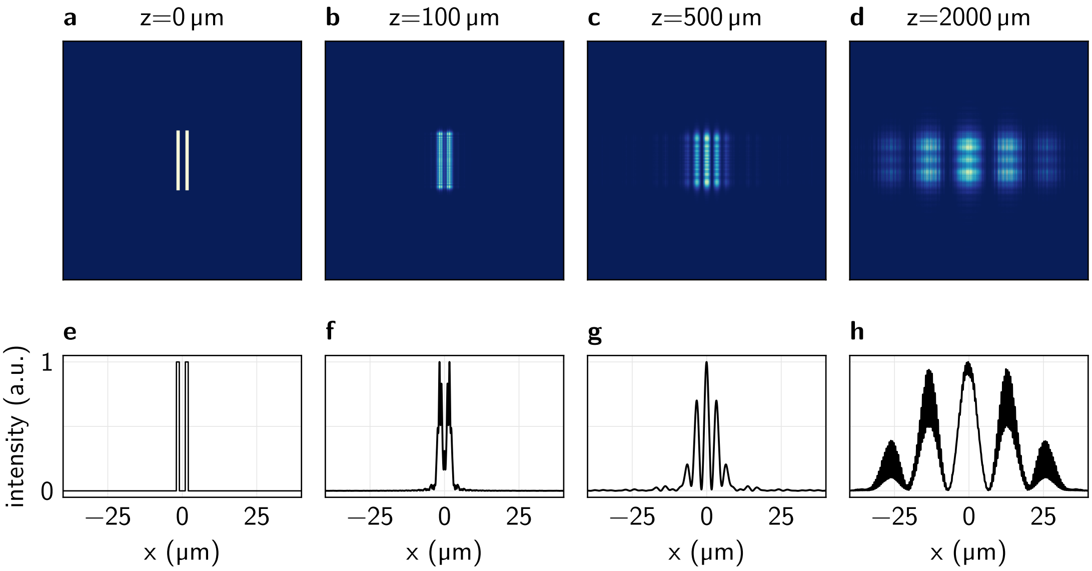

Figure 2.7.: Near-field propagation of a double slit. Simulated diffraction pattern after a double slit of 1 µm slit width and 2 µm separation under plane-wave illumination. The photon wavelength is 20.4 nm and propagation distances z are given on top of the respective diffraction patterns. **a)-d)** Simulated diffraction pattern. The total simulation area is 40 µm × 40 µm. **e)-h)** Line scans perpendicular to the slit direction. The series shows the evolution of the diffracted intensity into the signature double-slit interference pattern. Aberrations occur at larger propagation distances, i.e. when the simulated area is too small for the diffraction pattern. Likewise, an insufficient pixel resolution creates aberrations as well, as evidenced by the incompletely modulated interference pattern in (h). Both limitations – large simulation area and small pixel size – result in quickly growing computation memory demands for increasing propagation distances.

Part II.

In-situ fluence monitoring

3. Influence of the spatial fluence distribution

The introduction to this thesis outlines why the spatial fluence distribution on the sample is such a complex and fluctuating quantity at FEL sources. The aim of this section is to briefly illustrate how the detailed distribution affects measured signals with a non-linear fluence dependence. Let us consider three different fluence distribution estimates of a strongly focused FEL beam with a complex, non-Gaussian beam: (i) The actual, non-Gaussian distribution (Fig. 3.1a). (ii) A blurred distribution, as obtained by a knife-edge or aperture scan (Fig. 3.1b). Such scans are routinely used to approximately determine the fluence distribution in the sample plane. The resulting maps are inevitably multi-shot averages and are thus blurred due to shot-to-shot noise and the convolution with the aperture size. (iii) A constant distribution over a certain area or, equivalently, the characterization by a single "spot size" number (Fig. 3.1c). The different distributions affect the measured signal level $I(f)$ that a non-linear process causes for the same overall shot energy. Here, we calculate the signal levels assuming a linear, power-law and a saturating fluence dependence. These relationships are prevalent in many high-intensity light–matter interactions. While a linear relationship is typical for the low-fluence regime, a power-law is often associated with multi-photon absorption at higher photon fluences [60]. Saturation behavior has been reported in a number of FEL experiments, e.g. due to stimulated emission [10] or saturable absorption [61]. †

As expected, the signal in the linear case (Fig. 3.1e) only depends on the total shot energy and is independent of the distribution. For a power-law dependence the slope in a double-logarithmic plot (Fig. 3.1f), i.e. the observed exponent, is unaffected by the fluence distribution. However, this is only the case if the signal has no other dependencies, such as a linear background. In any case the approximate distributions obfuscate the particular signal level, which is relevant for quantitative analysis. Finally, with a saturating fluence behavior (Fig. 3.1g), the correct saturation point f_s and level $I(\infty)$ cannot be determined without the exact fluence distribution.

Thus, a correct interpretation of fluence dependent measurements will only be possible with an accurate, *in-situ* characterization of the incident photon distribution $I(\xi, \eta)$ on the sample on a shot-by-shot basis. The following sections describe the development of such a simultaneous measurement of the spatial fluence distribution on the sample in conjunction with a diffraction signal from a solid sample in a single-shot XUV FEL experiment. The measurement scheme is derived from work on monolithically integrated gratings on carrier membranes [1]. The structures obtained were found to be equivalent to zone-plates under off-axis illumination [62]. The demonstrated integrated diffraction monitor design is able to map the incident photon distribution on the sample to the

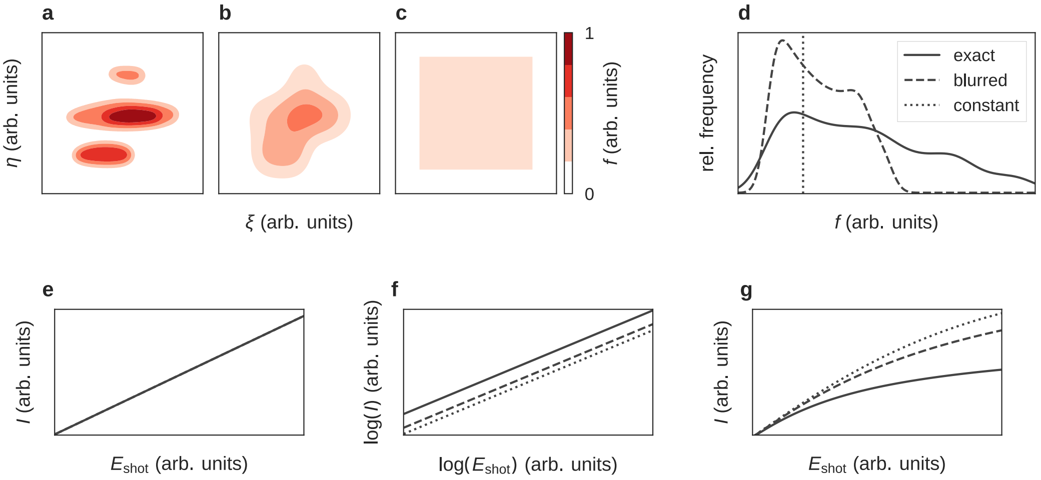

Figure 3.1.: Examples of spatial fluence distribution estimates. Simulated two-dimensional maps of the spatial fluence distribution in the sample plane ($f(\xi, \eta)$), representing **a)** an exact measurement, **b)** a blurred, low-resolution measurement and **c)** a constant estimate. All maps sum to the same overall shot energy E_{shot}. **d)** Fluence histograms of the three maps in a) – c). **e)–g)** Simulated scattering signal $I(f)$ for increasing integral shot energy in the three fluence distributions under the assumption of, respectively, linear, quadratic and saturating fluence dependence. Note the double logarithmic scale in **f)** †.

detector plane. There, the illumination is recorded simultaneously with the sample's scattering signal. †

4. Development of the grating monitors

The fundamental concept of this work is to utilize routinely used carrier membranes in diffraction experiments as a fluence monitor by outfitting them with a purposely designed grating. Over the course of this thesis, this concept developed from an empirically developed, integral intensity monitor (without spatial resolution) to a thoroughly understood and well-controlled tool to map spatial fluence distributions *in-situ*. This thesis does not aim to retrace this lengthy process. However, some aspects of the integral fluence monitors are still relevant for special applications. Most importantly, the fluence-dependent experiments in the second part of this thesis utilize integral fluence monitors. The present chapter thus includes corresponding results and their discussion. For clarity, the empirical grating design formula is omitted. The next section derives the design formula for spatially resolving grating monitors. This formula encompasses the earlier grating designs.

4.1. Derivation of the distorted grating formula

Fig. 4.2 sketches the fundamental idea of the concept as a step-wise evolution from regular, to segmented, and finally to the spatially resolving gratings discussed here. The basic situation is an FEL diffraction experiment that detects scattered radiation as a function of momentum transfer $\mathbf{q}$ on a 2D pixelated detector (Fig. 4.1). Note that this geometry also includes standard spectroscopy of the photon beam, where the beam at a selected momentum transfer (such as $q = 0$) is detected as a function of wavelength. In material and life sciences, thin membranes of $\mathrm{Si_3N_4}$, Si or polymers are commonly used to administer samples to the FEL beam. We equip these membranes with a grating structure, that gives rise to an additional scattering signal at a selected detector position [1]. The key idea of this work is to design the gratings such that each point on the sample surface diffracts the incoming light to a separate position on the detector while preserving the spatial relationship of the originating sample points. †

We start with the following sinusoidal transmission function for a regular grating [33]:

$$t(\xi, \eta) = \frac{1}{2} + \frac{1}{2}\cos\left(\frac{2\pi}{p}\left(\xi\cos(\varphi) + \eta\sin(\varphi)\right)\right) \tag{4.1}$$

Here, ξ and η are spatial coordinates in the sample plane, while p and φ are the grating period and orientation angle, respectively. They are given by the position (x, y, z_{det}) of

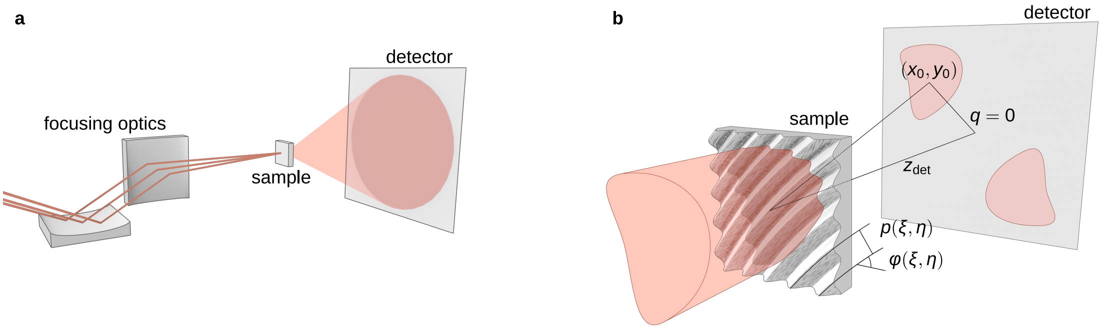

Figure 4.1.: Experiment geometry and sample design. **a)** An optical system focuses the incoming beam (red lines) onto the sample. Downstream, a 2D pixelated detector records the scattered radiation (red cone). **b)** Enlarged view of the sample and the scattering geometry. The sample bears a suitably tailored, continuously varying grating with local periodicity $p(\xi, \eta)$ and local orientation angle $\varphi(\xi, \eta)$, where ξ and η are the coordinates in the sample plane. Incident light is diffracted away from the undeflected beam ($q = 0$) with a momentum transfer of $\pm\mathbf{q}(p, \varphi)$ according to the local grating parameters. We design the grating such that it maps an enlarged image of the incident illumination, centered around $\pm(x_0, y_0)$ in the detector plane at distance z_{det}.[†]

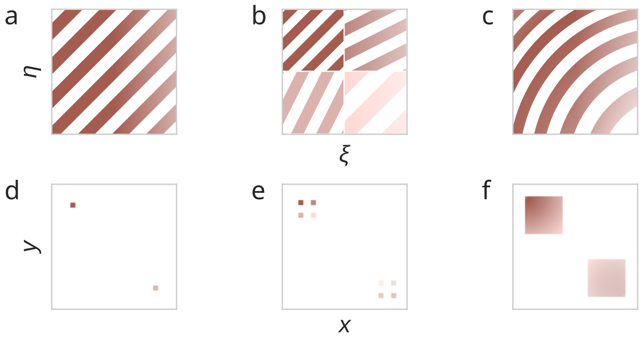

Figure 4.2.: Schematic evolution of our grating design from regular gratings. The images show the real-space structures (a–c) and respective diffraction pattern (d–f). **a)** A regular grating diffracts incoming light to two symmetric points in Fourier-space (d) and hence reveals no spatial information on the illumination function. **b)** A two-by-two segmented grating yields two symmetric sets of four diffraction spots (e). The intensity of each spot is proportional to the illumination of the corresponding sample quadrant. This constitutes the most basic form of a spatially resolving beam profile monitor based on an integrated grating. **c)** A grating with suitably varying period and orientation forms a magnified image of its own illumination in Fourier-space (f). The colors in the real-space images indicate the local grating period and mark the corresponding points in the diffraction images.[†]

the grating's first diffraction order in the detector plane:

$$\varphi = \arctan(y/x) \tag{4.2}$$

$$p = \frac{\lambda}{\sin\left(\arctan\left(\sqrt{x^2+y^2}/z_{\mathrm{det}}\right)\right)}\,. \tag{4.3}$$

We turn φ and p into functions of the sample coordinates by setting

$$x = x_0 + m\xi \tag{4.4}$$

$$y = y_0 + m\eta\,. \tag{4.5}$$

Inserting this into Eq. (4.1), results in a grating with continuously varying pitch and orientation. It diffracts an image of its own illumination function, magnified by the dimensionless parameter m and centered at (x_0, y_0), to the detector. †

In simulations with Gaussian beams we observe, that the following condition must be satisfied (see detailed discussion in the following sections):

$$\frac{z_{\mathrm{det}}}{m} < 2\pi\frac{w_0^2}{\lambda}\,, \tag{4.6}$$

where w_0 is the smallest feature size in the spatial fluence distribution to be resolved. This relation enforces that the illumination does not change drastically within a small number of grating periods, which would lead to errors in the diffracted fluence maps.†

4.2. Relationship between grating design and resolution limits

This section discusses the design principles of the grating monitors, their imaging capabilities and possible aberrations. Two different approaches yield equivalent perspectives on these structures: They may either be treated as segments of zone-plates, or as modified regular gratings. Both approaches provide established theoretical frameworks and are adapted to the case at hand. This, and additional numerical simulations enable a consistent and comprehensive understanding of the grating monitors' behavior, their fluence mapping capability and limitations.

4.2.1. Relationship to zone-plates

All gratings obtained through Eq. (4.1) are segments of Fresnel zone plates. This can readily be verified by inspecting gratings whose diffraction center is coaxial with the illuminating beam, i.e. by setting $x_0 = y_0 = 0$, as shown in Fig. 4.3a. †

A modified transmission function

$$t(\xi,\eta) = \frac{1}{2} + \frac{1}{2}\cos\left(\frac{2\pi}{p}\left(\xi\sin(\varphi) + \eta\cos(\varphi)\right)\right) \tag{4.7}$$

yields hyperbolic zone-plate structures instead (Fig. 4.3b). Both types of grating moni-

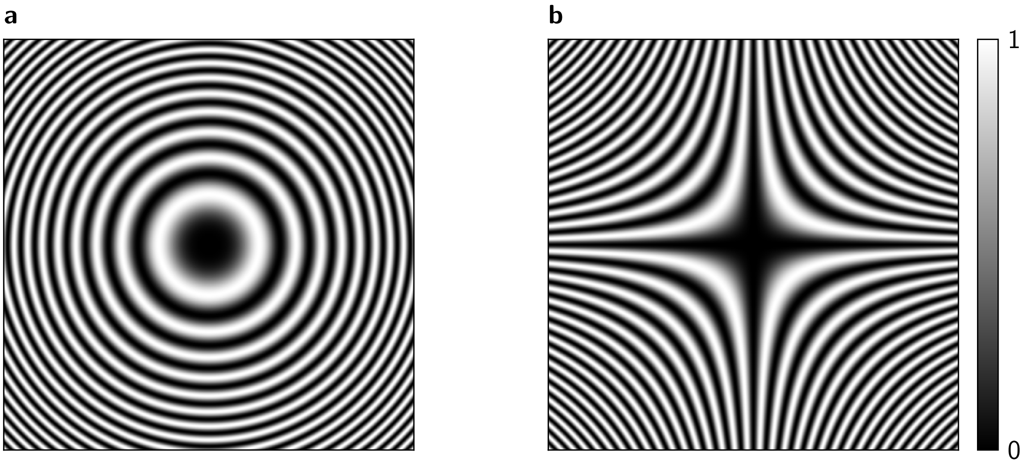

Figure 4.3.: Grating monitors as zone-plate segments. **a)** Fresnel-type grating monitor with transmission function given in Eq. (4.1) and x_0=y_0=0. **b)** The same parameter set yields a hyperbolic zone plate when Eq. (4.7) is used instead.

tors are capable of mapping the sample illumination. They have slightly different mapping properties that make them more or less suitable for specific cases, as discussed in the following sections.

The radius of the n-th zone of an equivalent zone-plate is [63]

$$r_n = \sqrt{n\lambda f}\,. \tag{4.8}$$

Where the focal distance f is related to our grating parameters by

$$f = \frac{z_{\mathrm{det}}}{2m}\,. \tag{4.9}$$

Thus, we may understand the working principle of a grating monitor as a lens that maps the illumination in a close-by object plane (located at $f = z_{\mathrm{det}}/2m$ relative to the grating position) to a far-away image plane. †

Leveraging the grating parameters, we can ensure that the focal distance does not exceed the Rayleigh-length for a – presumably Gaussian – focused spot of waist size w_0, given by

$$z_{\mathrm{R}} = \frac{\pi w_0^2}{\lambda}\,. \tag{4.10}$$

Demanding that $f < z_{\mathrm{R}}$ ensures that the object plane is close enough to the sample plane to preclude any significant difference of the illumination between both planes. This directly yields the mentioned condition for the grating design:

$$\frac{z_{\mathrm{det}}}{m} < 2\pi \frac{w_0^2}{\lambda} \tag{4.11}$$

This result has a very illustrative interpretation: Since Eq. (4.11) forbids to increase the detector distance arbitrarily, smaller grating structures are necessary to sufficiently separate the fluence map from the main beam. This ensures that the grating features are always considerably smaller than the beam footprint, and thus, that the illumination does not change drastically within a small number of grating periods. Such a limit is to be expected, since our derivation of the grating formula starts with the assumption of a well-defined diffraction spot from a regular grating, which requires a minimum number of illuminated grating periods. [†]

4.2.2. Fraunhofer simulations on Fresnel- and hyperbolic gratings

This section relies on the simulation procedure outlined in Section 2.7.2. Specifically, it investigates the diffraction pattern of various combinations of the diffracting structure and its illumination. The simulated grating parameters are constant, and illumination functions that are increasingly smeared out represent a more or less rapidly changing beam footprint. Here, the basic shape of the illumination intentionally includes horizontal, vertical and diagonal edges as well as sharp corners to systematically identify differences in the fluence mapping of both, hyperbolic and Fresnel-type gratings.

Fig. 4.4 shows details of a series of simulated diffraction images with increasingly "soft" illumination functions. The details correspond to the positive diffraction order. Note that for the hyperbolic grating structures, the diffracted fluence maps are rotated by 90° in order to align them the simulated illumination function. It is evident that both grating types yield a direct and faithful map of this illumination function, as long as the simulated beam footprint does not change drastically within a few grating periods. This condition can typically be well fulfilled in XUV and soft x-ray experiments at synchrotron and FEL sources with focused beam sizes ranging from a few to some tens of micrometer and a grating periodicity of 60 nm to 200 nm. Due to the large range of possible grating parameters, it is useful to refer to the steepness of an illumination function in multiples of the smallest grating period (p). Steep intensity gradients, the full width at half maximum (FWHM) of which spans less than ten grating periods, are encountered at the sample boundaries or in close proximity behind apertures. They lead to an intensity ringing with an amplitude that is comparable to that of the simulated illumination gradient. Hyperbolic gratings are much less susceptible to intensity ringing in the horizontal and vertical directions. Accordingly, they can image steeper intensity gradients in these directions than the Fresnel-type gratings. For diagonal intensity gradients, both grating types perform similarly. [‡]

4.2.3. Zone-plate perspective

As discussed in Section 4.2.1, the grating monitors act as zone-plates that image the illumination in a close-by object plane to the detector at much greater distance. This implies, that the mapped illumination function may differ from the actual illumination when their focal length (f) exceeds the Rayleigh-length. To verify this interpretation of the grating behavior, this section investigates the far-field diffraction pattern of Fresnel-

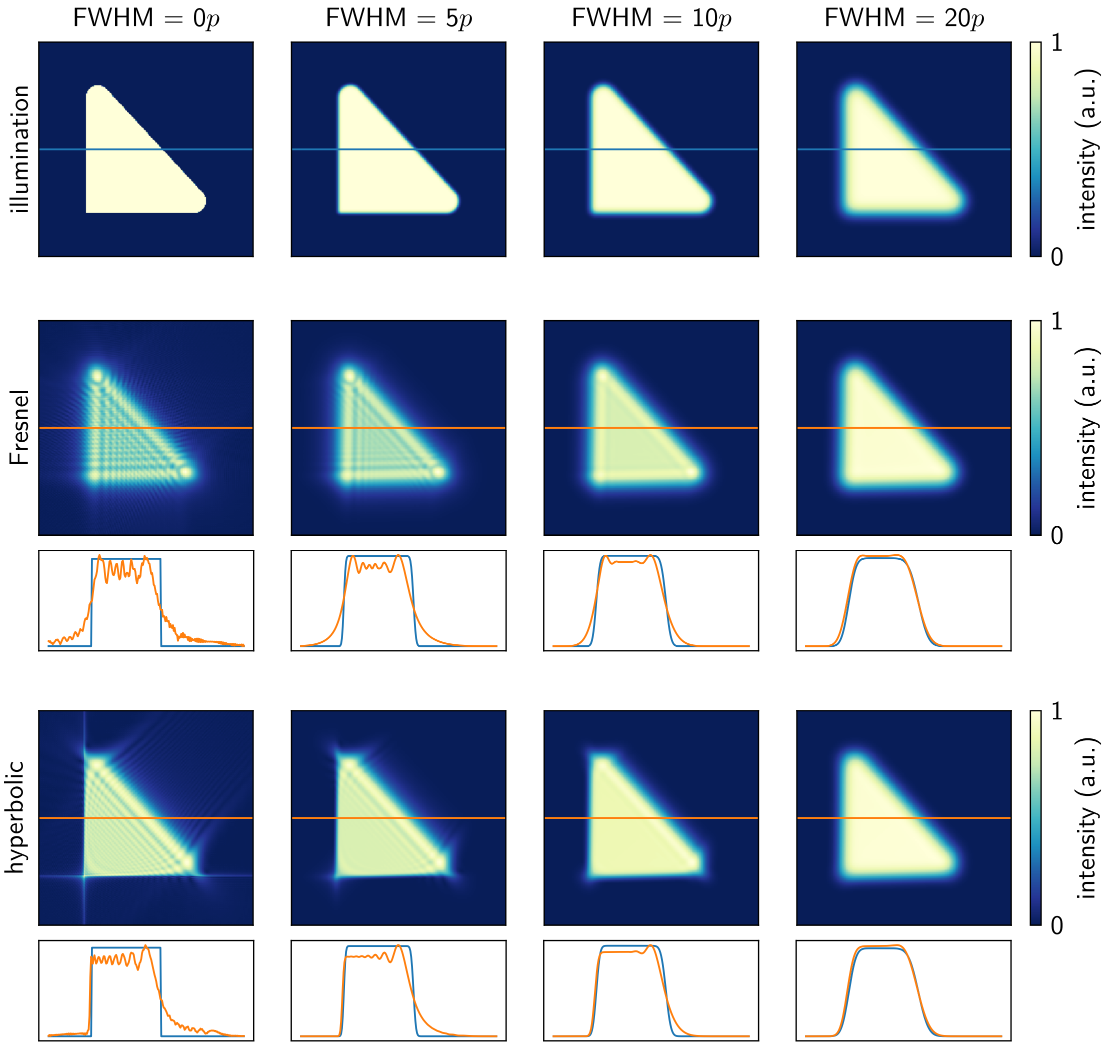

Figure 4.4.: Simulated Fraunhofer diffraction of Fresnel- and hyperbolic gratings. Top row: simulated illumination profile. The convolution with a Gaussian kernel of variable width provides increasingly smooth illumination footprints. The actual widths (FWHM) are given in multiples of the median grating period p on top of the respective images. Middle and bottom row: Diffracted fluence maps of the Fresnel-type and hyperbolic grating, respectively. For increased clarity, the diffraction images are details, limited to the positive first diffraction order. The line plots show the intensity along the colored markers in the diffraction images (orange) and the simulated illumination (blue). For both grating types, very steep intensity gradients (less than 10 grating periods FWHM) produce diffraction artifacts. In the case of the Fresnel-type gratings, these artifacts are isotropic and become tolerably small when the illumination gradient extends over more than 10 grating periods (FWHM). The hyperbolic gratings show a similar level of diffraction artifacts along the diagonal directions. In horizontal and vertical directions however, their resolution is better than 5 grating periods. ‡

grating		**sub-beam 1**		**sub-beam 2**
λ	20.8 nm	λ	20.8 nm	20.8 nm
x_0	8 mm	w_0	3 µm	2 µm
y_0	8 mm	z_0	0 µm	0 µm
z_{det}	30 cm	x_c	−2 µm	3 µm
m	250	y_c	0 µm	0 µm

Table 4.1.: Grating and beam parameter used in the simulations. The parameters are for a Fresnel-type grating that intentionally violates Eq. (4.11).

type grating monitors when illuminated by Gaussian beams. Using Gaussian beams provides a direct way to compare the diffracted fluence maps with the expected beam profile at various positions along the propagation axis. Furthermore, using the sum of two beams with different center positions $(x_{\mathrm{c}}, y_{\mathrm{c}})$ breaks the rotational symmetry of a single Gaussian beam around its center. This makes it easier to unambiguously correlate the diffracted intensity in the simulation with the respective beam positions. The beam and grating parameters are summarized in Table 4.1.

They intentionally violate Eq. (4.11) in order to demonstrate the aberrations that occur in this case. Specifically, they fulfill

$$z_{\mathrm{det}} = 2m\pi\frac{w_0^2}{\lambda} = 30\,\mathrm{cm} \tag{4.12}$$

and thus

$$f = \frac{z_{\mathrm{det}}}{2m} = 0.6\,\mathrm{mm}\,. \tag{4.13}$$

Fig. 4.5 shows the calculated beam profiles at the focus ($z = 0\,\mathrm{mm}$), and at $1f$ and $2f$. The beam profile at $1f$ is used as illumination function for the simulated grating monitor. In the resulting diffraction pattern, the positive and negative diffraction orders are not point-symmetric with respect to the diffraction image's center. Neither of them matches the simulated illumination function. Instead, the two diffraction orders map the beam profiles at $z \pm f$, i.e. one focal length of the equivalent zone-plate (Eq. (4.9)) away from the grating position.

It is thus clear, that the physical grating position (i.e. the sample plane) does not coincide with the object plane (the illumination of which the grating maps). This is not an issue as long as the distance between sample- and object plane is sufficiently small with respect to the rate at which the beam profile changes along its propagation axis. In this context, the magnification factor m at a fixed detector distance z_{det} is the most important grating design parameter to ensure a valid fluence mapping.

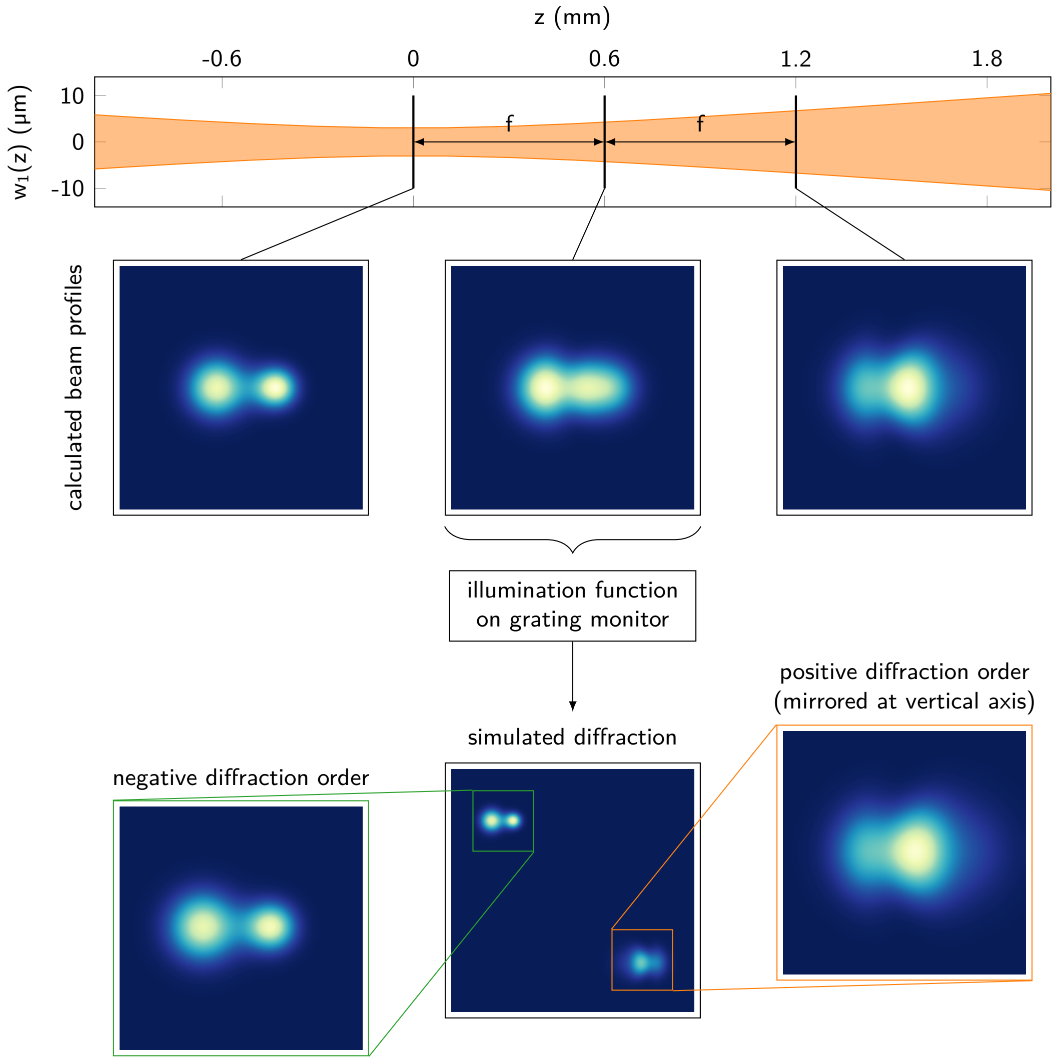

Figure 4.5.: Simulation of the object plane shift along the propagation axis. Top: Plot of the beam diameter for the Gaussian sub-beam 1 along its propagation axis. Beam parameters are given in Table 4.1. First image row: Calculated spatial fluence distributions (Eq. (2.9)) at the focus (z=0 mm), and at 1f and 2f (z=0.6 mm and $z = 1.2$ mm, respectively) along the beam propagation axis. Image extents are 20 µm × 20 µm. Bottom row: Simulated diffraction pattern of a grating monitor, illuminated by the z=0.6 mm beam profile. The bright center pixel of the simulated diffraction pattern is manually set to zero in order to enhance visibility of the positive and negative diffraction orders. These are shown in the enlarged details to the left and right of the diffraction pattern. Evidently, they do not map the illumination of the simulated sample plane (z=0.6 mm). Instead, they correspond to the ones that are one focal length of the equivalent zone-plate (f) away, as the comparison with the directly calculated beam profile shows. All images are normalized to the value range [0,1] and plotted on the same linear false color scale as used in Fig. 4.4.

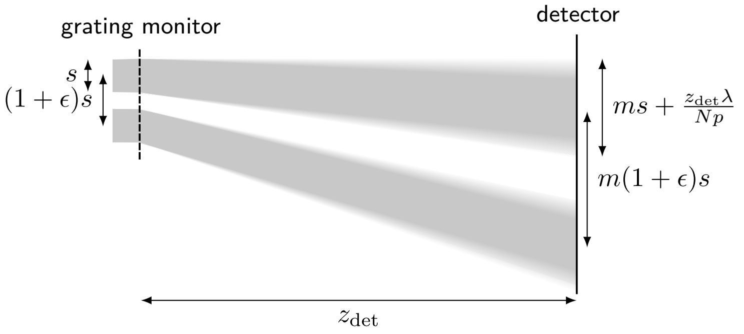

Figure 4.6.: Resolution estimate in the grating picture. Two separate, spatially localized beams of size s and with separation $(1+\epsilon)s$ are incident on a grating given by Eq. (4.1). Given the (local) lattice constant p, each beam footprint illuminates $N = s/p$ grating periods. The grating diffracts an m-fold enlarged image of this illumination function to the detector plane at distance z_det. Here, the diffracted beams are smeared out due to the finite number of illuminated lines. The amount of this broadening increases for smaller beam footprints. This effectively limits the attainable spatial resolution.

4.2.4. Grating perspective

It is not strictly necessary to treat the grating monitors as zone-plates in order to assess their resolution limits. A similar expression to Eq. (4.11) can be derived by considering under what circumstances two localized beams of width s and at lateral distance $(1+\epsilon)s$ will still be distinguishable in the diffracted fluence map. This approach is similar to the estimation of the spectral resolution of a grating monochromator.

In the detector plane at distance z_det, all sizes and distances are scaled by the magnification factor m, according to the grating design. Additionally, the diffracted beams are smeared out by the width w of the principal maximum of a grating with finite number of illuminated lines [33], as sketched in Fig. 4.6:

$$w = \frac{\lambda z_\mathrm{det}}{Np} \tag{4.14}$$

Here, p is the grating periodicity, N the number of illuminated lines and λ the photon wavelength. The grating period of course depends on the coordinate (ξ, η) in the sample plane for any $m > 0$. Since this variation is small within the extent of the beam footprint, treating p as a constant is justified in order to simplify this resolution estimate.

Separating both beam footprints requires that

$$(1+\epsilon)ms \geq ms + \frac{z_\mathrm{det}\lambda}{Np} \tag{4.15}$$

$$\epsilon ms \geq \frac{z_\mathrm{det}\lambda}{Np}\,. \tag{4.16}$$

In small-angle approximation, p is given by:

$$p \approx \frac{z_{\mathrm{det}}\lambda}{r} \tag{4.17}$$

$$r = \sqrt{(x_0 + m\xi)^2 + (y_0 + m\eta)^2} \quad . \tag{4.18}$$

And thus

$$N \geq \frac{r}{\epsilon m s} \tag{4.19}$$

The number of illuminated lines is $N = s/p$, resulting in

$$p \leq \frac{m s^2}{\epsilon r} \tag{4.20}$$

This is a rough estimate that, for example, depends on what distance is considered distinguishable. Expressing Eq. (4.20) in terms of the detector distance (i.e. by again substituting $p = \lambda z_{\mathrm{det}}/r$), yields an identical expression to Eq. (4.11) for $\epsilon = 1/(2\pi)$, demonstrating that both perspectives are equivalent. †

$$\frac{z_{\mathrm{det}}}{m} \leq \frac{1}{\epsilon}\frac{s^2}{\lambda} \tag{4.21}$$

4.3. Aberrations

4.3.1. In the near-field

Since Eqs. (4.2) and (4.3) relate to far-field diffraction, the mapping is only valid if the detector is sufficiently far away from the sample to be in the Fraunhofer regime [33], i.e.

$$z_{\mathrm{det}} > 2\frac{w_0^2}{\lambda} \,, \tag{4.22}$$

where w_0 is the beam's waist size on the sample.

According to this, z should at least be 118 mm for an XUV experiment with $\lambda = 20.8\,\mathrm{nm}$ and a fully illuminated grating with $D = 35\,\mu\mathrm{m}$ edge length. However, a large distance from sample to detector limits the accessible in-plane momentum transfer for a given detector size L, since only scattering angles θ smaller than

$$\theta_{\max} = \arcsin\left(\frac{L}{2z}\right) \tag{4.23}$$

can be detected. In the above example, and with the detector size of the experiments in this thesis ($L = 27.65\,\mathrm{mm}$), this corresponds to a diffraction-limited spatial resolution of only 350 nm. The sample-to-detector distance in experiments is therefore often considerably smaller and deviations from the Fraunhofer diffraction pattern are to be expected. In order to identify such aberrations, this section discusses the near-field diffraction pattern of uniformly illuminated hyperbolic and Fresnel-type gratings. The diffraction pattern is calculated by free-space Fourier propagation (see Section 2.7.3).

The intensity at distance z behind a diffracting structure is the squared magnitude of the propagated electric field $E(\mathbf{r}, z)$. Fig. 4.7 shows this diffracted intensity for Fresnel-type and hyperbolic gratings at different propagation distances. The simulation uses tabulated optical constants for Si_3N_4 [9] to calculate the complex exit-wave for a plane wave passing through a grating with 2 nm topographic amplitude on a 30 nm thick membrane. The gratings in the calculation are square with 25 µm edge length and have the following parameters: $m = 10$, $x_0 = y_0 = 1\,\mathrm{mm}$ and $z_{det} = 8\,\mathrm{cm}$. The diffraction pattern is calculated on a grid of 8192×8192 points, representing a total area of $270\,\mu\mathrm{m} \times 270\,\mu\mathrm{m}$.

The image series in Fig. 4.7 shows the evolution of the wave-front into the positive and negative diffraction orders immediately after passing the grating ($z = 0\,\mathrm{mm}$). The corresponding to the foci of the underlying zone-plate structure In the case of the Fresnel grating, both diffraction orders remain undistorted, although at first only the size of the positive order increases, while the negative diffraction order contracts before eventually expanding again. In this fashion, the wave-field continuously approaches the centrosymmetric diffraction pattern in the Fraunhofer, i.e. far-field regime. Crucially, the fluence map of at least one diffraction order yields usable information throughout the whole propagation distance. The hyperbolic grating shows a similar behavior. However, the evolution here also has to accommodate a rotation of the fluence map by 90° on the way to the final far-field diffraction pattern. As a consequence, both diffraction orders are sheared into trapezoid shapes. At a certain distance, the distortion becomes so severe, that only elongated stripes are observed, which yield no practical information on the grating's spatial illumination profile.

It is clear that the grating type has to be taken into account when considering the grating parameters for a particular experiment. As discussed in Section 4.2.2, hyperbolic gratings are less error-prone with respect to very steep intensity gradients. However, when the conditions for Fraunhofer diffraction are not fully satisfied, Fresnel-type gratings are the more robust choice.

4.3.2. Geometric Distortion

The grating formula derived in Section 4.1 implicitly assumes that the grating's spatial extent is small compared to the final illumination map in the detector plane. In other words, it supposes that all diffracted intensity emanates from a single point of origin. For very large gratings with comparably small magnification factors, this approximation is no longer valid. In such cases, each point of diffracted intensity in the detector plane (x, y) is offset by its corresponding source point (ξ, η) on the sample, which leads to an apparent shearing of the mapped fluence distribution. This modifies the mapping of the sample to the detector plane, given in Eq. (4.5), to

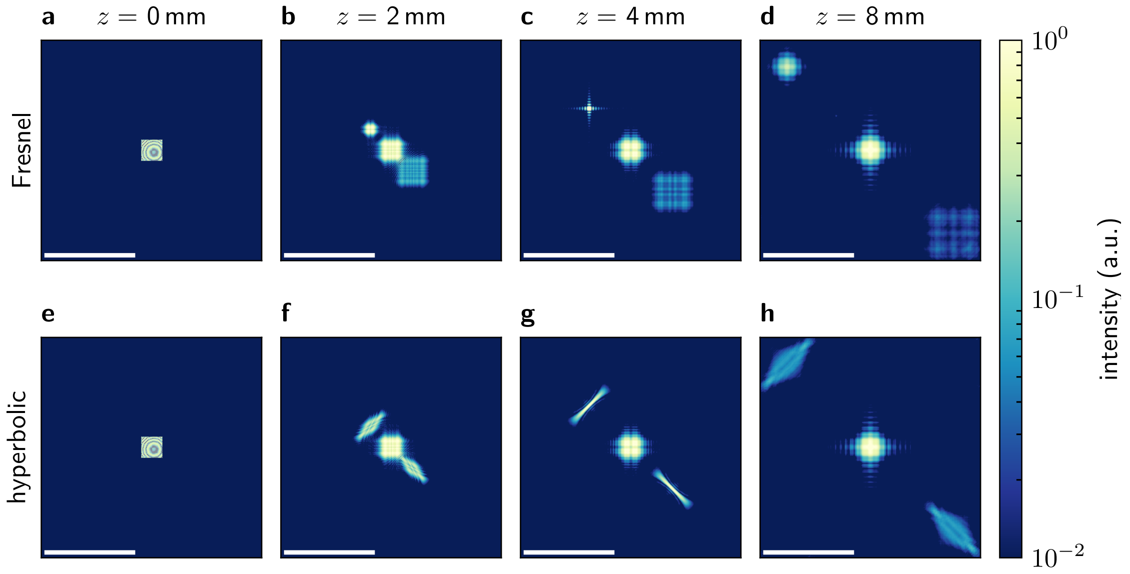

Figure 4.7.: Near-field evolution of the grating diffraction. **a-d)** The Fresnel grating produces undistorted (i.e. not sheared) fluence maps in its near-field. The fluence maps correspond to the positive and negative focal point of the equivalent zone plate. In this case, the upper left diffraction has its focus within the simulation's propagation distance at approximately $z = 4\,\mathrm{mm}$. **e-h)** The hyperbolic grating's fluence maps are sheared, as long as far-field conditions are violated.

$$x = x_0 + m\xi + \xi = x_0 + (m+1)\xi \tag{4.24}$$

$$y = y_0 + m\eta + \eta = y_0 + (m+1)\eta\,, \tag{4.25}$$

The maximum displacement of a single point with respect to the correct mapping is evidently equal to the sample size. It is possible to account for this distortion when generating the grating, but only for one particular sample – detector distance. Given typical parameters for the experiments in this thesis – sample size less than 50 µm and magnification factors of 30 to 100 – this effect is negligible.

5. Experimental Results

After the theoretical treatment, this chapter demonstrates the application of the grating monitor concept in synchrotron and FEL experiments. These experiments fall into two categories – artificial test scenarios and direct application alongside other experiments. The synchrotron experiments generally fall into the first category, and FEL experiments in the latter.

5.1. Grating fabrication

The grating samples in this work are prepared by direct FIB writing, as described in Section 2.6.2. With this approach, it is possible to reliably structure whole membrane windows that are as thin as 30 nm with sizes ranging from 30 µm × 30 µm up to 250 µm × 250 µm. Without the necessity of any additional lithographic steps, rapid prototyping of different structures and the manufacture of hundreds of samples for destructive experiments is viable. #

The typical acceleration voltage for structuring is 30 kV and the beam current and dwell-times are chosen to achieve a processing time of less than 120 s for a single membrane. In the case of 35 µm × 35 µm membranes, milling a single grating takes about 90 s using a beam current of 72 pA. For soft x-ray and XUV radiation, milling the gratings very shallow, as displayed in Fig. 5.1, is sufficient. The shown topographic peak-to-valley amplitude of only 2 nm to 3 nm – as measured by atomic force microscopy – is representative for most of the gratings in this work. The bare, 30 nm thick Si_3N_4 membranes show no sign of charge build-up during the milling process, which would rapidly decrease the spatial resolution. #

5.2. Synchrotron experiments

5.2.1. Matching the diffracted intensities

As discussed in Section 2.4, the limited dynamic range of the CCD detector imposes an upper limit on the ratio by which the intensity of simultaneously detected signals may differ. In order to achieve the best signal-to-noise ratio (SNR), all signal contributions need to yield comparable intensity levels on the detector. In the context of this work, the signals of interest are the XMCD-based scattering signal signal and the fluence map provided by the grating diffraction. Here, the grating design needs to be optimized with respect to the position and intensity of the diffracted intensity on the detector.

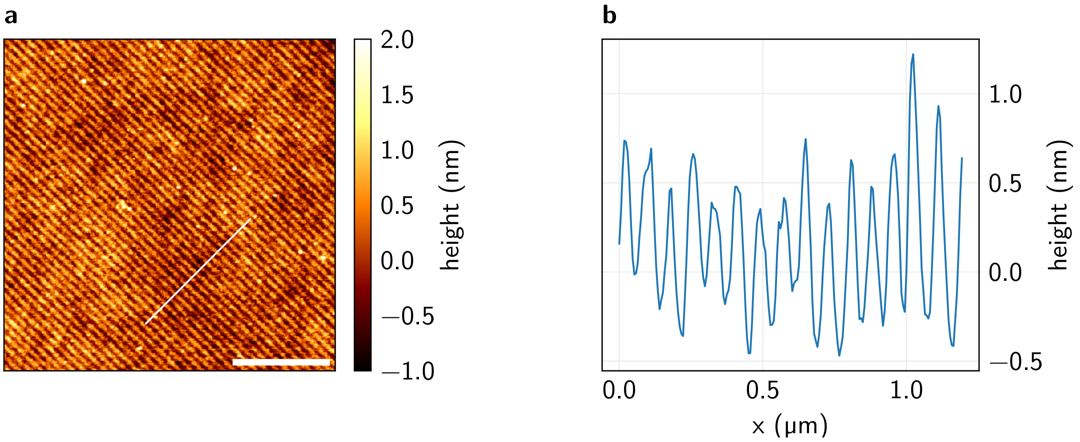

Figure 5.1.: Topography of the fabricated gratings. a) AFM image of a typical grating structure milled into a Si_3N_4 membrane. Scale bar is 1 µm. **b)** The height profile along the indicated line in (a) shows the shallow topographic amplitude of the final grating structure.

The experiment is performed at the UE112-PGM beamline of the BESSYII synchrotron source at a photon energy of 60 eV. This is the same energy as in the FEL experiments that comprise the second part of this thesis. The Si_3N_4 sample membrane bears a FIB-milled curved grating, and a magnetic multi-layer thin-film with composition Ta(15)/ Pd(30)/ $[Co(6)/Pd(7)]_{10}$/ Pd(12). Without any applied field, the sample layer's magnetization state is a labyrinthian pattern of domains with opposite magnetization directions perpendicular to the sample plane. The domains have a characteristic, uniform width and – in this particular case – a slight preference for parallel alignment. Due to the XMCD effect, the magnetic structure gives rise to two circular scattering lobes (see Section 2.3).

Fig. 5.2 shows a series of diffraction images with variable grating parameters on different samples with equivalent magnetic domain structures. The images demonstrate that it is possible to match the diffracted intensities of the grating and the primary sample under study. Here, the diffraction signals unintentionally overlap on the detector. This could be avoided by i) an altered grating periodicity, i.e. placing the grating's diffraction within or without the magnetic signal, or ii) by making sure that the magnetic domains and the principal grating direction are aligned perpendicular to each other. The estimated intensity ratios of grating and XMCD diffraction (I_{gr} and I_{mag}, respectively) are given on top of the respective images. They vary from 250 (grating dominates diffraction pattern, Fig. 5.2a) down to 1 (equal measured intensities, Fig. 5.2d).

5.2.2. Aperture-defined illumination profiles

Aperture-defined illumination functions allow to verify the expected spatial mapping capabilities of the grating monitors. In this experiment, movable apertures directly in front of the grating sample shape the incident illumination in a very controlled fashion. The apertures need to be as close to the sample as possible – about 1 mm in this partic-

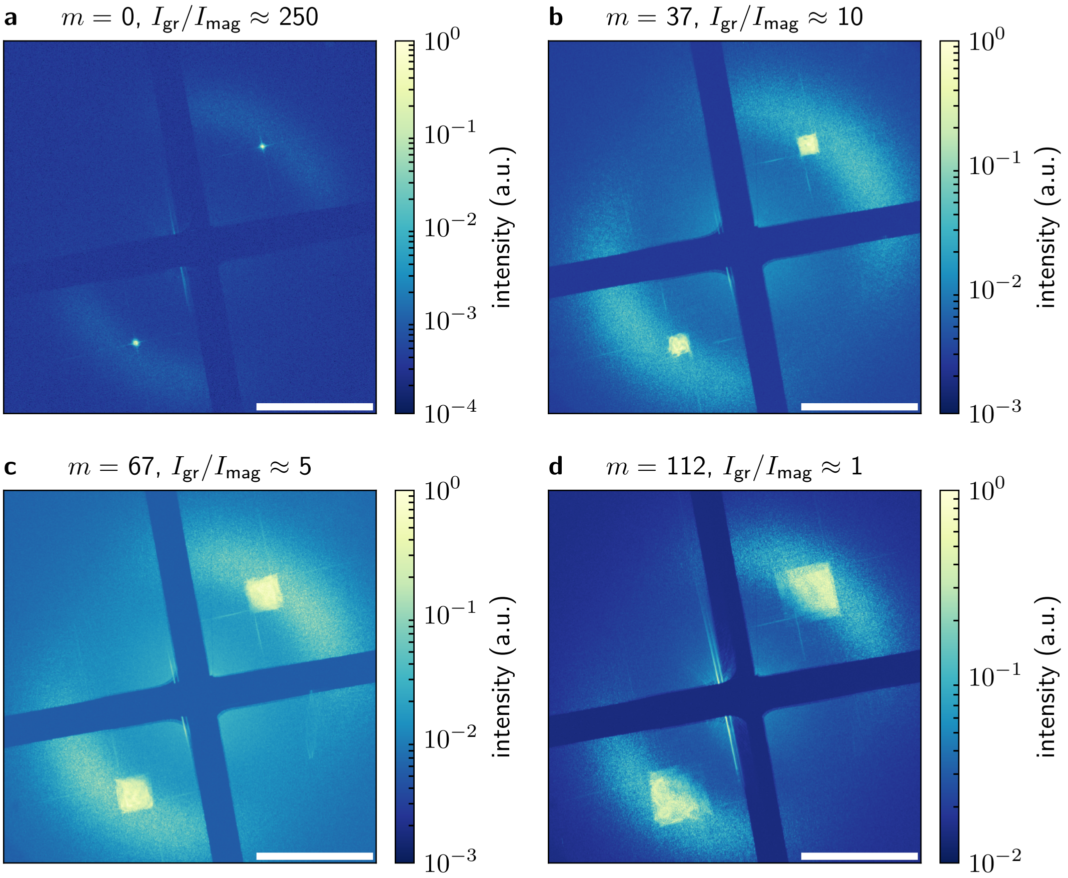

Figure 5.2.: Diffraction images with magnetic and grating diffraction. Each image corresponds to a different sample with comparable magnetic domain state but with a different grating milled into the Si_3N_4 membrane. For each image, the acquisition time is set such that the highest intensity does not saturate the CCD detector. The respective magnification factor m and resulting ratio of grating- and magnetic XMCD diffraction is given on top of the images. Scale bars correspond to a momentum transfer of 40 µm^{-1}. **a)** A regular (Bragg-type) grating (magnification factor $m = 0$) produces a sharp peak of high intensity, entirely dominating the diffraction pattern. **b)** – **d)** With increasing m, the grating distributes the diffracted intensity over a larger area. Thus, the CCD is able to detect both signals – magnetic and grating diffraction – with comparable SNR. #

ular experiment – to avoid diffraction effects from the aperture modulating the fluence distribution on the grating. Thus, the illumination function on the sample is principally given by the aperture's shape. A motorized sample stage positions and scans the aperture with sub-micrometer accuracy. This yields a direct comparison of the known aperture shapes, sizes and positions with the diffracted intensity maps.

The experiment is conducted at the UE52-SGM beamline of the BESSYII synchrotron source with a photon energy of 300 eV ($\lambda = 4.1$ nm). At these particular settings, the beamline delivers not only the selected photon energy, but also a sizable amount of radiation at twice the photon energy [64]. Due to this, the diffraction images not only contain the first and third grating diffraction order of 300 eV, but also the third diffraction order of 600 eV (see annotations in Fig. 5.3b). The sample and apertures are 30(5) cm downstream of the beamline focus. This ensures a large x-ray spot with a lateral dimension of about 3600 µm × 700 µm, the spatial fluence distribution of which varies chiefly along the longer, horizontal axis [64].

The gratings are FIB-milled into a 50 nm thick, thermally evaporated Au layer. The gold gives good absorption contrast, even at shorter photon wavelengths, but forms residual grains of several 10 nm size during the milling process. The speckle diffraction from these grains is visible in all recorded images as an additional scattering signal. This makes evaporated Au an inferior choice for the grating material, as compared to e.g. Si_3N_4 or – especially for higher photon energies – Ta and single-crystalline gold [65].

The image series in Fig. 5.3 shows a fully illuminated 35 µm × 35 µm grating and the same grating with a square 12 µm aperture at various positions in front of it. It is obvious that the grating accurately maps the incident photon distribution to the detector plane. The diffracted map unambiguously reveals the aperture's shape and position with respect to the grating sample. Likewise, it is immediately obvious when the sample membrane clips the incident beam, as is the case in Fig. 5.3c. This makes an accurate alignment of a membrane carrying sample to the photon beam trivial for most experiments. The faint horizontal and vertical streaks that emanate from the corners of the fluence map are characteristic for the tightly confined, rectangular illumination of a hyperbolic grating, as discussed in Section 4.2.2.

5.2.3. Large area segmented gratings

During the grating manufacturing, the patterning area of the FIB pattern generator is, for the given resolution requirements, limited to about 40 µm × 40 µm. Larger gratings are milled in segments, i.e. by partitioning the whole structure into 35 µm × 35 µm tiles and sequential milling. The gratings in this section are prepared in this fashion with a spatial extent of 140 µm × 140 µm. This area is large enough to reveal the internal structure of the out-of-focus beam 30(5) cm behind the focus. Here, the horizontal extent of the beam is 3.6(6) mm [64]. Along this direction, the beam has a pronounced internal structure, which is visible in the spatial fluence distribution imaged in Fig. 5.4a. For this large, 140 µm × 140 µm grating, the geometric distortion discussed in Section 4.3.2 becomes noticeable.

In addition the the internal beam structure, the boundaries of the sequentially milled

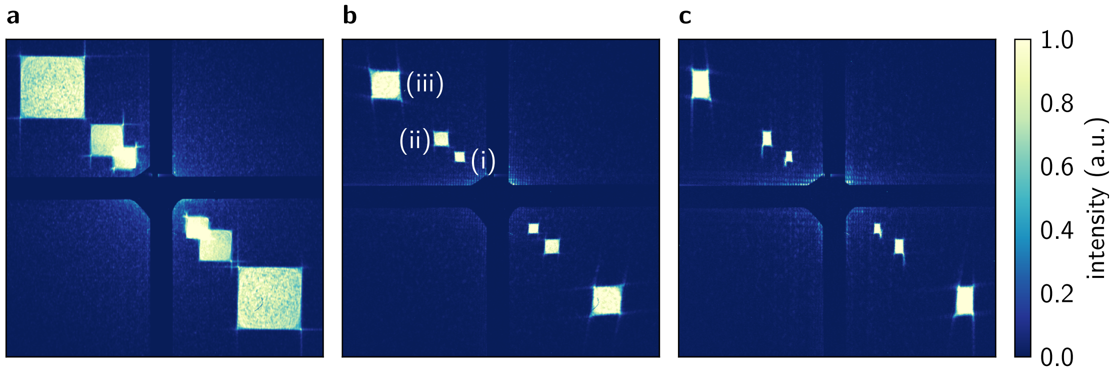

Figure 5.3.: Fluence maps of aperture-defined illuminations. The diffraction spots correspond to different grating diffraction orders (m) and photon energies (E): (i) $m = 1$, $E = 300\,\mathrm{eV}$, (ii) $m = 3$, $E = 600\,\mathrm{eV}$ and (iii) $m = 3$, $E = 300\,\mathrm{eV}$. **a)** Fully illuminated grating. **b)** Illumination through a square, $12\,\mu\mathrm{m} \times 12\,\mu\mathrm{m}$ aperture. **c)** Same aperture as in (b), positioned at the edge of the grating area. Here, the overlap between sample membrane and aperture is reduced to a rectangular area of $5(1)\,\mu\mathrm{m} \times 10\,\mu\mathrm{m}$.

grating tiles are discernible as horizontal and vertical lines in the diffracted intensity maps. SEM images reveal a change in the image contrast of the corresponding grating regions (Fig. 5.4b). This indicates that patterning artifacts, such as redeposition and proximity effects, locally reduce the topographic grating amplitude and thereby the grating efficiency at the tile junctions. A spatial stitching error, i.e. gaps between (or overlaps of) neighboring grating tiles could additionally lead to a phase shift of the grating at the tile junction. This would also manifest in visible tile boundaries in the diffracted fluence maps. However, careful inspection of the SEM image in Fig. 5.4b shows that this is not the case and the boundaries observed are due to an amplitude modulation at the tile junctions. Optimized patterning strategies – as employed for zone-plate manufacturing – are able to overcome these limitations [66, 67].

5.2.4. Interleaved gratings with spatially allocatable diffraction

It is possible to obtain spatial fluence information by distributing a number of separate, distinguishable gratings (e.g. with varying orientation angles ϕ) over the sample. Since the diffraction of these gratings does not overlap when designed suitably, their individual intensities are proportional to the integral illumination of the corresponding grating. With the known positions of the gratings on the sample, this constitutes a rough map of the spatial fluence distribution. The resolution of this map depends on the size and density of the gratings on the sample. The intensities need to be extracted from the diffraction image and manually allocated their respective position, as demonstrated in Fig. 5.6b-c. The comparison with an aperture scan (Fig. 5.6d) validates the spatial fluence distribution obtained in this fashion. This concept is a direct precursor to the spatially resolving gratings derived in Section 4.1. It is a viable alternative for experiments where the contiguous fluence maps produced by a spatially resolving grating

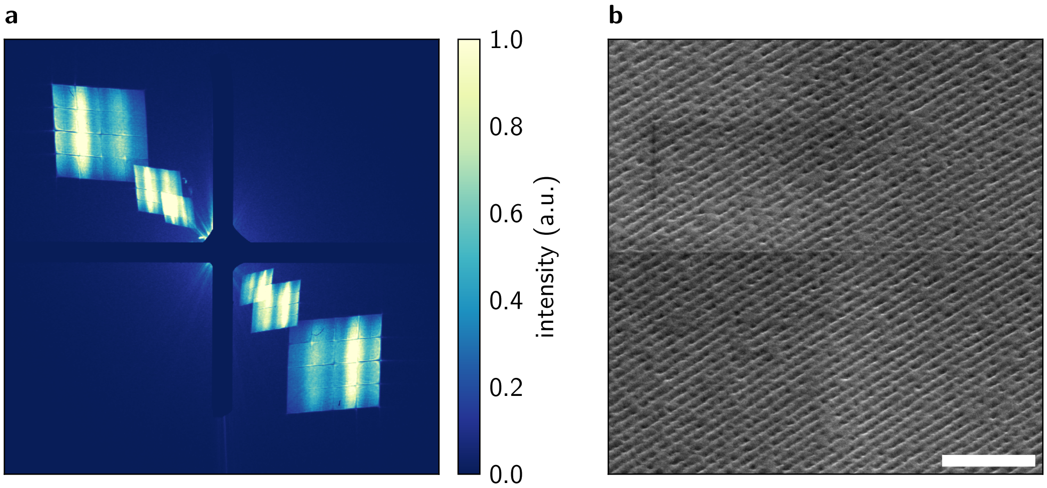

Figure 5.4.: Diffraction and SEM image of a large segmented grating. **a)** Diffraction pattern of a 140 µm × 140 µm (4 × 4 tiles of 35 µm each × 35 µm each) tiled grating at 300 eV and, simultaneously, 600 eV. The inner- and outermost fluence maps are, respectively, the first and third grating diffraction orders of 300 eV. The overlapping fluence map between those two is the third diffraction order of 600 eV (see also Fig. 5.3). The intensity variation represents the actual illumination on the sample, as created by the beamline optics. **b)** SEM image of a grating structure milled in gold. In the center of the image, four adjacent milling areas meet. Here, the boundary of the milling fields is more pronounced in the horizontal direction. Such matching errors leads to the noticeable tile outlines in the diffracted intensity maps. Scale bar is 1 µm.

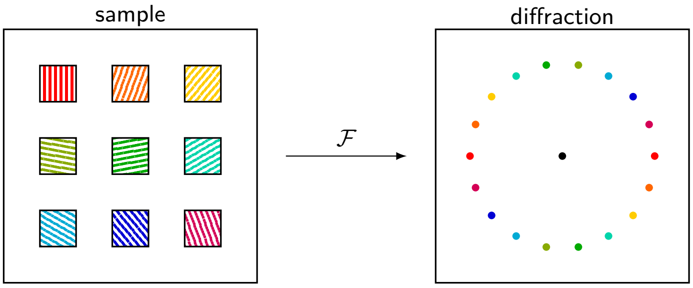

Figure 5.5.: Sketch of a fluence mapping experiment with distinguishable gratings. Illustration of a sample with separate gratings of uniform period and variable orientation (left). Different colors denote different orientation angles. Schematic diffraction pattern (right). Same colors denote corresponding gratings and diffraction.

monitor would overlap with the scattering signal of the sample under study.

5.3. In-situ fluence monitoring of FEL pulses

Fig. 5.7a shows the spatial fluence distribution of a single FEL pulse at the DiProI end-station of FERMI, measured by a grating monitor. The scattering signal directly provides relative fluence information. In this particular case, the fluence map is designed to cover an area of about 2 mm × 2 mm on the detector, or 0.5 % of the total available detector area. On the sample, the grating has a size of 35 µm × 35 µm, corresponding to a magnification factor of 58. The map reveals a complex focal spot with a bright central area and several side lobes of considerable intensity. This is in very good agreement with the independently obtained data for a different single-shot via a wave-front sensor measurement, shown in Fig. 5.7b. Small deviations from the actual photon distribution – as measured by the wave-front sensor – find their origin chiefly in the non-negligible spatial extent of the sample and the fact that the experimental geometry does not fully satisfy the condition for Fraunhofer diffraction. †

The far-field approximation is valid when the sample – detector distance z satisfies [33]

$$z > \frac{2D^2}{\lambda}\,. \tag{5.1}$$

Here, D is the aperture size and λ the photon wavelength. Given our experimental situation, with D being the grating's extent of 35 µm and $\lambda = 20.4\,\mathrm{nm}$, z needs to be larger than 120 mm. However, due to space constraints, the actual distance from sample to detector in this case is only 50 mm and deviations from the simulated Fraunhofer diffraction, as discussed in Section 4.3.1, are to be expected.

The focal spot's detailed structure is lost in the multi-shot fluence maps, as can be seen in Fig. 5.7c. Examining a series of 40 single-shot fluence maps shows that the absolute position in the transverse direction to the optical axis varies from shot to shot, while the shape of the intensity within the focal spot does not change substantially. Hence, the smearing out of this internal structure is due to the shot-to-shot pointing instability commonly encountered at FEL sources. Such spatial jitter presents a major obstacle in the performance and interpretation of high-fluence, single-shot experiments, especially when inhomogeneous samples are investigated. Given this situation, it is obvious that the interpretation of fluence-dependent phenomena is prone to large systematic errors, if the fluence on the sample has to be inferred from measurements over many shots or even from the integral pulse energy, as discussed in Chapter 3.

Fig. 5.8 shows the difference between the center-of-mass positions in corresponding single- and multi-shot images. The resulting estimate of the shot-to-shot spatial jitter is 4 µm and 7 µm (FWHM, horizontal and vertical, respectively).

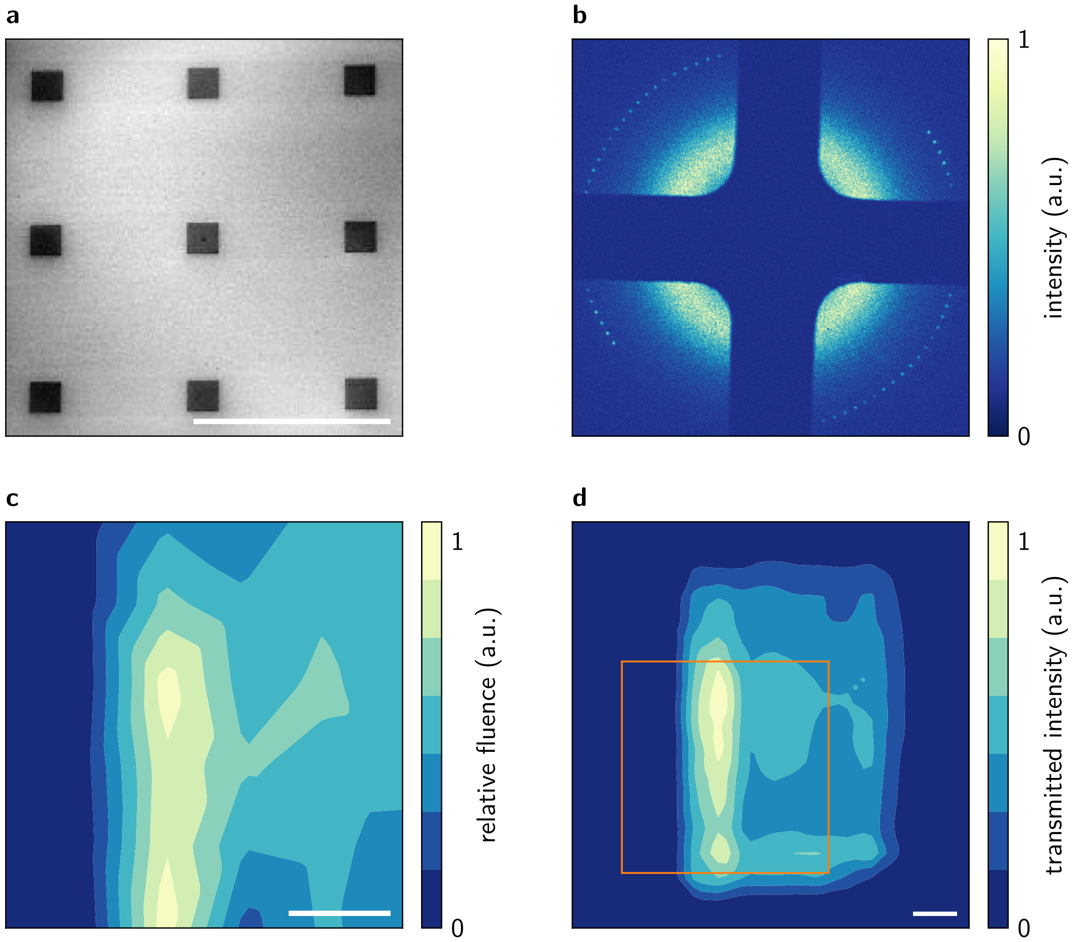

Figure 5.6.: Spatial fluence map from tiled gratings. **a)** SEM detail of a patterned Si_3N_4 membrane. Individual gratings (dark rectangular areas) cover an area of 7.5 µm × 7.5 µm in order to reduce milling time. The space between gratings is not patterned. The actual grating structure of lines and grooves is not discernible in this magnification. **b)** Scattering pattern of a 250 µm × 250 µm membrane with 6 × 6 segmented gratings. The bright ring near the center of the image is the XMCD scattering signal of the magnetic sample layer. Each pair of centro-symmetric spots on the outer ring corresponds to a different grating. **c)** False color fluence map of the sample illumination as measured by the segmented grating. Values are linearly interpolated between the 6 × 6 grating positions. **d)** Intensity map of the illumination, obtained by scanning a 30 µm × 30 µm square aperture over the beam in 20 µm steps and recording the transmitted intensity with a photodiode. The orange rectangle marks an area that corresponds to the mapped region in (c). All scale bars are 50 µm. #

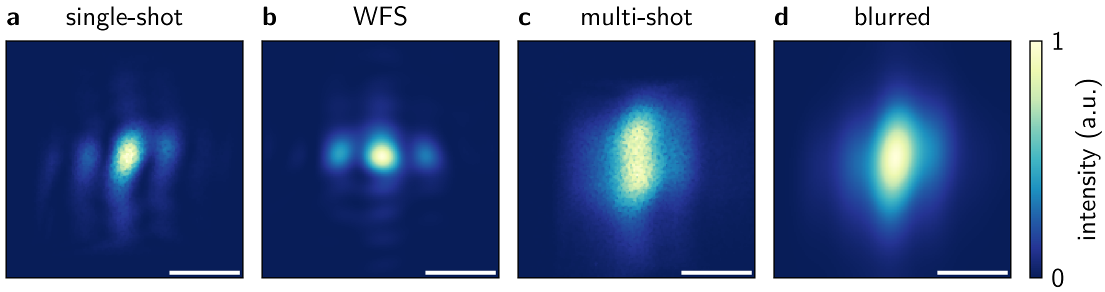

Figure 5.7.: Single- and multi-shot fluence distributions. **a)** Spatial fluence distribution of a destructive single-shot, measured by a curved grating sample. **b)** Single-shot wave-front sensor measurement of the photon distribution in the sample plane for a different FEL shot. **c)** Accumulated fluence distribution of 3000 attenuated shots on the same grating. **d)** Single-shot diffraction pattern convoluted with an asymmetric Gaussian kernel to simulate the multi-shot scattering pattern. Scale bars correspond to 10 µm. †

Alternatively, the spatial jitter can be inferred from only one set of single- and multi-shot images, by fitting a blurred version of the single-shot fluence map to the multi-shot map (Fig. 5.7d). The blurring is achieved by a Gaussian kernel with separate standard deviations in horizontal and vertical direction as fit parameters. For the whole series of 40 multi- and single-shot images, this procedure consistently yields spatial jitter values of 4.2(4) µm and 8.8(5) µm (FWHM) in horizontal and vertical direction, respectively. This is in good agreement with the position map in Fig. 5.8.

The amount of spatial jitter depends delicately on a plethora of parameters, from the radiation source to the refocusing optics. It is obvious, that – in addition to mapping the internal structure of the focus – the access to the spatial jitter of the focus on the sample on a single-shot basis is extremely valuable. This applies particularly to laterally inhomogeneous samples with spatially varying material composition, including particles sparsely dispersed on a membrane.†

We note that spectral jitter, i.e. a shot-to-shot change of the photon wavelength, has a slightly different influence on the measured fluence maps. Here, a centrosymmetric scaling of the diffraction pattern is to be expected due to the wavelength dependence of the scattering angles. This effect is negligible for seeded FELs such as FERMI, but might become noticeable at FELs employing the self-amplified spontaneous emission SASE scheme, e.g. at LCLS or FLASH.†

The spatial fluence distribution also changes substantially within a few millimeters along the beam propagation axis. This is due to the finite size of the optical elements which act as limiting apertures and introduce diffraction artifacts into the beam. The tailored grating integrated into the sample allows us to directly monitor this change for movement along the optical axis, as shown for selected positions along the beam propagation axis in Fig. 5.9a. Note that the images in Fig. 5.9 are from a separate experiment and thus are not expected to show the same spatial fluence distribution seen in Fig. 5.7. For all positions along the beam axis, we find excellent agreement of the

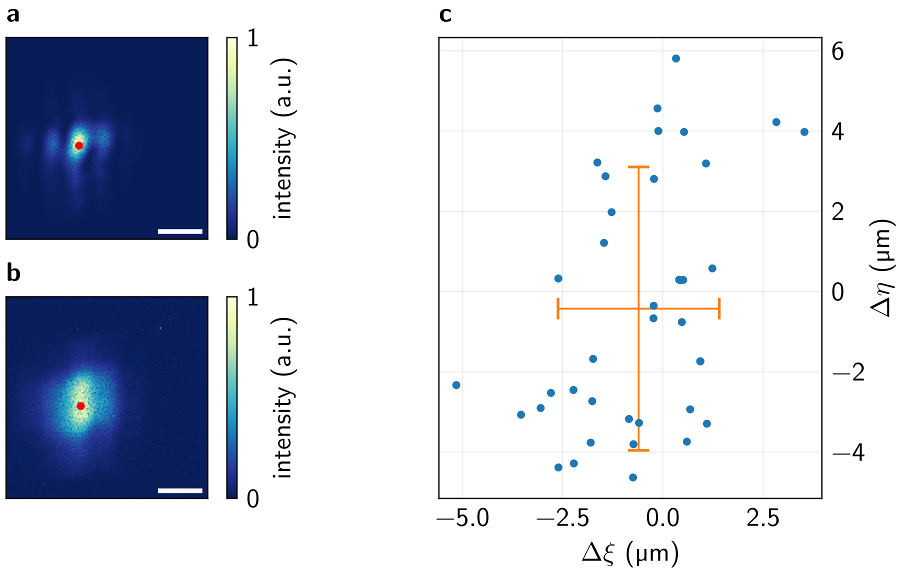

Figure 5.8.: Map of the spatial jitter. a-b) Example single- and multi-shot diffracted fluence maps. The red dot marks the calculated center-of-mass, i.e. the spot position. Scale bars are 10 µm. **c)** Two-dimensional map of the shift between single- and multi-shot spot position for all recorded data sets. $\Delta\xi$ and $\Delta\eta$ are the shifts in horizontal and vertical direction, respectively. The orange error bars mark the average position shift and its FWHM.

fluence distribution's fine structure between our grating measurement and the results calculated from wave-front sensor data (Fig. 5.9b).

We note that our *in-situ* fluence mapping approach can easily be used to track and optimize the sample position with respect to a focus both in the transverse direction as well as along the beam axis. The fact that the spatial fluence distribution on the sample varies substantially for changes in the sample position on the order of one millimeter along the optical axis, again illustrates the potential for uncertainty when fluences on the sample are estimated from integral pulse energy measurements.†

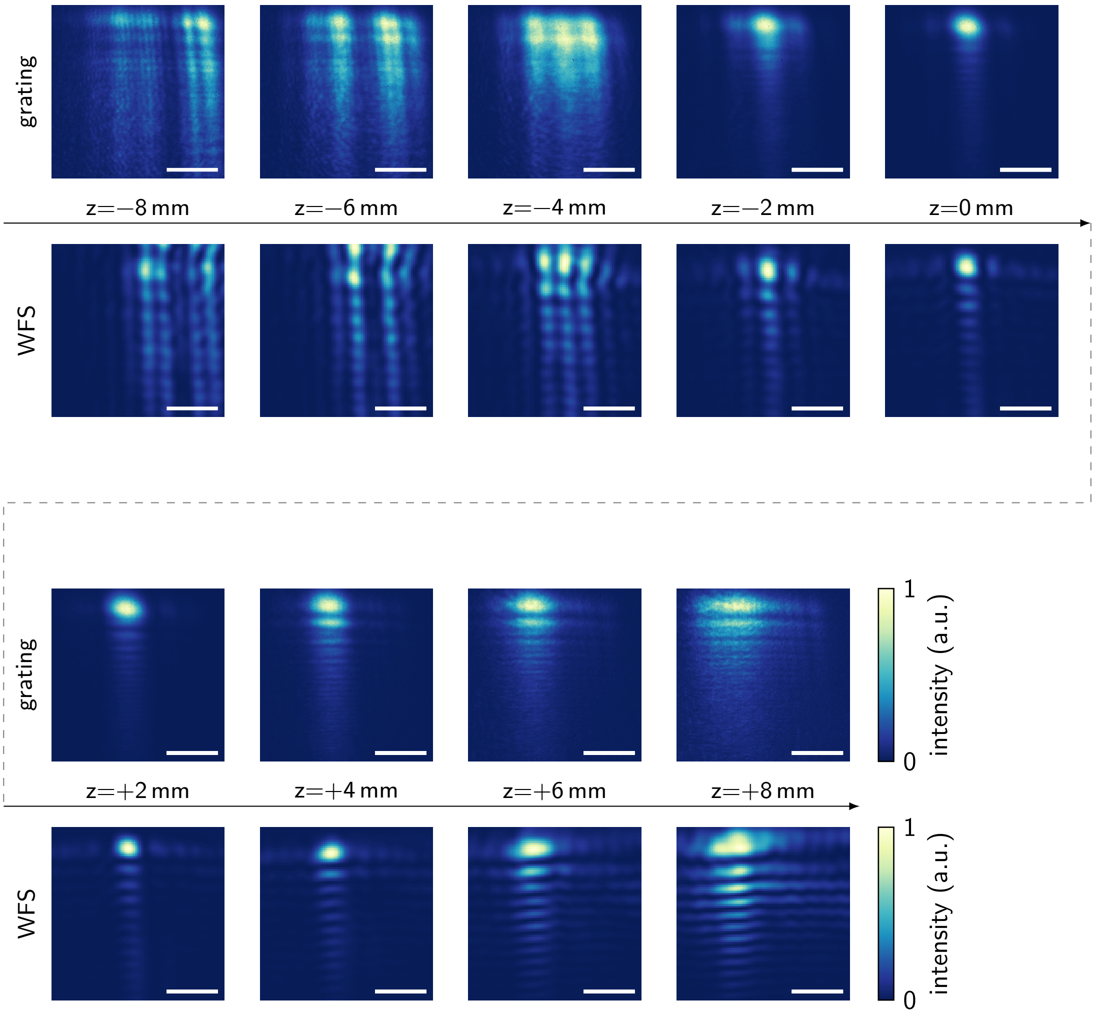

Figure 5.9.: Single-shot spatial fluence distributions along the beam propagation axis. Positive grating diffraction order and spatial fluence distribution calculated from wave-front sensor measurement along the beam propagation axis. The position z of the sample plane is given relative to the nominal focus position generated by refocusing the FEL beam using a KB optics. Scale bars correspond to 10 µm. [†]

6. Outlook and Summary

6.1. Applicability at higher photon energies

Moving towards shorter wavelengths and into the hard x-ray regime, the absorption contrast for most materials – and thereby the grating efficiency – diminishes. This necessitates higher aspect-ratios for the grating structures and thus a more challenging manufacturing process. Furthermore, the achievable focal spots of the FEL beam are considerably smaller, extending into the sub-100 nm region [20, 21]. Consequentially, smaller grating structures are necessary to satisfy Eq. (4.6) (if one wants to characterize such small foci). †

Due to their close relationship to the grating monitors, it seems reasonable to consider recent progresses in hard x-ray zone-plate manufacturing for the discussion of these issues. Zone-plates with 15 nm outer zone width have successfully been manufactured for hard x-ray radiation and are used in experiments with 9 keV photon energy [68]. With such manufacturing capabilities, it is feasible to directly transfer our concept to the hard x-ray regime and focal spot sizes on the order of 100 nm. Additionally, our concept does not require high diffraction efficiencies and aspect ratios can accordingly be smaller than for a zone-plate. This makes it possible to utilize even smaller structures, and achieve sub-100 nm resolution. However, the complex manufacturing process might – at the current technological state – prohibit the time- and cost-efficient fabrication of a large number of samples for destructive studies. The actual limit will of course depend on the specific experiment, including photon energy, sample size and thickness, available detector space and the experiment geometry. †

The low absorption of hard x-ray radiation in most of the conceivable grating materials is greatly beneficial when transparent beam monitors are considered. In such cases, our grating concept could provide permanent and reliable *in-situ* feedback of the beam position and its internal structure at critical beam-line positions, such as split-and-delay units [69, 70] or intermediate focus stages [21]. This is further encouraged by the fact that spatial constraints in the experimental setup apply to a much lesser degree since high-vacuum conditions are usually not required. Additionally, no computational treatment of the measured fluence distributions is necessary. This makes the concept suitable for live-monitoring, even at very high repetition rates. †

6.2. Summary

The first part of this thesis demonstrates the necessity of reliable estimates of the spatial fluence distribution on the actual sample. It discusses currently available methods and identifies their respective limitations when it comes to *in-situ* fluence monitoring. In order to supplement the existing methods, a novel concept based upon monolithically integrated gratings on the sample membrane is developed. The design formula for such gratings is derived from simple geometric considerations. The gratings form off-axis segments of either hyperbolic, or Fresnel zone plates. Theoretical calculations and numerical simulations explore the mapping capabilities and aberrations of these structures. In addition, the capabilities and usefulness of this concept has been demonstrated in FEL and synchrotron experiments at photon energies from 60 eV to 600 eV. The experimentally measured spatial fluence distributions are in excellent agreement with *a priori* known illumination patterns or independently obtained WFS data.

This fluence-mapping approach is a unique tool for true *in-situ*, single-shot-capable monitoring of the fine structure of the sample illumination in transmission-type scattering experiments. It is the only approach that allows for a simultaneous, non-invasive, mapping of the fluence distribution on the sample together with a scattering signal of interest. The approach provides an instantaneous online signal, which can be interpreted without any further computation, and can thus be used as instant feedback to align the upstream optical system. In the study of fluence-dependent phenomena, it provides crucial information for the correct interpretation of the data. The position and magnification of the photon-fluence map on the detector is, within the discussed constraints and the limits of the particular manufacturing process, freely selectable. Furthermore, the derivation of the grating formula can easily be adapted for diffraction experiments in reflection geometry. This makes the concept compatible with a large variety of experiments and samples. At the time of writing, this approach has already become a valuable and routinely used tool for alignment and optimization of the beam profile and sample position at the DiProI end-station of the FERMI FEL. †

Part III.

Fluence-dependent diffraction

7. XMCD diffraction from magnetic domains

The second part of this thesis discusses the fluence-dependence of XMCD diffraction from magnetic thin-film samples. In the samples used, the magnetization is perpendicular to the sample plane, and forms a worm-like domain pattern of alternating magnetization directions. The domains are unaligned (i.e. their orientation within the 2d sample plane is isotropic) and they exhibit a uniform width (see Section 2.3). Previous experiments on such samples have shown a quenching of up to 95 % of the XMCD-based scattering signal with increasing XUV [29] or soft x-ray [28] fluences. At soft x-ray wavelengths, different fluence dependent studies between $1\,\mathrm{mJ/cm^2}$ and $300\,\mathrm{mJ/cm^2}$ suggest different explanations – ultra-fast demagnetization [28] and stimulated emission [30] – for the dependence observed. The experiment reported in the XUV regime covers only the already strongly quenched regime at $5000\,\mathrm{mJ/cm^2}$ [29]. Moreover, it suggests a third explanations, i.e. an energy shift of the Co $\mathrm{M}_{2,3}$ absorption resonance.

The goal of the experiment described here is to map the complete fluence dependence of the XMCD diffraction cross-section at the Co $\mathrm{M}_{2,3}$ resonance, from a few $10\,\mathrm{mJ/cm^2}$ to $10\,000\,\mathrm{mJ/cm^2}$. This will potentially reveal which of the proposed models is most suitable to explain the quenching of XMCD-based scattering at XUV wavelenghts.

The results in this chapter cover two separate experiments in two different beamtimes[1] at the DiProI end-station of the FERMI FEL that are both conducted in the same manner and on the same set of samples. There are, however, inevitable differences in the FEL parameters, including for example the spot size and its internal structure. This is especially important since the samples in these experiments use only *integral* fluence monitors. The spatially resolving grating design described in the previous chapters was developed at a later time. Since beamtime at an FEL source is mandatory in order to reach the necessary fluences, the experiment could not be repeated with the spatially resolving fluence monitors. This has several significant consequences. While conducting the experiment, the spatial fluence distribution in the sample plane is an important parameter that, for example, governs the sample alignment. This includes the position along the optical axis relative to the focal position and thus the maximum fluence attainable. In the analysis of the data recorded, accurate fluence information is critical in order to extract the fluence dependence. Here, it is important to note that the experiment is destructive and a new sample is aligned for every data point. Given the finite size of the sample membranes and the complex internal structure of the focused FEL beam at the DiProI end-station (see Section 5.3), the effective spatial

---

[1] beamtimes 26.02.2014 – 01.03.2014 and 21.04.2015 – 26.04.2015

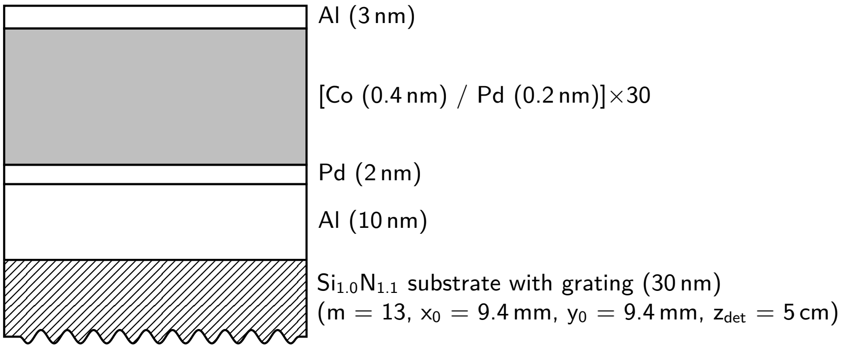
Al (3 nm)
[Co (0.4 nm) / Pd (0.2 nm)]×30
Pd (2 nm)
Al (10 nm)
$Si_{1.0}N_{1.1}$ substrate with grating (30 nm)
(m = 13, x_0 = 9.4 mm, y_0 = 9.4 mm, z_{det} = 5 cm)

Figure 7.1.: Schematic of the sample layer structure. The top Al layer prevents the oxidation of the magnetic layer. Individual layer thicknesses are to scale, except for the substrate.

fluence distribution is likely to differ from sample to sample. In the present case, the fluence information for individual membranes is obtained after the diffraction experiment from a combination of WFS, AFM and SEM measurements (Section 7.3). For future experiments using spatially resolving fluence monitors, this complex procedure is greatly simplified. Crucially, the spatial fluence distribution is then already available during the experiment.

7.1. Experiment description

The experiment discussed here is a diffraction experiment in transmission geometry, as described in Section 2.4. The samples are 25 mm × 25 mm Si chips with about 100 individual silicon-nitride windows (approximate composition $Si_{1.0}N_{1.1}$ [71]) of 30(5) µm × 30(5) µm size. The facet-sides of the 35(5) µm × 35(5) µm membranes bear FIB-milled hyperbolic grating monitors with parameters as noted in Fig. 7.1. The magnetic layer structure, also shown in Fig. 7.1, is deposited after the milling process by DC magnetron sputtering. This sequence ensures that the milling process does not damage the magnetic multi-layer via ion implantation (see Section 2.6).

The experiment itself follows a relative measurement scheme: Every measurement consists of a low-fluence characterization and a subsequent high-fluence single-shot. The low-fluence diffraction pattern establishes the diffraction cross-section for the magnetic domains and the grating monitor on the current sample at low fluence, i.e. within the regime of linear light–matter interaction. The high-fluence single-shot image follows immediately after.

For every measurement, a new sample membrane is aligned at low photon fluence. In these particular experiments, a reliable alignment – which necessitates direct optical control – was only possible with the faceted side of the sample facing towards the FEL beam, as this is also the only direction from which the sample is visible. This orientation presents the $Si_{1.0}N_{1.1}$ membrane to the incident beam, instead of the magnetic multi-layer. The membrane and the Al and Pd layer combined absorb 45 % of the incident XUV photons [9].

Two Al solid-state filters of 200 nm and 800 nm thickness attenuate the beam during sample alignment and the low-fluence measurement. The characterization measurement consists of 300 attenuated FEL shots with an average shot energy of 0.094(21) µJ for the first, and 1.83(34) µJ during the second experiment, as measured by the GMD. Given their respective beam footprints on the sample, these correspond to a per-shot fluence of 25(3) mJ/cm^2, and 47(9) mJ/cm^2 on the sample (see discussion in Section 7.3.3). These characterization fluences are comparably high, given the fact that in their experiment at the Co $L_{2,3}$ absorption resonance, Wang *et al.* observe non-linear behavior already at 30 mJ/cm^2. The relatively high characterization fluence is a direct consequence of the uncertainty in the spatial fluence distribution estimated during the experiment.

For the subsequent single-shot, only the 200 nm Al-filter remains in the beam upstream of the sample in order to block the UV photons of the seed laser pulse. The natural shot-to-shot fluctuation of the FEL source already provides a random fluence variation of up to one order of magnitude. A gas absorber with variable pressure provides additional, adjustable attenuation for the high-fluence single shot.

7.2. Experimental Results

7.2.1. Diffraction image features and analysis

The experiments in this chapter record far-field diffraction images. They consist of a high-intensity center that corresponds to the undeflected beam and additional, centrosymmetric signal contributions. Given the sample – CCD distance of 5 cm and a photon wavelength of 20.4 nm, the maximum detectable momentum transfer at the edges of the detector is $\pm 41\,\mu\text{m}^{-1}$.

The gratings and the magnetic layer are designed such that all signal contributions fit on the limited detector area, but do not overlap with each other. Fig. 7.2a shows a typical single-shot diffraction image. It contains the diffraction signature of the magnetic domains and the artificially created grating structure. The bright spots on the image diagonal are due to the grating, while the 2d isotropic magnetic domains give rise to the ring-shaped feature. The cross-shaped dark area is the beam-stop, which protects the CCD detector from the undeflected beam and from light scattering off the membrane edges. Corresponding dark images are recorded for every measurement to correct for possible stray light.

When a high-powered FEL shot hits the sample, additional unwanted image features may occur. The absorbed energy ionizes a substantial fraction of the sample atoms within the few-femtosecond FEL pulse. The Coulomb-force between the ionized atoms results in a “Coulomb-explosion” that destroys the sample. This process generates fragments of the sample material as well as a plasma that emits light [6]. Both may impinge on the detector and generate a spurious signal that is not centro-symmetric and thus easily identified, as shown in Fig. 7.2b. In such cases, the corresponding detector regions need

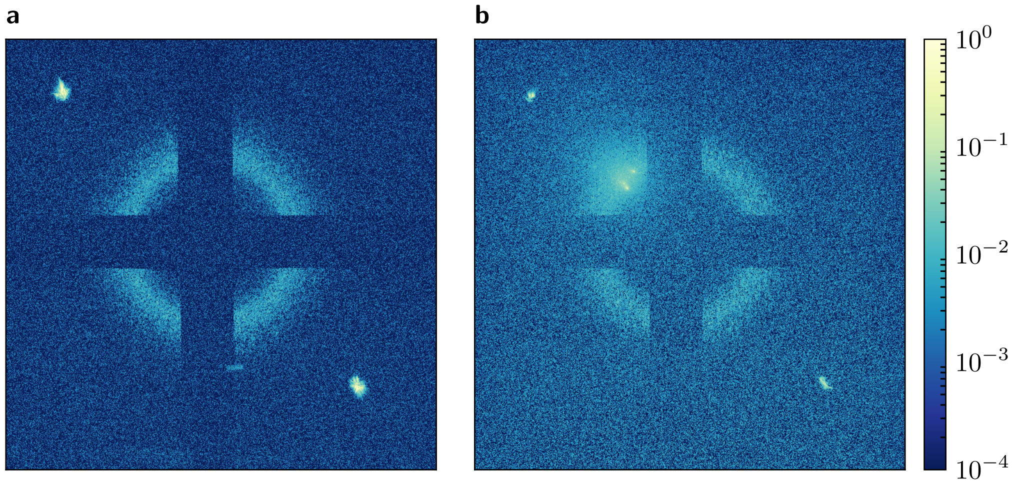

Figure 7.2.: Example single-shot diffraction images. **a)** Single-shot diffraction image of a 6.6 µJ FEL shot. The signal consists of the ring-shaped magnetic feature and the diffraction spots from an additional grating in the sample membrane. **b)** Single-shot diffraction image of a 4.1 µJ FEL shot on a different sample. In addition to the signals present in (a), the image exhibits non-centrosymmetric features that are due to the destruction of the sample membrane. Dark images have been subtracted in both cases. In both images, the maximum momentum transfer detectable at the edge of the detector is ±41 μm^{-1}.

to be excluded manually from the image evaluation.

Since the beamstop blocks the directly transmitted (i.e. $q = 0$) beam, the image center needs to be calculated from the center-of-mass positions of the two centrosymmetric grating diffraction spots. Accurately centering the images allows for an automatic positioning of the region of interest (ROI) for the grating- and magnetic domain diffraction (white and orange markers in Fig. 7.3a). Integrating the detected intensity in these regions yields the grating- and domain diffraction signal (I_{gr} and I_{mag}, respectively).

The distance to the image center, i.e. the polar angle θ of the diffracted beam, is related to the spatial periodicity p of the diffracting structure (see Section 2.2):

$$\sin\theta = \frac{\lambda}{p} \tag{7.1}$$

Or, in terms of the in-plane momentum transfer Δq:

$$\begin{aligned} \Delta q &= \frac{2\pi \sin\theta}{\lambda} && (7.2) \\ &= \frac{2\pi}{p} && (7.3) \end{aligned}$$

Thus, azimuthal integration of the XMCD signal yields the intensity distribution with respect to the size of the diffracting structure, as shown in Fig. 7.3b. This directly gives

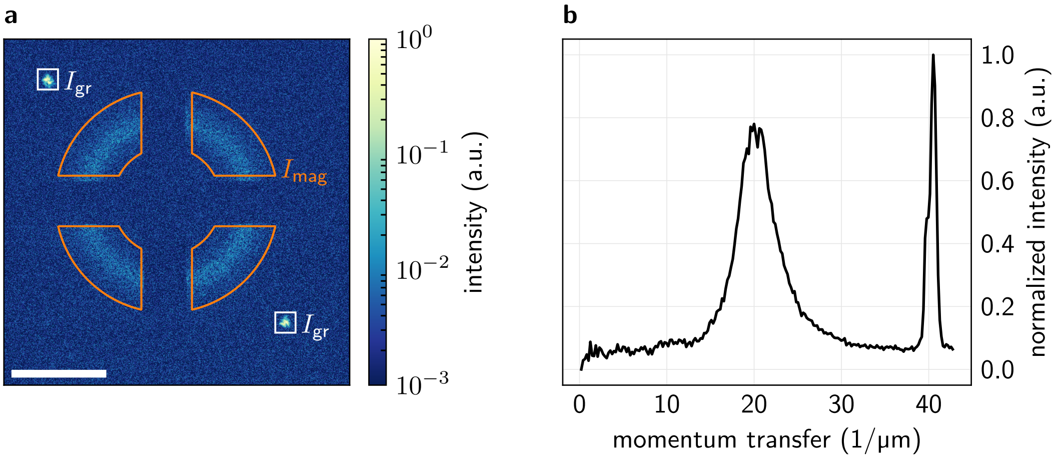

Figure 7.3.: Diffraction image evaluation. **a)** Single-shot diffraction image after background subtraction. The center-of-mass of the grating diffraction (white rectangles) accurately determines the image center. The integrated intensity in these areas yields I_{gr}. The ROI for the XMCD diffraction signal (orange lines) is defined relative to the image center. **b)** Relative intensity over momentum transfer, calculated from (a). The broad peak around 20 μm^{-1} corresponds to the ring-shaped XMCD diffraction and a domain size of 78 nm. The sharp feature at 40 μm^{-1} is due to the grating diffraction (approximately 40 nm half-pitch). The scale bar corresponds to a momentum transfer of 20 μm^{-1}

access to the size of the magnetic domains from the diffraction image.

For the purposes of this work, the diffraction cross-section of the magnetic domain lattice ($\sigma_{\mathrm{domains}}$) for a given FEL pulse duration is defined as the ratio of the detected intensity on the CCD (I_{mag}) and the pulse energy accepted by the sample (E_{sample}):

$$\sigma_{\mathrm{domains}} = \frac{I_{\mathrm{mag}}}{E_{\mathrm{sample}}} \tag{7.4}$$

However, these values are specific to the particular sample layer, e.g. its current magnetic state and history as well as seed- and cap-layer transmission. The experimental setup itself also affects the detected intensities, for example via the detector's efficiency and the size of the beamstop. Thus, the single-shot needs to be normalized to the low-fluence calibration measurement:

$$\delta_{\mathrm{domains}} = \frac{\sigma_{\mathrm{domains}}^{\mathrm{high}}}{\sigma_{\mathrm{domains}}^{\mathrm{low}}} \tag{7.5}$$

$\delta_{\mathrm{domains}}$ is a dimensionless parameter, that indicates the fluence-dependent change of the diffraction cross-section with respect to the (linear) low-fluence regime. Similarly, δ_{gr} is defined as the fluence dependence of the milled grating's diffraction cross-section:

$$\delta_{\mathrm{gr}} = \frac{\sigma_{\mathrm{gr}}^{\mathrm{high}}}{\sigma_{\mathrm{gr}}^{\mathrm{low}}} \tag{7.6}$$

It is important to note, that E_{sample} (i.e. the pulse energy accepted by the sample) is not generally equal to the integral FEL pulse energy as measured by the GMD (E_{GMD}). The latter cannot account for the finite acceptance of the sample membrane. In FEL-based experiments, the spatial size of the focused beam on the sample is often intentionally larger than the sample in order to ensure a homogeneous illumination. Additionally, the focused FEL beam may suffer from shot-to-shot positioning errors of several µm (see Section 5.3). Thus, the acceptance will also change between the low-fluence characterization and the high-fluence single-shot. However, the GMD-measured pulse energy is – for lack of an alternative – routinely used in FEL-based experiments for the purpose of estimating the pulse energy accepted by the sample.

The integral grating monitors on the samples in this work resolve this problem. Their diffraction signal I_{gr} is proportional to the pulse energy accepted by the sample, since the grating monitor covers the entire sample membrane:

$$E_{\mathrm{sample}} = cI_{\mathrm{gr}} \tag{7.7}$$

Inserted into Eq. (7.4) and Eq. (7.5), this yields

$$\delta_{\mathrm{xmcd}} = \frac{I_{\mathrm{domains}}^{\mathrm{high}} / I_{\mathrm{gr}}^{\mathrm{high}}}{I_{\mathrm{domains}}^{\mathrm{low}} / I_{\mathrm{gr}}^{\mathrm{low}}} \tag{7.8}$$

The value of δ_{xmcd} now only depends on the detected intensities in both CCD images. This makes it a very reliable quantity, as long as the detected intensities are above the detector's noise-level and below its saturation threshold, and provided that there is no fluence-dependence in the grating diffraction cross-section.

The FIB-milled topographic structure of the grating monitors modifies the sample's charge density distribution, which in turn gives rise to a diffraction signal via non-resonant absorption. It is to be expected, that the topographic structure does not change substantially within a single, sub-100 fs FEL pulse, due to the atomic bodies' inertia [12]. At such pulse lengths, the non-resonant diffraction signal of the grating monitors should thus have no fluence dependence.

Fig. 7.4 shows the measured grating diffraction cross-section $\delta_{\mathrm{grating}}$ over the GMD-measured single-shot pulse energies for both experiments. The absolute values of $\delta_{\mathrm{grating}}$ are above unity. This is due to the fact that the GMD of the DiProI end-station is upstream of the final solid-state filter and cannot account for its transmission. In the relative measurement scheme employed here, this filter is only used for the low-fluence characterization and removed for the subsequent high-fluence single-shot, which leads to the elevated $\delta_{\mathrm{grating}}$ values.

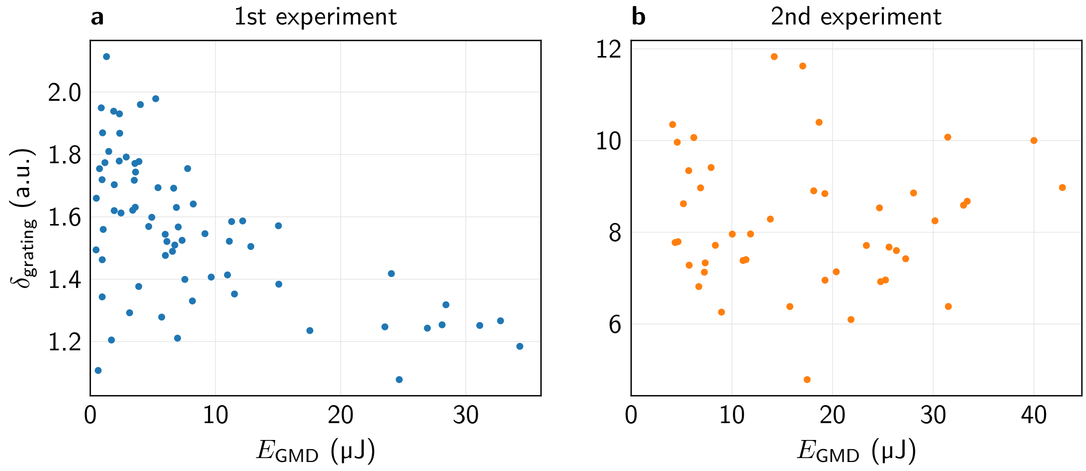

Figure 7.4.: FEL Shot-energy dependence of the grating diffraction cross-section. The measured diffraction cross-sections are above unity as the GMD cannot account for the transmission of the final solid-state absorber used during the characterization measurement. **a)** First Experiment. **b)** Second Experiment. The variation of the data is due to the pointing instability of the focused FEL beam.

The measured values vary quite strongly, with variations up to 20 % even within a small fluence range. As discussed above, this is due to spatial jitter of the FEL beam on the sample, which leads to different sample acceptances for the multi-shot characterization, and the high-fluence single-shot. The diffraction signal from the magnetic domains is equally affected by the acceptance. Thus, normalizing the magnetic diffraction signal to the grating diffraction corrects for the spatial jitter as well as for the additional filter transmission in the low-fluence measurement.

7.2.2. Non-linearity of the XMCD signal

Fig. 7.5 displays the measured δ_{xmcd} values over the integral shot energy as measured by the GMD (E_{GMD}). With the normalization to the grating diffraction (Eq. (7.8)), the actual δ_{xmcd} values lie, as expected [28–30], in the interval $[0, 1]$. Several observations are worth pointing out: (i) The XMCD diffraction cross-section exhibits a clear fluence-dependence over the entire range of shot energies. (ii) The single-shot pulse energies span more than two orders of magnitude. Taking the average characterization shot energies into account, the ratio of highest to lowest shot energies is more than three orders of magnitude. (iii) There is no lower threshold for the non-linearity. Even the lowest single-shot pulse energies of 0.5 µJ result in a 20 % reduction of the XMCD diffraction cross-section.

The data of both experiments exhibits this general trend. However, the actual δ_{xmcd} values for equal shot energies do not match up. This is due to the fact that the spatial fluence distribution differs significantly from one experiment to the other. In principle, this difference may manifest itself in two ways: (i) The fluence on the sample (per µJ shot

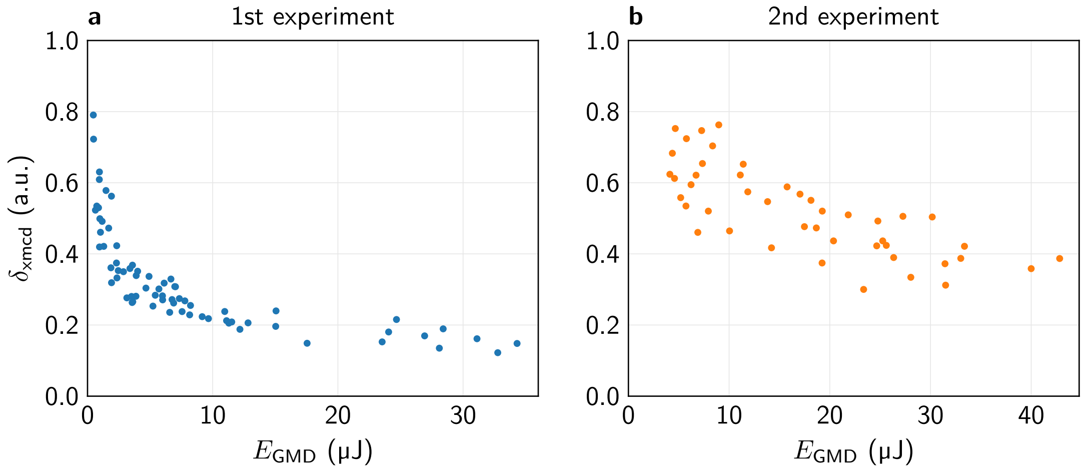

Figure 7.5.: Shot-energy dependence of the XMCD diffraction cross-section. a) First experiment. **b)** Second experiment. The different values of the relative diffraction cross-section (δ_{xmcd}) for equal shot energies between both experiments are due to decidedly distinct spatial fluence distributions.

energy in the FEL beam as measured by the GMD) in the second experiment is higher. In this case, the characterization measurement might already be in the non-linear regime. Since the single-shot diffraction cross-section is always relative to the characterization, this would necessitate a correction of the δ_{xmcd} values in the second experiment towards lower values. Or (ii), the effective fluence is lower in the second experiment. In a plot versus the spatial fluence, this would move all data points to the left. A combination of both cases is also feasible, since the characterization shot energies differ between the first and second experiment (0.1 µJ and 1.8 µJ, respectively). Thus, the single-shot fluences in the second experiment might be lower due to weaker focusing, while the characterization fluence is simultaneously higher due to increased shot energies. This demonstrates how crucially important reliable knowledge of the spatial fluence distribution on the sample is. The spatially resolving fluence monitors developed in the first part of this thesis could provide this information already during the experiment. In the present case, additional steps – as detailed in the next chapter – are necessary to obtain the spatial fluence distribution before a thorough understanding of this data set is possible. For the same reason, Fig. 7.5 does not give a break-down of the other experimental parameters, i.e. the FEL pulse length and size of the magnetic domains.

7.3. Spatial fluence distribution in the sample plane

The gratings in this particular experiment are intended as *integral* intensity reference, as the final – spatially resolving – grating design was developed after this experiment. They are based upon an empirically found formula [1], which can alternatively be expressed by the grating formula derived in Section 4.1. In terms of the latter, the gratings in this experiment are of the hyperbolic type with parameters $m = 13$, $z_{\text{det}} = 5\,\text{cm}$,

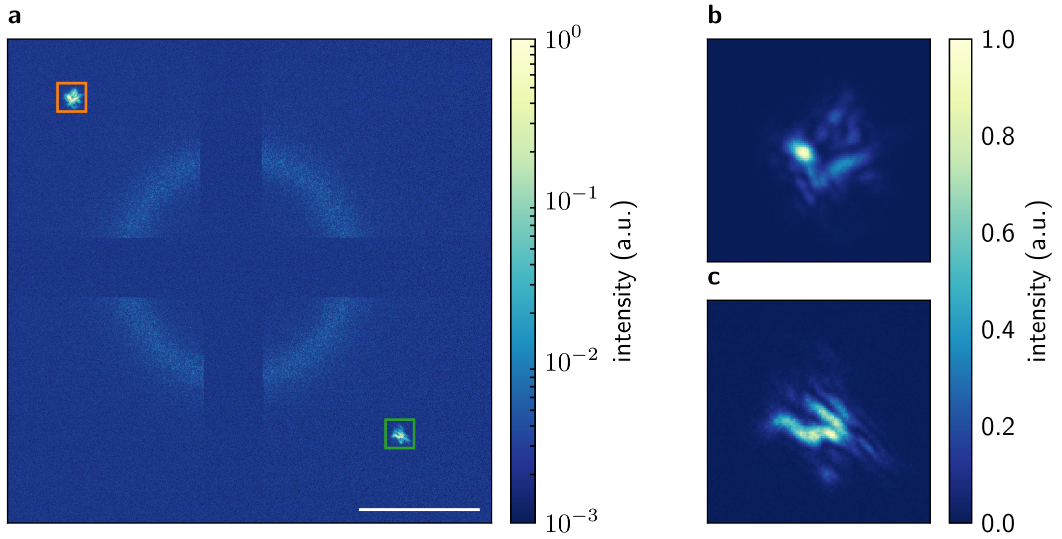

Figure 7.6.: Distorted spatial fluence map in the diffraction images. **a)** Single-shot diffraction image with a shot energy of 15 µJ. The scale bar corresponds to 20 µm^{-1} **b-c)** Details of the positive and negative grating diffraction orders. Orange and green frames mark the corresponding areas in (a). The two diffraction orders are not centrosymmetric since the experiment violates the far-field condition (Eq. (4.22)), and the grating parameters shift the image plane ±1.9 mm away from the sample plane (see Section 4.2.3).

$x_0 = y_0 = 9.5\,\mathrm{mm}$, sample size of $35\,\mu\mathrm{m} \times 35\,\mu\mathrm{m}$ and photon wavelength $\lambda = 20.4\,\mathrm{nm}$. These parameters violate two of the design principles for spatially resolving fluence monitors, derived in the first part of this thesis: (i) The detector distance is too small to satisfy the far-field condition (Eq. (4.22)) for the given sample size, which demands that $z_{\mathrm{det}} \geq 12\,\mathrm{cm}$. This results in severely distorted fluence maps, as shown in Fig. 7.6. (ii) The object planes mapped are $\pm z_{\mathrm{det}}/(2m) = \pm 1.9\,\mathrm{mm}$ away from the sample plane (positive and negative diffraction order, respectively; see Section 4.2.3). Thus, the gratings are not able to spatially resolve the fluence distribution on the sample. As a consequence, the experiment relies on rather large focal spots of $30\,\mu\mathrm{m} \times 30\,\mu\mathrm{m}$ and $100\,\mu\mathrm{m} \times 100\,\mu\mathrm{m}$ in the first and second experiment, respectively. This ensures a more uniform fluence distribution at the expense of peak fluence and a reduced sample acceptance as the finite membrane clips the FEL beam.

During the experiment, only rough aperture scans using an open, $30\,\mu\mathrm{m} \times 30\,\mu\mathrm{m}$ membrane were available to optimize the sample illumination (not shown). The large scanning aperture can only detect the beam footprint with this resolution and thus obfuscates local intensity maxima. This causes a significant uncertainty in the estimate of the spatial fluence distribution. In fluence-dependent experiments – such as discussed here – such an uncertainty may influence decisions regarding the experimental parameters, such as the characterization fluence, and thereby affect the course of the entire experiment. This underlines the fact that an *in-situ* measurement of the spatial fluence distribution on the actual sample is paramount – both for conducting the experiment as well as the interpretation of the recorded data.

The grating monitors employed could not provide spatially resolved fluence maps, but were able to measure the integral shot energy accepted by the sample. Consequentially, additional information about the footprint of the beam on the sample is required. This section discusses the steps that lead to an accurate estimate of the spatial fluence distribution in the sample plane. The final estimate combines AFM scans of damage craters in poly(methyl methacrylate) (PMMA) and the sample substrate with WFS measurements to obtain the fluence distribution in the sample plane. It then correlates the fluence distribution to SEM images of the shot sample membranes. This allows an assessment of the acceptance (i.e. the part of the incident beam that passes through the sample) of each individual membrane. With this information, it is possible to gauge the contribution of each fluence value to the measured diffraction signal. This approach yields a consistent definition of the nominal fluence for a given spatial fluence distribution and sample acceptance.

7.3.1. Obtaining the spatial fluence distribution

AFM scans of single-shot damage craters in the substrate material show, that i) the internal spot structure does not change substantially between shots in one experimental run (i.e. without realignment of the focusing optics); and ii) there are several “hot” spots, i.e. local intensity maxima (Fig. 7.7). However, it is not possible to directly extract the spatial fluence distribution from the damage craters since they suffer from melting and redeposition. Furthermore, the Si substrate has a comparably high ablation threshold of about $1\,\mathrm{J/cm^2}$ [54, 72]. Thus, the damage craters can only reveal the highest fluence maxima, but omit intermediate- and low-fluence structures in the FEL beam. Instead, a WFS measurement is used to obtain the actual spatial fluence distribution in the sample plane. This measurement is from a separate, unrelated experiment. However, the extrapolated fluence distribution matches the ablation imprints very well, as shown for the first experiment in Fig. 7.7. The good agreement is reasonable, since the experiment that furnishes the WFS measurement uses the same photon wavelength and beamline optics as the experiments discussed here.

7.3.2. Sample acceptance

In both experiments, the fluence distribution’s spatial extent is larger than the sample membranes. Thus, the surrounding substrate material clips the fluence distribution to the membrane size of about $30\,\mu\mathrm{m} \times 30\,\mu\mathrm{m}$. The actual section of the total fluence distribution of course depends on the sample alignment. Furthermore, Fig. 7.7d shows that the local fluence varies by up to $90\,\%$ over distances of less than $5\,\mu\mathrm{m}$. It is thus paramount to determine – for each single-shot – the exact sample acceptance, i.e. which part of the distribution actually interacts with the sample.

Since the grating monitors in this experiment cannot provide a spatially resolved fluence map, this information is obtained from the damage signature in the shot membranes via SEM imaging. For about $60\,\%$ of the membranes, the observed damage allows the

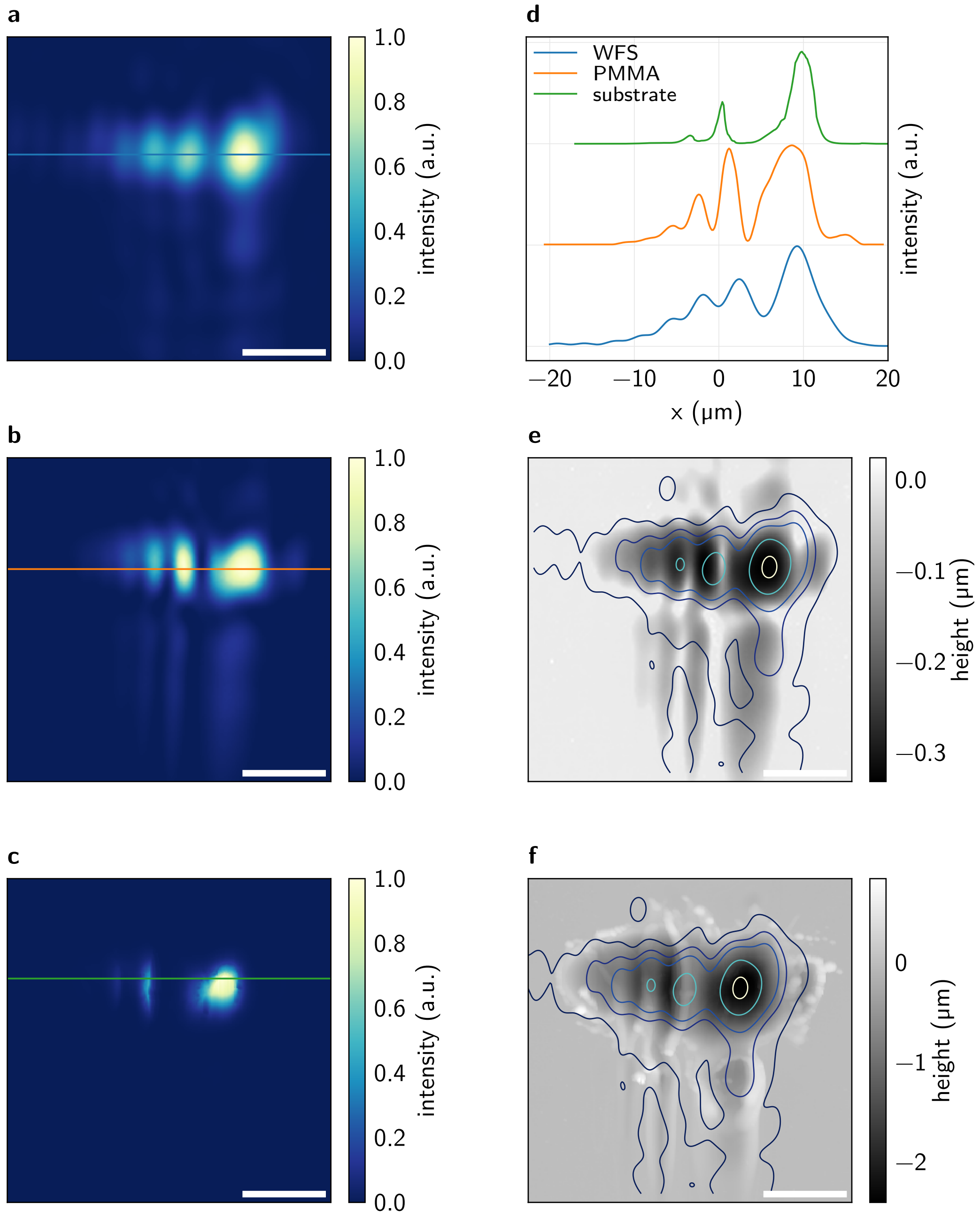

Figure 7.7.: Spatial fluence distribution during first experiment. Calculated from **a)** WFS measurement, **b)** ablation imprint in PMMA and **c)** single-shot damage crater in the sample substrate. **d)** Intensity along the marked lines in the three fluence distributions. **e)** – **f)** AFM images of the ablation imprints in PMMA and the sample substrate, respectively. The images are overlaid with lines of constant intensity of the WFS measurement. All scale bars are 10 µm.

alignment of the respective fluence distribution to the membrane, as demonstrated in Fig. 7.8. During the experiment, a consistent sample alignment strategy is maintained in order to minimize the influence of local intensity maxima. The SEM images show, that this is successful in 58 out of 74 cases (about 78 %). Fig. 7.8 shows examples of both, regular and misaligned, shots. The average integral acceptance is 69(13) % in the first experiment, and 19(3) % for the second.

7.3.3. Definition of the fluence axis

For every FEL shot, a wide range of local fluences interacts with different points of the sample. This makes it ambiguous to assign a single fluence value to a particular combination of fluence distribution, sample acceptance and integral shot energy. However, for the purpose of visualizing the results, as well as relating them to other experiments, such an assignment is necessary. The method described here gives consistent and meaningful results. Nevertheless, it is important to keep in mind that the magnetic diffraction signal in this experiment depends on the detailed fluence distribution.

Fig. 7.9a-b shows exemplary spatial fluence distributions and sample acceptances for both experiments. The fluence distributions consist of a large low-fluence population of narrow width, and a wider high-fluence part. This makes it impossible to use constant interval widths for an intensity histogram. Segmenting the fluence distribution with a global threshold into two (sub-)images circumvents this problem. The thresholding algorithm described by Li *et al.* is particularly suited for this case as it deals well with uneven widths and sizes of the sub-image distributions [73]. For a pixelated image $M = \{m_1, m_2, \ldots, m_i\}$, it iteratively modifies the threshold value t and calculates the measure

$$T_{\mathrm{Li}} = \frac{p - q}{\log p - \log q} \tag{7.9}$$

Here, p and q are the average intensities in the sub-images (with number of pixels N_1 and N_2, respectively) [74]:

$$p = \left(\sum_{m_i < t} m_i \right) / N_1 \tag{7.10}$$

$$q = \left(\sum_{m_i \geq t} m_i \right) / N_2 \tag{7.11}$$

After each iteration, $T_{\mathrm{Li}} \pm \epsilon$ becomes the new threshold value (depending on whether T_{Li} is above or below zero), until the difference between two iterations is smaller than ϵ. Typically, ϵ is set to about 0.1 % of the total value range in the image.

Fig. 7.9c-d shows the split histograms for both parts of the fluence distribution. In order to obtain a measure of how much each fluence value in the histogram contributes

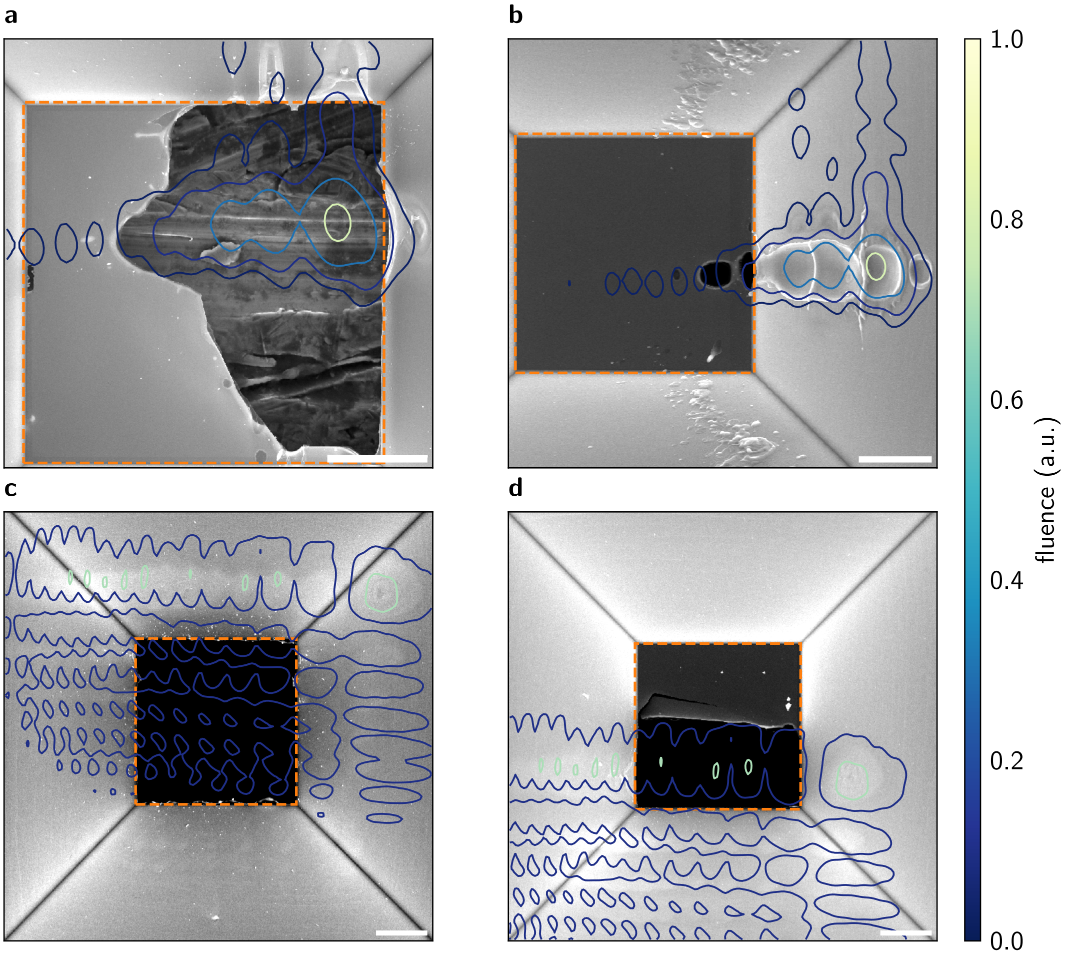

Figure 7.8.: Determining the sample acceptance from membrane damage. SEM images of shot membranes, overlaid with the associated spatial fluence distribution. The bright areas with diagonal boundaries are the etched Si facets of the sample membrane. These are practically opaque for the incident photons, due to the high absorption at the experiment's wavelength of 20.8 nm. The darker, rectangular area (dashed orange lines) in the center is the Si_3N_4 membrane. In most cases, we are able to position the spatial fluence distribution (colored lines) unambiguously on the SEM image. The effective fluence for a particular FEL shot is the overlapping region of the membrane marker and the aligned fluence distribution. Scale bars are 10 µm. **a)** Well-aligned shot (first experiment). **b)** Misaligned shot (first experiment). **c)** Well-aligned shot (second experiment). **d)** Misaligned shot (second experiment).

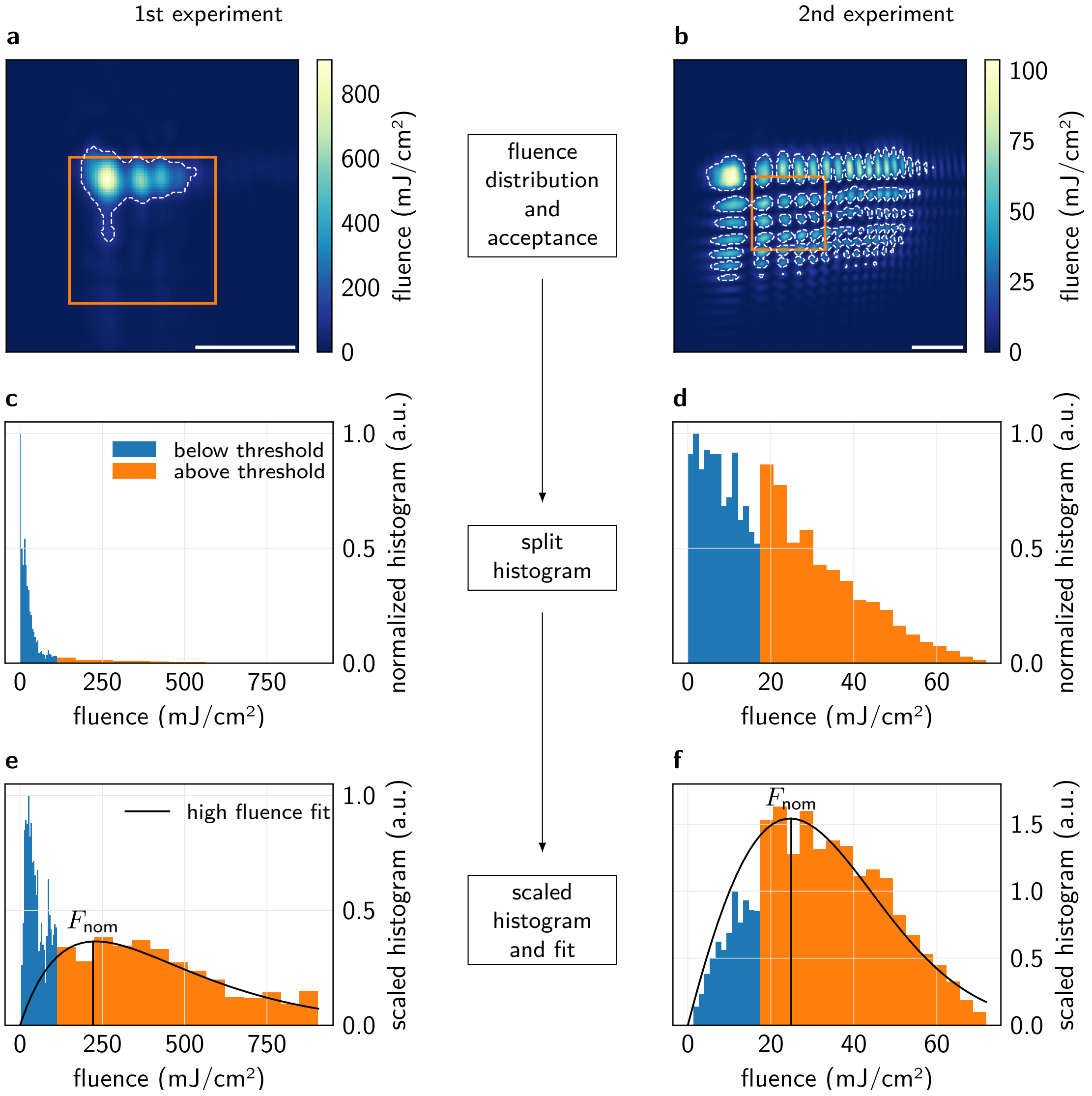

Figure 7.9.: Definition of the nominal fluence. Exemplary illustration of the fluence definition on the basis of the WFS-measured spatial fluence distributions for both experiments. **a, b)** WFS-measured fluence distribution during first and second experiment, respectively. The orange rectangles mark the accepted 30 μm × 30 μm part of the distribution in a typical sample alignment. The white dashed line marks the segmentation threshold that divides the image into a low- and high-fluence part. Image scale bars are 20 μm. **c, d)** Histograms of the frequency of fluence values in the accepted fluence maps. Especially during the first experiment, the high- and low-fluence parts differ considerably in variance and population size. This makes it impossible to calculate a usable histogram with uniform bin width. The image segmentation circumvents this problem. For a more uniform distribution, such as in the second experiment (d), the segmentation is not strictly necessary, but doesn't hinder the evaluation either. **e, f)** Low- and high-fluence histograms, scaled with their respective fluence values to reflect contribution to the overall detector signal. The solid black line is a fit of Eq. (7.12) to the high-fluence histogram. Its maximum marks the nominal fluence (F_{nom}) for the particular combination of fluence distribution and sample acceptance.

to the diffraction signal, the histogram counts are scaled linearly with their respective fluence values (Fig. 7.9e-f). This neglects non-linear effects that might increase or reduce the respective contribution to the overall signal level at higher fluences, but yields a consistent definition for the nominal fluence. For the non-Gaussian beams in this work, the scaled high-fluence histogram has a distinct maximum which marks the nominal fluence. Note that for an ideal Gaussian beam, this calculation yields a flat histogram. This signifies that, for Gaussian beam footprints, all fluences contribute equally to the overall signal. In contrast to that, the scaled histogram values for the non-Gaussian beams in this work follow a normal distribution, multiplied with the linear fluence scaling factor described above:

$$s(f) \propto f \cdot \exp\left(-f^2/\sigma^2\right) \tag{7.12}$$

Here, $s(f)$ are the scaled histogram values, f is the fluence and σ the width of the normal distribution. A least-square fit of this function to the scaled high-fluence histogram yields a robust value for the nominal fluence (Fig. 7.9e-f). Using only the high-fluence part is appropriate, since it typically is responsible for about 80 % of the measured signal (assuming a linear relationship between fluence and signal). This complete analysis is not available for all membranes, as some are completely destroyed, or the damage signature is otherwise ambiguous. For such cases, the most common spatial fluence distribution of the respective experiment is assumed.

Fig. 7.10 shows the nominal fluence values obtained in this fashion throughout both experiments, as well as their average values and standard deviations. Using these values, the fluence-dependent data from both experiments is now consistent with each other, as Fig. 7.11 shows. This plot reveals that the second experiment covers a much smaller fluence range, despite the higher integral FEL shot energies. The fluence information also significantly affects the theoretical modeling in the next chapter. This demonstrates the practicality of the outlined procedure as well as the critical importance of reliable fluence information for the interpretation of the experimental data. In this context, the elaborate determination of the actual fluence distribution accepted by each individual sample is a key aspect of this thesis. It sets it apart from other fluence-dependent studies and facilitates a thorough understanding of the fluence dependence measured.

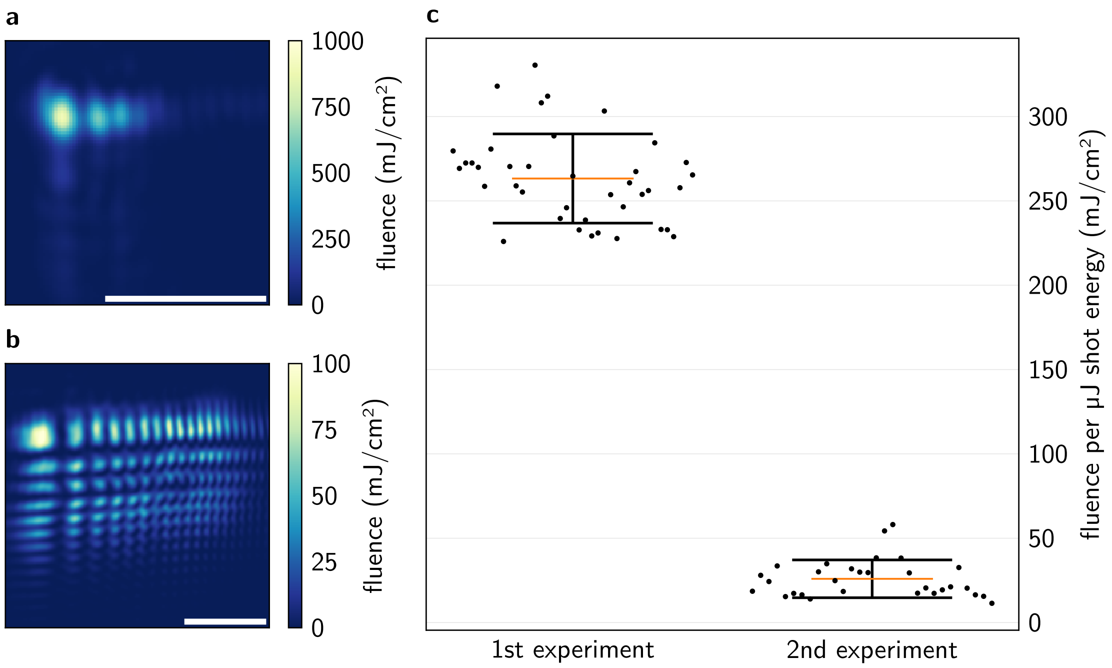

Figure 7.10.: Spatial fluence distributions and average fluence conversion factors. a, b) Spatial fluence distribution during the first and second experiment, respectively. The images show the whole distribution, as extrapolated from a WFS measurement. Both distributions are extrapolated from the same WFS measurement but belong to different positions up- and downstream of the beam focus. Fluence values in the false-color scale assume an integral shot energy of 1 µJ. Scale bars are 30 µm, which roughly corresponds to the size of the sample membranes. **c)** Summary of nominal fluence values (including sample acceptance) during both experiments. The points mark the nominal fluence values (per µJ shot energy) of all analyzed data sets. Orange lines denote the average value and the black error bars are the standard deviation of all nominal fluence values. It is obvious, that the focal spots in both experiments are very different. During the first experiment, the spot is focused tighter, which results in higher fluences for a given shot energy. However, the sample alignment is much more critical in this case, as evidenced by the greater spread of the data. In the second experiment, the fluence values are overall lower and vary less, as the distribution is much larger.

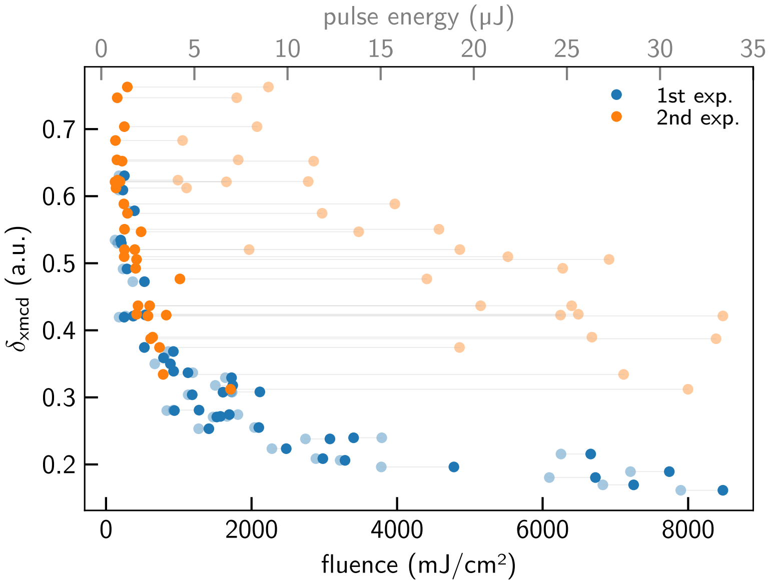

Figure 7.11.: Fluence ordering of the measured diffraction cross-sections. Comparison of the data in both experiments, plotted over the GMD-measured shot energy (top axis) and nominal fluence values (bottom axis). The detailed fluence analysis unifies the results of both experiments. It also changes the data ordering within the individual experiments. Less saturated points refer to the pulse energy axis (top). The horizontal gray lines connect corresponding points in both axes.

7.4. Phenomenological model of the non-linear XMCD diffraction cross-section

Fig. 7.12 shows the result of the previous chapter – the existence of a strong quenching of the XMCD diffraction cross-section that extends over the entire investigated FEL fluence range. In general, this cross-section is proportional to the absolute square of the sample magnetization [39, 75]. This chapter aims to explain the fluence dependence using a phenomenological model of XUV-induced ultra-fast demagnetization within the FEL pulse [28]. Given that the magnetization change occurs fast enough, a substantial fraction of the incident photons will encounter a significantly reduced magnetization level. These photons will then contribute less to the detected signal, effectively reducing the XMCD diffraction cross-section for the overall FEL shot.

Ultra-fast demagnetization after an optical excitation is an extensively studied field, both in fundamental research as well as in the context of optically induced switching which is of interest for potential technological applications in data storage and information processing [76]. For Co-based samples with an out-of-plane domain network this effect occurs on a 100 fs time-scale [24, 25, 77, 78]. This matches the pulse duration in the present experiments and can thus be considered a significant factor in explaining the observed fluence dependence.

The full mechanism that governs the demagnetization is still under debate [79–81].

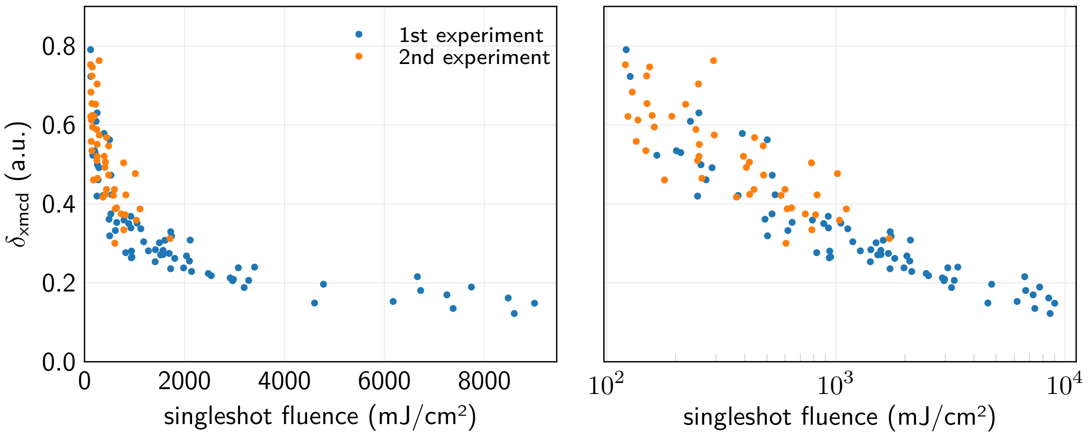

Figure 7.12.: Fluence dependence of the XMCD diffraction cross-section

Furthermore, experimental findings from different samples and techniques are not readily comparable. This is due to the fact that magnitude and characteristic time of the demagnetization depend on the detailed sample composition and the current magnetization state. The sample composition includes not only the individual layer materials and thicknesses, but also interface quality, additional seed- and cap-layers and impurities. In addition, the magnetization state depends on the microscopic domain structure and potential external fields. The sum of all these characteristics forms a highly specific system. Findings in such a particular system may be hard to generalize and measured parameters differ by factors of two to three between nominally comparable experiments. Table 7.1 at the end of this chapter summarizes the variance of reported parameters for ultra-fast demagnetization in different sample systems.

Most experiments on ultra-fast demagnetization induce the magnetization change via an optical or infrared pump pulse. In this thesis, the XUV FEL beam deposits energy in the sample. The model described here follows the work of Wang *et al.* in assuming that this initiates a demagnetization process in a similar way to optical pumping [28]. It is a numerical model based upon the Beer-Lambert law of absorption and a phenomenological description of ultra-fast demagnetization. It is discrete in the spatial and temporal domain.

7.4.1. Sample description

The sample modeled consists of $\delta z = 1\,\mathrm{nm}$ thick slices along the sample normal z. The single Co and Pd layers are not individually modeled, since they are only 0.4 nm and 0.2 nm thin (see Section 7.1). Given the lattice parameters of the respective single-crystals, this roughly corresponds to a single atomic layer of Co and half a layer of Pd [82]. It thus seem justified to model the multi-layer as a homogeneous film of an effective medium. This film has an average composition of 72 at.% Co and 28 at.% Pd.

Its absorption length l_{abs} at a photon energy of 60.0 eV ($\lambda = 20.4$ nm) is 10.6 nm [9]. This corresponds to an absorption of $a = 0.1$ per 1 nm slice with approximately 65 % of the total energy absorbed by the Co atoms. Fig. 7.13a shows the exponential transmission curve through the sample layer, given by

$$I(z) = I_{\text{tot}} \cdot \exp\left(-\frac{z}{l_{\text{abs}}}\right) . \tag{7.13}$$

7.4.2. FEL pulse propagation

The model assumes a Gaussian function for the temporal structure of the FEL pulse with total energy I_{tot}, as shown in Fig. 7.13b:

$$I(t) = \frac{I_{\text{tot}}}{\sigma_{\text{FEL}}\sqrt{2\pi}} \cdot \exp\left(-\frac{1}{2}\left(\frac{t}{\sigma_{\text{FEL}}}\right)^2\right) , \tag{7.14}$$

where σ_{FEL} is the FEL pulse length with a FWHM of $2\sqrt{2\ln 2}\sigma_{\text{FEL}}$.

In order to numerically model the temporal evolution of the sample and the diffraction signal, the pulse is partitioned into 10 fs slices. For each time- and spatial step, the model calculates the effectively absorbed fluence (Fig. 7.13c)

$$F_{\text{dep}}(z,t) = aA \cdot I(z,t) , \tag{7.15}$$

and the intensity of the XMCD diffraction signal

$$S(z,t) = I(z,t) \cdot M(z,t)^2 , \tag{7.16}$$

with the magnetization $M(z,t)$.

The magnetization quenching ΔM is assumed to be proportional to the absorbed fluence per unit time and volume until it reaches total demagnetization ($\Delta M = 1$) at F_{sat} [76].

$$\Delta M(z,t) = \begin{cases} F_{\text{dep}}(z,t)/F_{\text{sat}} & , F_{\text{dep}}(z,t) < F_{\text{sat}} \\ 1 & , F_{\text{dep}}(z,t) \geq F_{\text{sat}} \end{cases} \tag{7.17}$$

After excitation at t_0, the magnetization drops exponentially, as shown in Fig. 7.13d:

$$M(t) = \begin{cases} (1-\Delta M) + \Delta M \cdot \exp\left(-\frac{t-t_0}{\tau_{\text{m}}}\right) & , t \geq t_0 \\ 1 & , t < t_0 \end{cases} \tag{7.18}$$

Generally, the demagnetization time-constant depends on the magnetization quenching, and thus the fluence [24, 25, 76–78]. However, this dependence only extends to the low-fluence regime, i.e. below F_{sat}. The typical fluence values in the present experiment are several orders of magnitude larger. For simplicity, τ_{m} is thus assumed to be constant

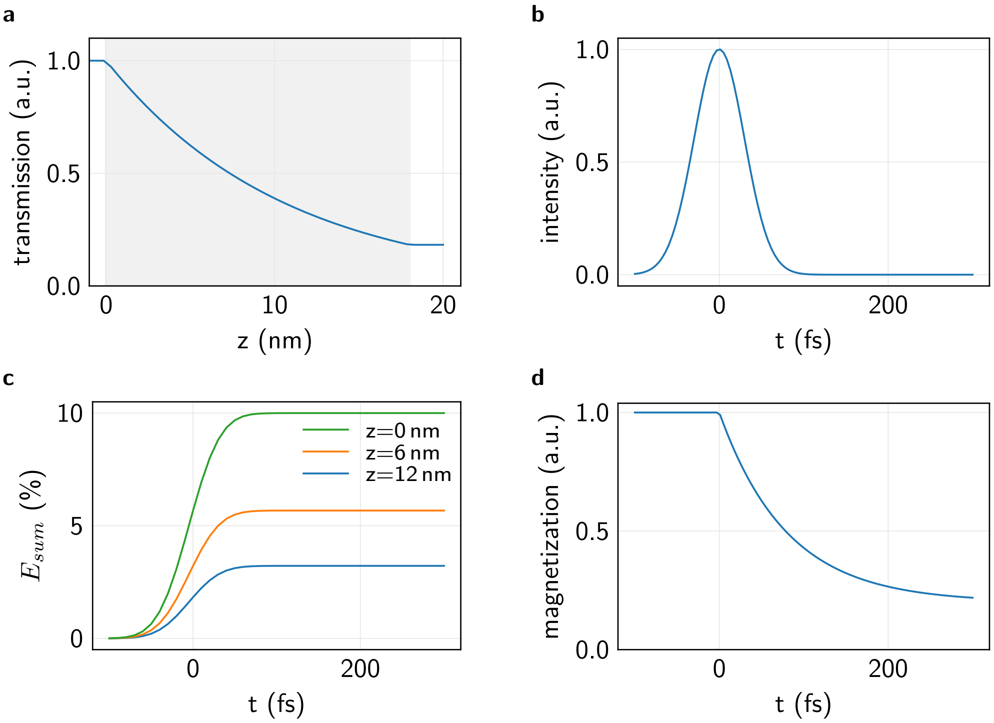

Figure 7.13.: Model components for ultrafast demagnetization during the FEL pulse **a)** Exponential absorption of the photon intensity along the sample normal. The shaded area marks the extent of the simulated sample, excluding seed- and cap-layer as well as the substrate. **b)** FEL pulse with Gaussian shape and 70 fs width (FWHM) **c)** Energy accumulation over time for three simulated sample slices of 1 nm thickness at different z. E_{sum} is given in percent of the total shot energy. **d)** Demagnetization curve with a time-constant $\tau_{\mathrm{m}} = 80$ fs and $\Delta M = 0.8$.

with respect to the photon fluence.

For every time step, an independent demagnetization curve (Eq. (7.18)) is calculated. All demagnetization curves up to the current time step superimpose without interaction, as shown for a single sample slice in Fig. 7.14.

Finally, the XMCD signal is integrated over the whole spatial and temporal simulation area. Fig. 7.15a shows the modeled spatial and temporal evolution of the magnetization. In Fig. 7.15b, it is obvious that the overlap of the effective sample magnetization and the FEL pulse modifies the amplitude of the diffraction signal. The actual magnitude of this modification depends on the various model parameters, which are discussed in the next section.

7.4.3. Influence of the model parameters

Fig. 7.16a-d demonstrates the influence of the three model parameters (τ_{fel}, τ_{m}, F_{sat}) on the overall fluence dependence. In the respective images, only one of the parameters varies, while the others are kept constant. It is evident, that the FEL pulse length,

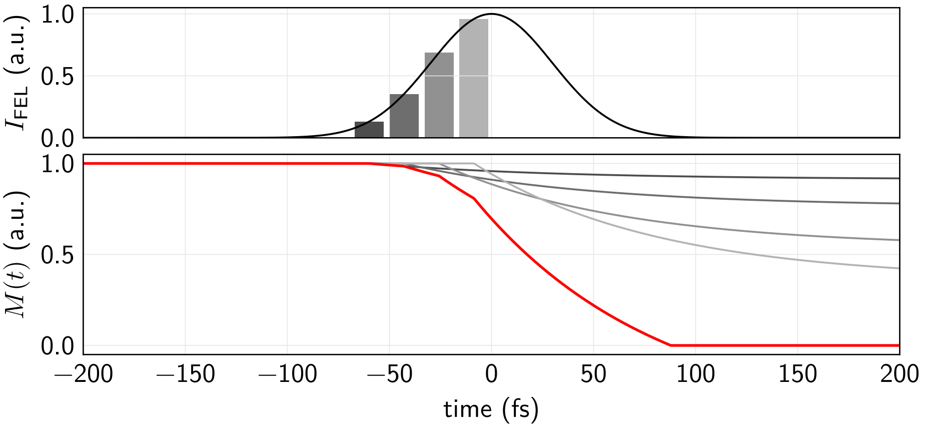

Figure 7.14.: Temporal superposition of demagnetization curves in a single sample slice. Top: The black line is the Gaussian FEL pulse and gray bars represent points in our temporally discrete model. For clarity, only selected time points are shown. At each time step, a demagnetization curve (gray lines, see Eq. (7.18)) starts with a ΔM that is proportional to the absorbed energy at that time (i.e. the bar height). All demagnetization curves share the same time constant τ_{m}. The thick red line is the sum of all demagnetization curves and represents the evolution of the total magnetization within the sample slice.

demagnetization time constant, and saturation fluence exert a similar influence within the explored parameter range. They all shift the curve along the fluence-axis, but do not modify the overall shape.

The relationship between pulse duration τ_{fel} and demagnetization time constant τ_{m} is easy to understand when considering Fig. 7.15b. Here, it is obvious that the XMCD signal is proportional to the overlap of the time-dependent magnetization curve squared and the FEL pulse. A slower demagnetization time thus compensates a longer FEL pulse length, and vice versa. Hence, it is the ratio of both parameters that is decisive, instead of their individual magnitudes.

In the destructive, high-fluence regime of our experiment, a relatively small fraction of the integral FEL shot energy is already sufficient to fully demagnetize the sample. The saturation fluence, F_{sat}, thus shifts the entire demagnetization curve along the temporal axis, since the Gaussian pulse shape has a comparably small slope in its outer regions. This modifies the overlap between the FEL pulse and the effective sample magnetization. The resulting effect on the fluence dependence is similar to modifying τ_{m} or τ_{fel}. Thus, changing one of these coupled parameters can always be compensated by an appropriate change of the other.

This implies, that fitting the model to experimental data may yield somewhat arbitrary results unless two of the parameters can be determined via independent measurements. On the other hand, the model predictions are quite universal, as it requires only the fact that the probing XUV beam is capable of initiating an ultrafast demagnetization of the sample. The assumption that this occurs approximately on the same time-scale and with saturation fluences that are comparable to optical pumping is already sufficient to produce a sizable effect, even at moderate fluences.

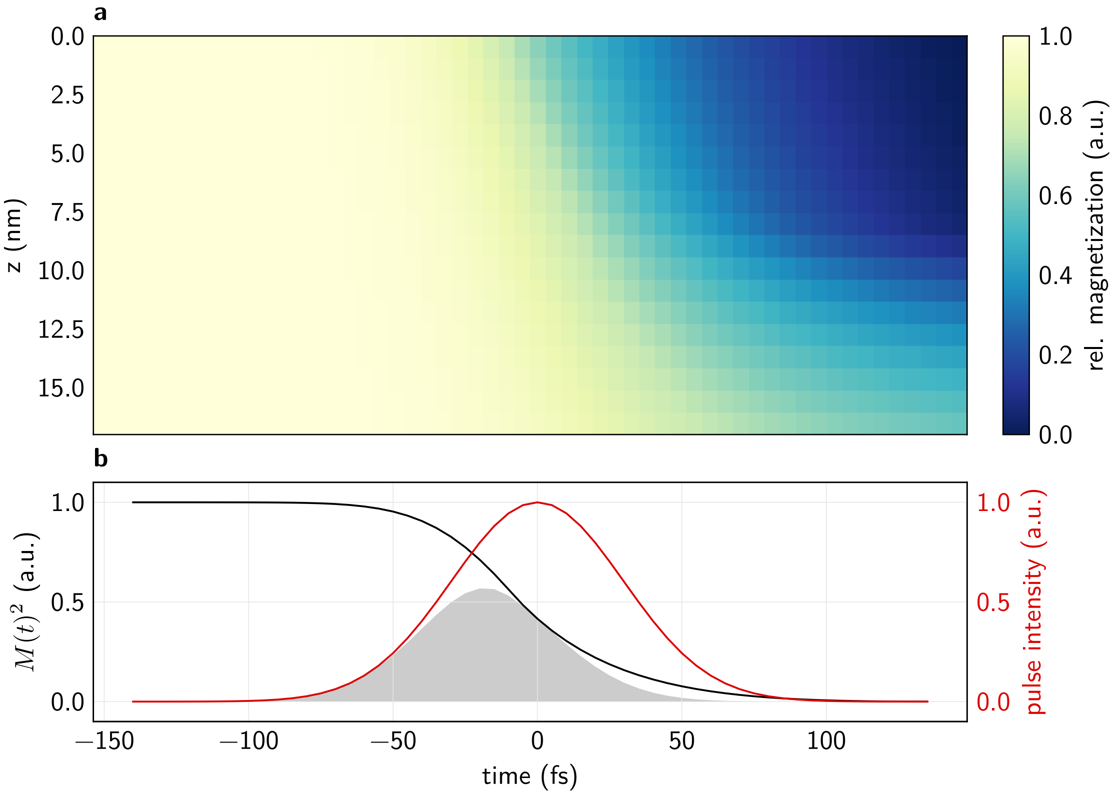

Figure 7.15.: Simulated magnetization profile. Simulation parameters are: FEL fluence 100 mJ/cm², saturation fluence 10 mJ/cm², FEL pulse length 70 fs, demagnetization time constant 100 fs. **a)** 2d-map of the magnetization in time and space. The deeper sample slices absorb less energy and their overall demagnetization progress is thus slower. **b)** Squared sample magnetization at z = 0 nm (black curve) and FEL pulse (red curve). The gray shaded area is the product of both curves and corresponds to the simulated XMCD signal as given by Eq. (7.16).

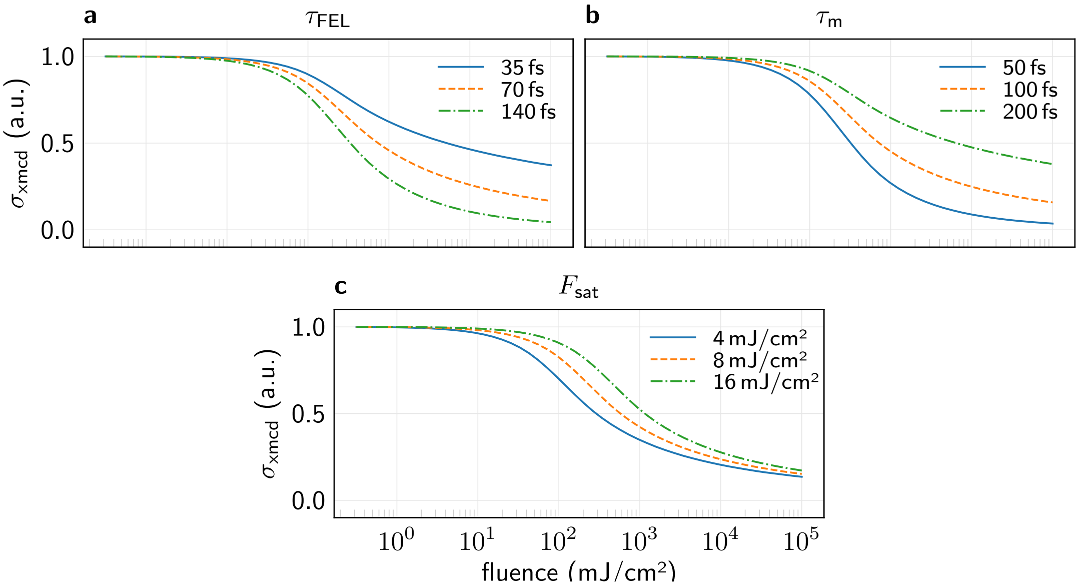

Figure 7.16.: Influence of the different model parameters. The FEL pulse length (**a**), demagnetization time constant (**b**) and saturation fluence (**c**) shift the fluence dependence along the fluence axis without altering its shape. These three parameters are thus effectively coupled. Their unambiguous determination requires independent measurements.

7.4.4. Role of the spatial fluence distribution

So far, the FEL pulse in the simulation is considered to have a spatially homogeneous intensity. However, the detailed shape of the FEL pulse is of pivotal importance for the experiments in this thesis, as Section 7.3.3 demonstrates.

The model directly allows to account for the spatial fluence distribution. For every fluence, the corresponding XMCD signal needs to be calculated and integrated over the whole distribution. The effect of the fluence distribution on the overall fluence dependence is notably different from the other parameters, as Fig. 7.17 shows. The basis of the simulation shown is the WFS-measured fluence distribution during the first experiment (Fig. 7.10a). For comparison, the fluence dependence for “flat” fluence conversion factors of 35 mJ/(cm² µJ) and 110 mJ/(cm² µJ) are shown as well. These values correspond to the 98 % and 99 % percentiles of the measured fluence distribution, respectively.

It is evident, that the spatial fluence distribution changes the overall shape of the simulated fluence dependence. It thus exerts a decidedly different influence than the three coupled model parameters (τ_{FEL}, τ_{m}, F_{sat}). It also produces a region with lower slope at shot energies above 50 µJ. This is reasonable, considering the fluence distribution includes areas of very low, yet non-zero intensity. These areas still contribute noticeably to the overall signal, as discussed in Section 7.3.3. Furthermore, they do not fully demagnetize during the FEL pulse, even at very high (hypothetical) shot energies in excess of 100 µJ.

The spatial fluence distribution thus has a unique influence on the measured signal.

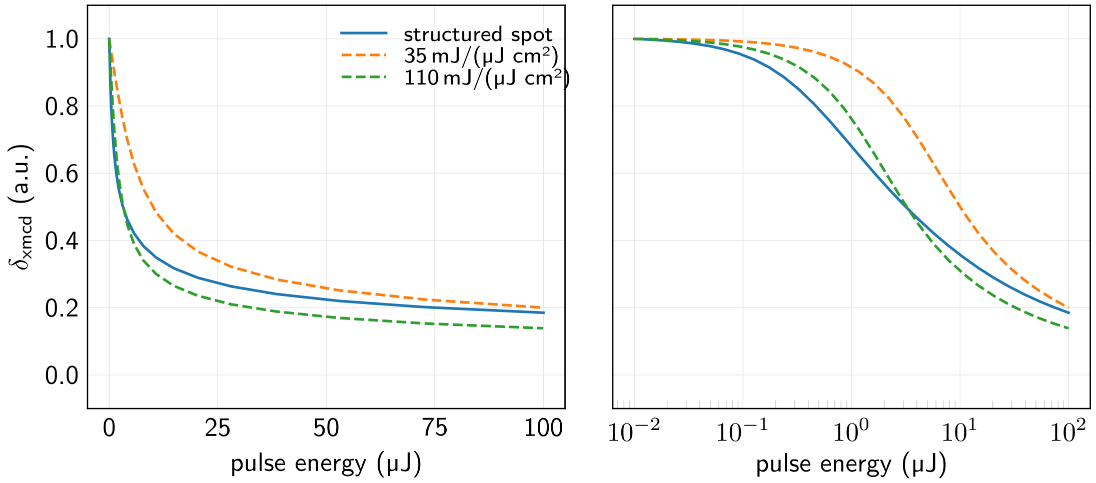

Figure 7.17.: Influence of the spatial fluence distribution on the fluence dependence of the XMCD signal. Solid line: sum over all fluences in the WFS-measured spatial fluence distribution during the first experiment (see Fig. 7.10a). Dashed and dotted lines: constant fluence conversion factors.

Without this detailed knowledge, the constant diffraction cross-section at high fluences could only be explained by residual sample magnetization. Although relevant for our sample system [24, 83], neglecting the spatial fluence distribution would significantly over-estimate this effect. It is thus critically important that the fluence measurements do not truncate a low-intensity background. Of the routinely used methods (see Section 2.5), ablation imprints are especially prone to the latter, since they yield no fluence information below the ablation threshold of the used material.

7.5. Modeling the experimental data

The previous section demonstrated that the spatial fluence distribution is pivotal for the fluence dependence of the diffraction signal. It thus is necessary to use the detailed fluence information – including the sample acceptance – obtained in Section 7.3 to fit the model to the experimentally measured diffraction cross-sections. In order to simulate the change of the diffraction cross-section, it is necessary to assume that the beam position does not change significantly between the low-fluence characterization and the high-fluence single shot. This, and the GMD-measured integral FEL shot energy, allows to separately simulate the low- and high-fluence XMCD signal (I_{xmcd}). The corresponding diffraction cross-section is the XMCD signal, divided by the FEL shot energy:

$$\sigma_{\mathrm{xmcd}} = \frac{I_{\mathrm{xmcd}}}{E_{\mathrm{shot}}} \tag{7.19}$$

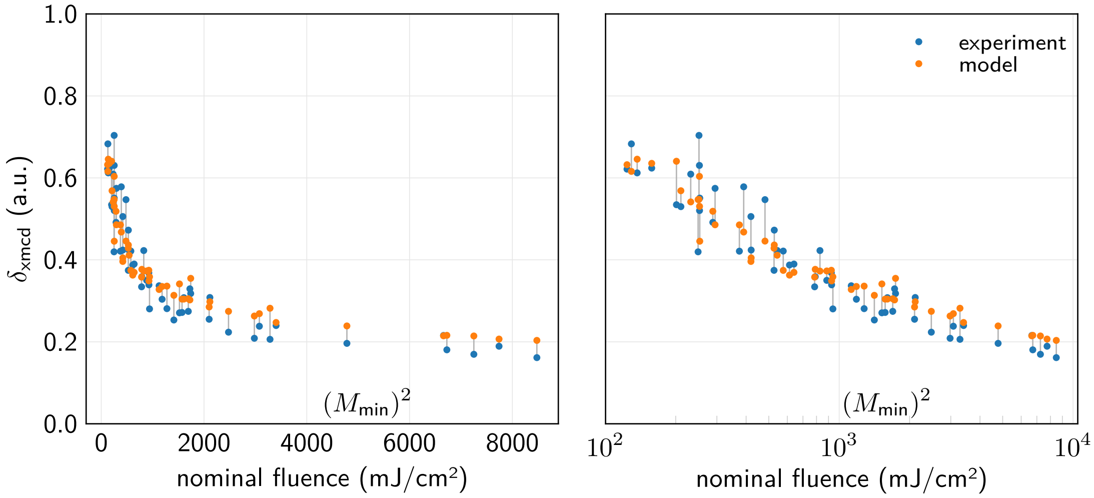

Figure 7.18.: Fit of the demagnetization model with individual fluence information. Thin gray lines mark corresponding experimental and simulated values. The model is not expected to give a smooth line, since the spatial fluence distribution is different for each data point. The deviations for lower fluence values are typically larger, since here the single-shot image is much noisier.

The experiments in this thesis measure the ratio of high- and low-fluence diffraction cross-sections (compare Section 7.2.1):

$$\delta_{\mathrm{xmcd}} = \frac{\sigma^{\mathrm{high}}_{\mathrm{xmcd}}}{\sigma^{\mathrm{low}}_{\mathrm{xmcd}}} \,. \tag{7.20}$$

This quantity is directly accessible from the simulation.

It is thus straightforward to accurately model the experimental situation. The modeling includes the spatial fluence distribution as well as the specific combinations of characterization and single-shot pulse energies. It thus eliminates the fluence distribution as a free fit parameter, which is highly desirable given its strong and complex influence on the diffraction signal.

For every measurement taken, the fitting algorithm simulates the relative change of the diffraction cross-section (δ_{xmcd}). Given the free model parameters (τ_{m} and F_{sat}), the simulation would of course be able to reproduce every single experimental measurement individually without error. This would result in a different set of fit parameters for every measurement. Instead, the algorithm simultaneously minimizes the difference between measured and simulated values using a single set of fit parameters. This is shown in Fig. 7.18 for the data of both experiments, i.e. with the two differing spatial fluence distributions. A single set of parameters simultaneously fits both data-sets very well. The best-fit values are $\tau_{\mathrm{m}} = 90\,\mathrm{fs}$ and $F_{\mathrm{sat}} = 2.5\,\mathrm{mJ/cm^2}$. Note, that the FEL pulse length is not a free parameter. For the given FEL parameters, it is known to be 70(20) fs (short pulses) and 140(20) fs (long pulses) from independent measurements [50].

The remaining diffraction cross-section at fluences exceeding 4000 mJ/cm² is due to

magnetic layer	τ_m (fs)	F_max (mJ/cm^2)	ref.
[Co(4 Å) / Pd(6 Å)]×30	95	11	[24]
[Co(4 Å) / Pd(2 Å)]×20	100	9	[25]
[Co(4 Å) / Pd(6 Å)]×20	160	5.6	[77]
[Co(5 Å) / Pt(10 Å)]×15	180	5.6	[77]
[Co(8 Å) / Pt(14 Å)]×16	<300	14.6	[78]

Table 7.1.: Comparison of literature values for optically induced ultrafast demagnetization. Several of the reported demagnetization time-constants (τ_m) are comparable to the ones in this work. Since all experiments are repetitive (i.e. non-destructive), they typically don't reach very high magnetization quenching values. Even for this lesser amount of quenching, the corresponding fluences are consistently lower than the fitted saturation fluence of 2.5 mJ/cm^2 obtained by the phenomenological model in this section. For optical pumping, the reflectivity and absorption of cap layers has much greater influence, though.

the limited temporal probing range, given by the FEL pulse length, and the low-fluence background in the spatial fluence distribution.

The demagnetization time-constant τ_m and saturation fluence F_sat are coupled parameters, as discussed in the previous section. Their particular values may thus be changed concertedly without affecting the overall quality of the fit. In all cases however, either one, or both parameters are lower by a factor of 2 to 3 compared to reported literature values for comparable magnetic systems (see Table 7.1) [24, 25, 77, 78]. The experiments in these works employ a pump-probe scheme with optical excitation and either optical, or XUV probing. Due to their repetitive nature, they are non-destructive. This is in stark contrast to the experiments in this work, in which a single XUV pulse excites, and simultaneously probes the sample. The lower τ_m and F_sat values may thus be either related to the destructive single-shot measurement scheme, or they might indicate a more efficient demagnetization process under resonant XUV excitation.

The present data does not allow to decide which of these possible explanations is more likely. To do so, it is feasible to perform a similar experiment to the ones discussed here, using optical pulses. In such an experiment, a magneto-optical Kerr effect (MOKE) signal could supplant the XMCD diffraction as a probe for the sample magnetization. Alternatively, XUV-pump/ XUV-probe experiments are possible at FEL sources through split-and-delay units [84], or two-color seeding [85].

7.5.1. Pulse length variation

For a fluence-dependent effect, the number of photons that interact with the sample per unit time and area is decisive. The pulse-length tunability of the FERMI FEL (see Section 2.5) allows for a systematic variation of this parameter. Here, measurements at 70 fs and 120 fs (FWHM) pulse length are taken with comparable integral shot energies. Thus, the number of photons per unit time and area is halved for the 120 fs pulses.

Fig. 7.19 displays the relative XMCD cross-section for both pulse lengths. Here, the 120 fs data has slightly lower δ_xmcd-values than the 70 fs data at comparable fluence.

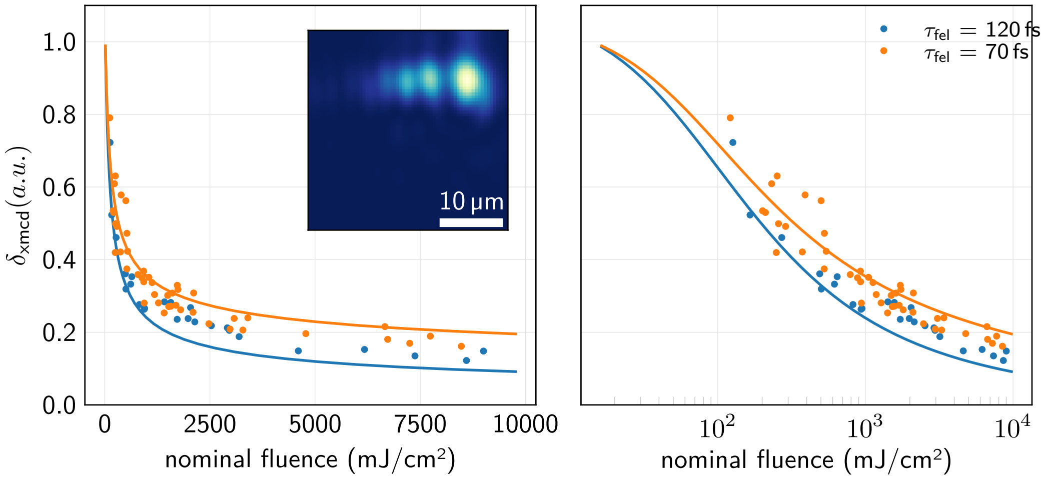

Figure 7.19.: Demagnetization model fit using nominal fluence distributions. Experimental and modeled values of the XMCD diffraction cross-section. Here, the model assumes that all points share the same, nominal spatial fluence distribution (inset) and integral characterization pulse energy. The model parameters are $\tau_{\text{m}} = 90\,\text{fs}$ and $F_{\text{sat}} = 2.5\,\text{mJ/cm}^2$, i.e. the same as previously obtained in the global fit of the data with individual fluence information.

This is already noticeable below $1000\,\text{mJ/cm}^2$, although the general fluence dependence in that fluence region is very steep and the separation is small. At high fluences however, the data measured clearly saturate at different levels.

For the data modeled, Fig. 7.18 shows only points with complete fluence information, including the sample acceptance. Crucially, this excludes all data points with the longer, 120 fs pulses. In order to compare the model's predictions with those data points, a nominal sample alignment is assumed whenever the detailed fluence information is unavailable. Fig. 7.19 shows the nominal fluence distribution and measured δ_{xmcd}-values for the first experiment. The nominal fluence distribution is the most commonly achieved alignment (about 80 % of all cases) and reflects the sample alignment strategy adopted in the experiments.

Using the same parameter values as above, the model predicts a slightly stronger reduction of the diffraction cross-section for the 120 fs pulses. This is in excellent agreement with the experimental data. It is important to note, that this observation – a slightly stronger response at increased FEL pulse lengths – is incompatible with all effects that are based on several photons concurrently interacting with a single atom. This includes stimulated emission [30, 86] and absorption saturation [61]. This, and the excellent agreement of the model with the experimental data, suggests that ultrafast demagnetization is, by far, the dominant effect in the experimental observations.

7.6. Summary

This chapter explores the fluence-dependence of the XMCD diffraction cross-section from thin-film samples with out-of-plane magnetic domains. It is the first systematic study of the fluence dependence of an XMCD diffraction signal in the XUV regime. Using 120 individual samples, it covers nearly three orders of magnitude in fluence – from $10\,\mathrm{mJ/cm^2}$ to $8000\,\mathrm{mJ/cm^2}$. All samples are outfit with a grating monitor that yields integral fluence information. The data obtained reveals a clear fluence-dependence of the XMCD cross-section, which already sets in at the lowest fluences investigated here. These fluences are high compared to synchrotron sources, that produce comparable numbers of photons per second to an FEL source, but distribute them over much more, and significantly longer pulses (e.g. BESSYII synchrotron: 35 ps (FWHM) pulses at 500 MHz; FERMI FEL: 100 fs (FWHM) pulses at 10 Hz). The difference in numbers of photons per second within a single pulse is nine orders of magnitude. However, at FEL sources the fluence dependence of the XMCD diffraction is relevant, even at fluences that induce no permanent damage in the sample and may thus be used routinely in pump-probe experiments.

Accurate knowledge of the spatial fluence distribution on the sample is pivotal in order to model and understand this observation. In the experiment presented, no *in-situ*, spatially resolving fluence monitoring is available. Additional measurements are performed in order to obtain reliable estimates for the fluence distribution and sample acceptance. This information allows for a consistent definition of the nominal fluence for two-dimensional spatial fluence distributions.

In order to understand the fluence dependence of the XMCD diffraction cross-section, a spatially and temporally discrete, numerical model is developed. The model is solely based on ultrafast demagnetization during the FEL pulse propagation through the sample. It makes no assumptions on the microscopic origin of the demagnetization process. It only requires, that XUV photons deposit energy into the sample, which in turn causes an exponentially decaying magnetization level.

The model reproduces the experimental findings with very good accuracy. Several of the model parameters are coupled, which makes their particular magnitudes somewhat ambiguous. Nevertheless, the parameter values are reasonable when compared to literature-reported values. Least-squares fitting yields a single parameter set that simultaneously fits all experimental data measured in this chapter. The spatial fluence distribution on the sample, while not a model parameter in its own right, has a pivotal influence on the simulation results. The model allows to directly factor in the high-quality, detailed fluence information obtained in Section 7.3.

In accord with the experimental results, the model correctly predicts a slightly stronger quenching of the XMCD diffraction cross-section upon doubling the FEL pulse length. This is in conflict with explanations based on multi-photon processes such as stimulated emission, which is proposed to be the dominant mechanism for analogous observations at the $\mathrm{Co\,L_{2,3}}$ absorption resonance. These findings cannot be transferred directly to the experiments in this thesis, since the core-hole life-times and excitation cross-sections differ between the L-edge energies and the Co $M_{2,3}$ resonances investigated here. A direct comparison requires an experiment at the $L_{2,3}$ resonances with the methods developed in this thesis. For the Co $M_{2,3}$ absorption resonance and in the fluence regime investigated here, stimulated emission can only play a minor role for the fluence dependence of XMCD diffraction.

8. Fluence dependent absorption in Cobalt

The previous section demonstrates, that the phenomenological model of ultrafast demagnetization is able to explain the fluence dependence of the XMCD diffraction cross-section very well. However, it uses a number of free parameters, the values of which cannot be determined independently. This leaves some room for additional effects to play a role in the observed fluence dependence. The experiment presented in this section specifically aims to check for evidence of stimulated emission at high XUV fluences.

In an experiment at the Co $\mathrm{L}_{2,3}$ absorption resonance (778 eV), Wu *et al.* observed a reduction of the diffraction cross-sections for both, XMCD and charge diffraction signal. They identified stimulated elastic forward scattering as the fundamental mechanism for this behavior [30]. Although the previous chapter demonstrates that ultrafast demagnetization sufficiently explains the fluence-dependence observed at the Co $\mathrm{M}_{2,3}$ resonances, stimulated emission may still contribute to it, resulting in a combined effect of both mechanisms.

According to Wu *et al.*, the key signature of stimulated emission is enhanced forward (i.e. $\Delta q = 0$) scattering [30]. In their experiment, and similar to the experiments in this thesis, a beamstop blocks the forward direction from detection. Thus, the reduction of all other diffraction signals at $\Delta q > 0$ is the only experimentally accessible signature of enhanced forward emission. The mechanism proposed for this reduction is similar to the selection of a longitudinal mode in an optical laser cavity. The resonantly excited Co layer acts as a single-pass active medium that amplifies (by stimulated emission) the most dominant radiation mode that propagates through it. In the case of an upstream diffracting structure, this dominant mode is usually the forward ($\Delta q = 0$) direction. The emission in this direction is enhanced by stimulated emission, at the expense of all other scattering signals at $\Delta q > 0$ [30].

The principal difference of the experiment in this thesis to the one by Wu *et al.* is the lower photon energy of 59.6 eV, which is in resonance with the Co $\mathrm{M}_{2,3}$ absorption edges. The life-time of the corresponding core-excited states, estimated from reported line widths, is less than 1 fs [87]. Thus, high x-ray photon densities – as are only available at FELs – are necessary to possibly reach stimulated emission. The experiment involves no XMCD-based scattering signal, and thus allows to separate the presumed effect of the stimulated emission from XUV-induced ultrafast demagnetization.

8.1. Experiment description

The experiment described here aims to detect fluence-dependent changes of non-resonant scattering signals in the presence of resonant absorption. The hypotheses to be tested are that (i) non-resonant scattering events exhibit a fluence dependence on samples that also include a resonantly absorbing layer. (ii) This fluence dependence is qualitatively different depending on whether the non-resonant scattering event is followed, or preceded by the resonant absorption. The experiment sketched in Fig. 8.1 is able to simultaneously detect both effects.

The sample consists of three layers – the initial 30 nm Si_3N_4 membrane, a 40 nm thick Co film and another 20 nm layer of Si_3N_4. The intermediate Co layer serves as the active medium. It has a homogeneous in-plane magnetization and hence no XMCD-based scattering signal at $\Delta q > 0$. Both Si_3N_4 layers bear hyperbolic grating monitors that cover the entire 35 µm × 35 µm membrane and share the same parameters ($x_0 = 8.2\,\mathrm{mm}$, $y_0 = 8.2\,\mathrm{mm}$, $m = 60$, $z_{\mathrm{det}} = 10\,\mathrm{cm}$), but are aligned perpendicular to each other. They map their respective illumination functions to the detector where they can be detected simultaneously. The experiment employs the same relative measurement scheme that was successfully used in the previous experiment of this thesis. Thus, every measurement consists of a low-fluence characterization and a high-fluence single shot. This provides a reliable normalization for slight differences of the diffraction cross-section between different gratings and for the spatial jitter of the FEL beam on the sample.

In the presence of stimulated emission, the diffraction cross-section of the upstream grating is expected to decrease, as described in the previous section. At the same time, the absorption in the Co layer would decrease, as the stimulated emission process competes with spontaneous emission and the non-radiative Auger decay [61, 88]. This would result in a larger number of photons scattering from the second grating and thus an apparent increase in its diffraction cross-section. Given the noise level in the diffraction cross-sections measured in the previous experiment of this thesis, the measurement scheme proposed is expected to be able to clearly detect a ±5 % change of the diffraction cross-sections of the down- and upstream grating, respectively. In the experiment by Wu *et al.*, the non-resonant diffraction contrast is reduced by more than 20 % at 300 mJ/cm^2.

8.2. Diffraction image evaluation

Fig. 8.2 shows representative single- and multi-shot diffraction images. The diffracted illumination maps appear slightly sheared, as the combination of grating design and experimental parameters do not fully satisfy far-field conditions (Eq. (4.11)). They still give reliable information on the sample alignment and the spatial fluence distribution, as discussed in Section 8.3. The image evaluation is analogous to Section 7.2.1, except for the fact that the images contain no XMCD signal, but two sets of grating diffraction.

The absolute value of the diffracted intensity differs between front- and backside gratings due to a systematic difference in the FIB ion current during the respective milling process. This results in a slight difference in the grating topography and, consequen-

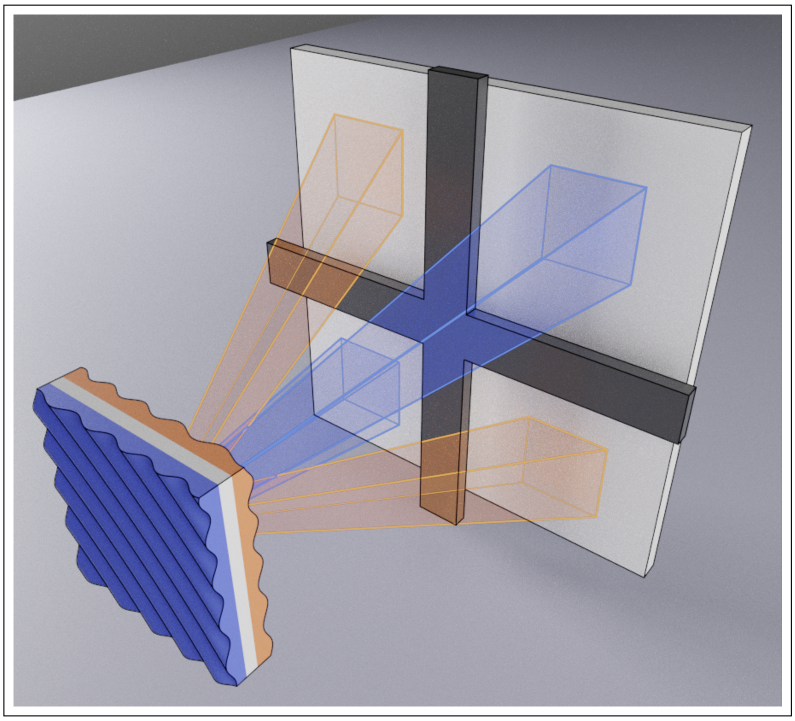

Figure 8.1.: Experiment and sample design to detect stimulated emission The sample is a tri-layer of 30 nm Si_3N_4 (blue), 40 nm Co (white) and 20 nm Si_3N_4 (orange). Both Si_3N_4 layers bear FIB-milled gratings that are oriented perpendicular with respect to each other. Each produces a set of centrosymmetric diffraction spots along the ±45° diagonals. The Co serves as an absorption layer and has no magnetic structure in the detector's sampling range.

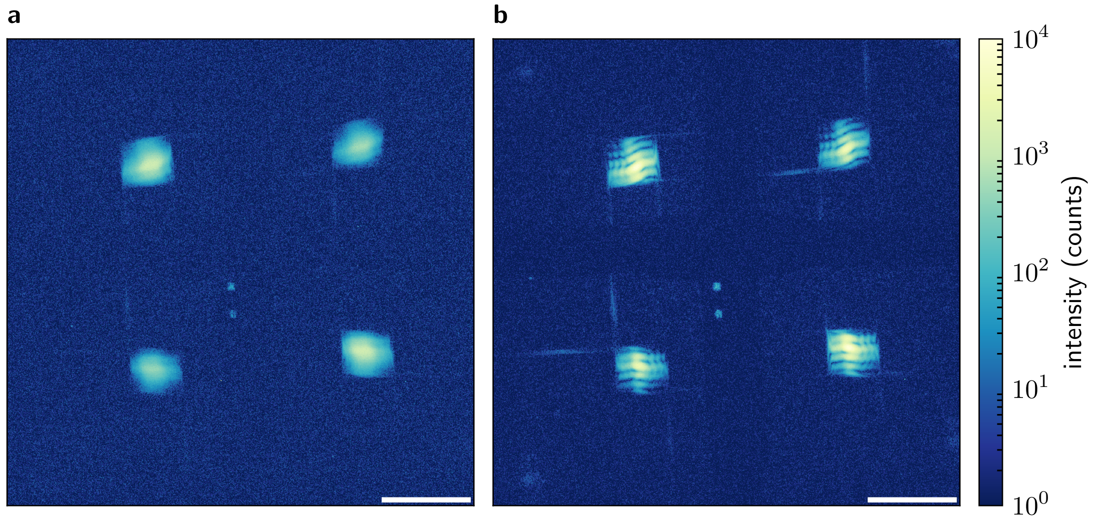

Figure 8.2.: Diffraction images from a double-grating sample. For this particular experiment, the actual detector counts are relevant, since some of the CCD images in the experiment exceed the detector's linear regime (see Section 2.4). Hence, the images are not normalized to $[0, 1]$. Only dark images have been subtracted from the measured diffraction images. **a)** Multi-shot, low-fluence characterization. The internal structure of the FEL spot is partially lost due to spatial jitter (see Section 5.3). **b)** High-fluence single-shot. The four centro-symmetric bright areas are the diffraction patterns of the front- (upper left and lower right) and back-side grating (lower left, upper right). Scale bars are 10 µm^{-1}.

tially, the diffraction cross-section. In order to address these variations, and similarly to the previous experiment, a relative measurement scheme is employed. It consists of a low-fluence calibration, followed by a high-fluence single-shot. Each measurement thus yields four values: The diffracted intensity of the front- and backside grating, each at low and high fluence. The figure of interest in this experiment is the relative diffraction cross-section at high fluence (i.e. relative to the low-fluence characterization):

$$\delta_{\text{front}} = I^{\text{high}}_{\text{front}} / I^{\text{low}}_{\text{front}} \tag{8.1}$$

$$\delta_{\text{back}} = I^{\text{high}}_{\text{back}} / I^{\text{low}}_{\text{back}} \tag{8.2}$$

The ratio of δ_{front} and δ_{back} will reveal any fluence-dependent asymmetry in the diffraction cross-sections. In the presence of stimulated emission, the diffraction cross-section of the front-side (upstream) grating should diminish at high fluences [30].

8.3. Spatial fluence distribution

The gratings in this experiment directly yield the spatial fluence distribution on the sample. The (nominal) fluence values are defined analogous to the detailed description in Section 7.3.3. In contrast to the previous experiment however, the fluence information is directly obtained from the spatially resolved fluence maps of the grating monitors, instead of a combination of WFS, AFM and SEM images. This greatly simplifies the analysis and, at the same time, increases its reliability since a single diffraction image contains all the relevant information.

The comparison with the WFS-measured distribution (Fig. 8.3) shows, that the trapezoid distortion of the diffracted fluence map has only a minor effect on the fluence histogram. With the given FEL spot size and alignment, the sample typically accepts more than 95 % of the incident photons.

8.4. Fluence dependence of the grating diffraction

In total 35 data sets are recorded, each with a characterization image at 5(1) mJ/cm^2 and single-shot fluences varying from 100 mJ/cm^2 to 20 000 mJ/cm^2. The multi-shot diffraction image in Fig. 8.2a suggests that the FEL beam on the sample jumps several micrometer between shots. Section 5.3 evaluates and discusses this behavior in detail. Here, the 35 µm × 35 µm sample membranes are large enough to accommodate the FEL spot including its positioning uncertainty.

Inherently, the fluence maps yield spatially resolved absorption figures. Thus, a single diffraction image already contains a range of fluences due to the variation within the focused FEL spot. Accordingly, a comparison of equivalent regions in the front- and backside grating diffraction will reveal changes in the absorption cross-section of the intermediate Co layer. However, the fluence maps' trapezoid distortion precludes a reliable evaluation in this manner. This is evident in Fig. 8.4. The distortions, though small in themselves, occur in different directions for the front- and backside grating. This difference is due to their respective orientations along the ±45° sample diagonals (see Section 4.3.1). As a result, these distortions dominate the intensity variations between equivalent positions in the fluence maps.

Alternatively, a spatially resolved comparison of the characterization and single-shot measurement for each individual grating could reveal fluence-related alterations of the transmission in the Co layer. However, the spatial jitter during the multi-shot characterization precludes this analysis. Thus, the analysis here only considers the integral intensities in each diffracted fluence map.

Fig. 8.5 displays the ratio of front- and backside grating's diffraction cross-section ($\delta_{\mathrm{front}}/\delta_{\mathrm{back}}$). As expected, the data points scatter around unity, but values at higher shot energies are generally lower. Here, it is important to note that the only apparent change coincides with the saturation of the CCD detector (see Section 2.4). The front-side gratings (upper left and lower right diffraction spots) consistently have a slightly higher diffraction cross-section. This is due to an increased ion current during FIB milling as compared to the back-side gratings. Consequentially, the saturation behavior of the CCD camera affects their diffraction more than that of the back-side gratings.

Thus, the detector's dynamic range limits the highest usable fluence to 5000 mJ/cm^2. Beyond this fluence, the detected intensity levels are no longer proportional to the diffrac-

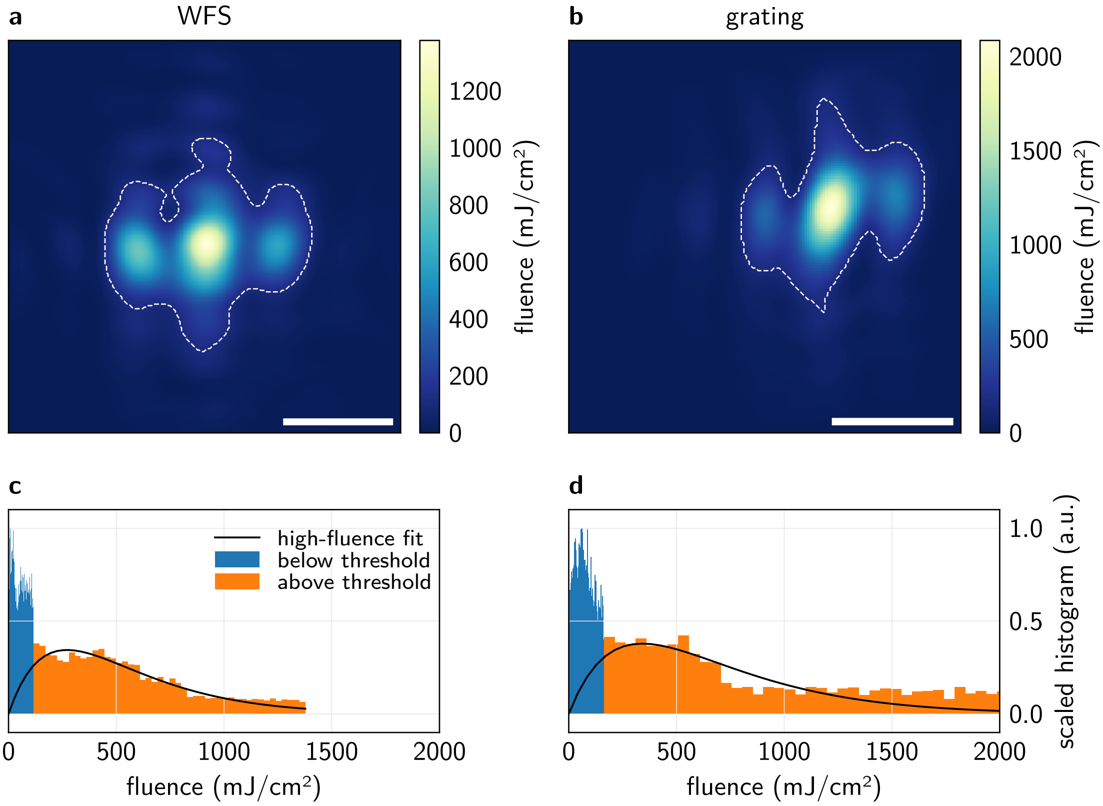

Figure 8.3.: Spatial fluence distribution in the sample plane **a)** Extrapolated image from a single-shot WFS measurement. **b)** Grating diffraction of a 5.4 µJ single-shot. Scale bars are 10 µm. The image areas roughly correspond to the full 35 µm × 35 µm membrane. White dashed lines mark the segmentation threshold for the high- and low-fluence part. **c,d)** Fluence histograms with fit of Eq. (7.12) to the high-fluence part. Histogram counts are scaled to represent the contribution of each fluence value to the detected signal (see Section 7.3.3). The nominal fluence per µJ shot energy is 365(17) mJ/cm² for the WFS measurement, and 386(15) mJ/cm² for the diffracted fluence map. The diffracted fluence map indicates a slightly higher maximum fluence than the WFS measurement.

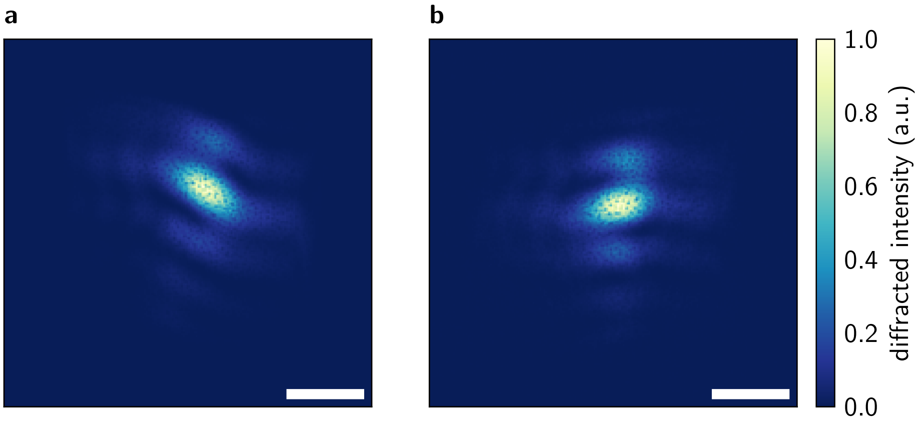

Figure 8.4.: Diffracted single-shot fluence maps of front- and backside grating. a) Front-side (upstream) grating diffraction. **b)** Back-side (downstream) grating diffraction. The trapezoid distortion precludes a direct mapping of equivalent sample positions between both spatial fluence distributions. Scale bars are 10 µm.

tion signal. Within this region, there are no fluence-dependent changes in the diffraction cross-sections, and thus no evidence of stimulated emission.

8.5. Summary

The experiment presented in this chapter specifically tests for stimulated emission as a possible explanation for the fluence dependence observed in the experiment reported in Chapter 7. In the experiment described, the primary signal is the resonant absorption in a 40 nm thick Co layer. Two sets of spatially resolving grating monitors per sample map the spatial fluence distribution before, and after resonant absorption. This approach encodes the resonant absorption cross-section of Co in the non-resonant grating diffraction of the Si_3N_4 fluence monitors. Additionally, the grating monitors greatly reduce the effort that is necessary to obtain reliable information on the spatial fluence distribution. The experimental results indicate that stimulated emission at the Co $M_{2,3}$ edges has no sizable effect on the absorption cross-section up to fluences of $5000\,\mathrm{mJ/cm^2}$. At this fluence, XMCD-based scattering signals at the same absorption resonance are already strongly quenched (by 95 % in the experiment of Müller *et al.* [29] and 85 % in the experiments in this thesis). This rules out the hypothesis that stimulated emission is the dominant mechanism at the Co M-edge.

The experiment extends to significantly higher nominal fluences of up to $20\,000\,\mathrm{mJ/cm^2}$. Here, the detector's saturation behavior precludes a reliable analysis of this data. Designing the gratings such that their diffraction covers a larger area would alleviate this problem. Furthermore, performing this experiment according to the principles derived in the first part of this thesis – with undistorted spatial fluence maps – would make the *peak* fluence available for evaluation, instead of the nominal fluence. Given the FEL beam footprint in this experiment and the maximum integral FEL shot energies of 60 µJ,

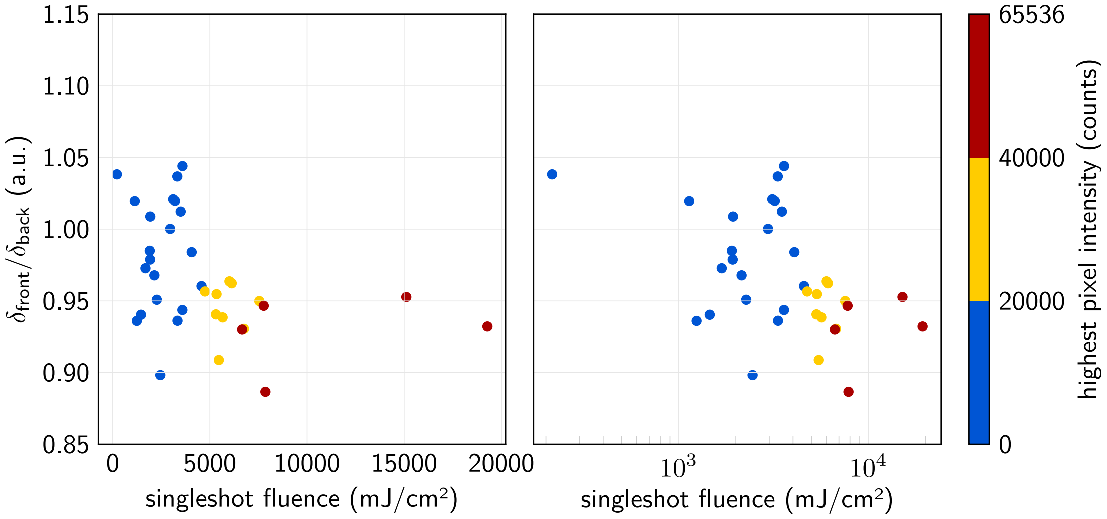

Figure 8.5.: Diffraction cross-section ratios of front- and backside grating. The apparent reduction of the front-side grating's diffraction cross section at fluences above 5000 mJ/cm^2 is due to saturation effects of the CCD detector. This occurs above approximately 20 000 counts.

the peak fluence attainable exceeds 100 000 mJ/cm^2. Such fluences could potentially reveal a threshold beyond which stimulated emission begins to have a sizable effect on the M-edge diffraction cross-sections.

Part IV.

Summary and Outlook

The first part of this thesis describes the development of *in-situ*, spatially resolving fluence monitors for diffraction experiments in transmission geometry. Such monitors can easily be integrated into the Si_3N_4 membranes routinely used as sample support in soft x-ray and XUV experiments. In numerical simulations as well as synchrotron and FEL experiments, their imaging capabilities are explored. Potential aberrations are thoroughly investigated and guidelines developed that ensure aberration-free fluence maps. This results in clear design principles that relate the relevant experimental parameters to the spatial resolution of the fluence maps obtained. The resolution is sufficient to image tightly focused FEL spots with complex internal structures. This is demonstrated in synchrotron and FEL experiments at XUV and soft x-ray wavelengths.

Especially at FELs, the grating monitors are an extremely valuable tool that, for example, facilitates the crucial step of aligning the sample with respect to the beam focus – both in transversal direction as well as along the beam propagation axis. Moreover, the grating monitors are able to provide high-quality fluence information simultaneously to the diffraction experiment. Here, the spatial fluence maps obtained relate to the exact same FEL shot that gives rise to the scattering signal of the sample under study. Given the typical shot-to-shot fluctuations of a focused FEL beam, this is a tremendous advantage over the existing methods that measure the spatial fluence distribution separate from the primary experiment. These are incompatible with a diffraction experiment on solid samples in the forward direction. Furthermore, they cannot guarantee that the plane of the fluence distribution measured coincides with the sample plane, nor can they account for the limited acceptance of a finite sample. Thus, the fluence monitoring concept developed in this thesis is a huge step forward in controlling the spatial fluence distribution that interacts with the sample under study. The very accurate fluence information provided by the grating monitors is extremely valuable for conducting and interpreting fluence-dependent experiments in the XUV and soft x-ray regime. This topic recently has raised considerable interest in the research community and is also subject of the second part of this thesis.

The second part of this thesis investigates the fluence dependence of resonant scattering signals at the $\mathrm{Co\,M_{2,3}}$ absorption resonance. In the first experiment, the signal of interest is the XMCD-based diffraction from 2d magnetic domain patterns with magnetization directions perpendicular to the sample plane. Additional diffraction signals from grating monitors milled into the Si_3N_4 membrane provide an excellent integral normalization source. They account for the limited acceptance of the sample membrane and shot-to-shot fluctuations of the FEL beam position.

The data obtained represents the first systematic study of the XMCD-based diffraction cross-section at the $\mathrm{Co\,M_{2,3}}$ resonance, covering single-shot fluences from $10\,\mathrm{mJ/cm^2}$/pulse to $9000\,\mathrm{mJ/cm^2}$/pulse. It reveals a clear fluence-dependence of the resonant diffraction cross-section that extends over the entire fluence range investigated. The detailed spatial fluence distribution on the sample is crucial for the understanding of this observation. In the absence of spatially resolving grating monitors, additional measurements have to be performed following the diffraction experiment and correlated with each other in order to determine the effective fluence during the experiment. The procedure developed is greatly successful in unifying the results of the two separate FEL beamtimes that comprise the experiment.

A numerical model based on ultrafast demagnetization is developed in order to explain the fluence dependence observed. It accounts for an XUV-induced quenching of the sample magnetization, caused by the FEL pulse traversing through the sample. Using the accurate fluence information obtained before, the model is able to reproduce all of the data measured extremely well using a single set of fit parameters. The thereby obtained material parameters are in excellent agreement with literature-reported values for optically induced ultrafast demagnetization in comparable sample systems. Furthermore, the simulation predicts a slightly stronger quenching of the XMCD diffraction cross-section upon doubling the FEL pulse length. This is in very good quantitative agreement with the experimental data and convincingly excludes multi-photon processes as the dominant mechanism for the fluence dependence observed at the Co $M_{2,3}$ resonance.

In recent publications, stimulated emission has been demonstrated to be responsible for the fluence dependence of XMCD-based diffraction signals at the Co $L_{2,3}$ absorption resonances. The second experiment in this part of the thesis aims to find evidence of stimulated emission at the $M_{2,3}$ resonance of Co. The sample design exploits the literature-reported dependence of non-resonant diffraction cross-sections for scattering events that are followed by resonant stimulated emission. To this end, an in-plane magnetized Co layer is sandwiched between layers of Si_3N_4 that bear FIB-milled fluence monitor gratings. In the presence of stimulated emission in the intermediate Co layer, the diffraction cross-section of the upstream grating is expected to decrease, while that of the downstream grating increases. This qualitative difference provides a very sensitive probe for the onset of stimulated emission. In the experiment performed, no such asymmetry could be detected for fluences up to $5000\,\mathrm{mJ/cm^2}$. The XMCD-based scattering signal of the previous experiment is already strongly quenched at this fluence. Hence, it is unlikely for stimulated emission to play a major role in this fluence region at the Co $M_{2,3}$ resonance.

Both experiments presented in the second part of this thesis were performed before the final version of the spatially resolving grating monitors was developed, and before their imaging capabilities were as thoroughly understood as demonstrated in the first part of this thesis. Consequentially, these experiments suffer from certain limitations. As discussed in the respective sections, additional measurements or alternative procedures in the data analysis were able to alleviate these with good success. Conducting the experiments with spatially resolving fluence monitors has the potential to significantly extend the current understanding of non-linear light–matter interactions in the XUV and soft x-ray regime. In particular, the first experiment on XMCD-based scattering signals should be performed in a similar fashion at the Co $L_{2,3}$ resonance. Such directly comparable results are especially important, since different mechanisms seem to dominate the fluence-dependence at the two absorption resonances. In both cases, the experiment should include the photon energy range before and after the absorption resonances, in order to be able to detect a shift of the resonant transition energy, which has been proposed as an alternative explanation for the fluence dependence observed.

The experiment geared towards detecting stimulated emission has the unique potential to investigate unprecedentedly high soft x-ray and XUV fluences, as it does not average over the spatial fluence distribution. It should thus be carried out at L- and M-edge energies, following the grating design principles derived in the first part of this thesis.

The following section sketches an experiment that exploits the spatially resolved fluence map produced by the grating monitors developed in this thesis to measure the fluence dependence of a material's absorption cross-section in a single FEL shot. The author of this thesis developed the concept shown and submitted it as a beamtime proposal (with input from all co-proposers) [89] for the newly commissioned FEL facility FLASH2. The proposal has been granted beamtime and is scheduled for the second half of 2018.

The basic idea is shown in Fig. 8.6. It is similar to that of the previous chapter – namely, to measure the absorption cross-section via the diffracted fluence maps of a grating monitor. In order to obtain a reliable normalization, the material under study covers only one half of the grating structure. This allows a direct comparison of the transmitted intensity between covered and uncovered regions. Since this also measures the spatial fluence distribution, it is straightforward to map the transmission at a certain position to the corresponding fluence (Fig. 8.7). For smooth or at least symmetric FEL spots, this records the entire fluence-dependence in a single shot. In the case of a more complex spatial fluence distribution, an additional low-fluence calibration measurement is sufficient to obtain the fluence dependence. Hyperbolic grating monitors are the natural choice for this experiment, since the material boundary results in a steep intensity gradient along a predetermined direction. With the correct orientation, the hyperbolic grating monitor is able to map the fluence in this region with very high accuracy.

The approach sketched has several advantages over direct transmission measurements using, for example, a photodiode. Experimentally, the necessary normalization is an integral part of the recorded diffraction images. Hence, such a measurement is not only fast, but also very reliable. Most importantly, the concept does not average over the whole beam footprint. This makes much higher peak fluences accessible for the study of non-linear light–matter interaction in the x-ray and XUV regime. Even with the current-generation of XUV FEL sources, such interactions have, in the XUV regime, only been observed at the L-shell absorption resonances [10, 61, 90]. The main reason for this are the extremely short life times for M-shell core-holes. Here, the experiment outlined could provide the peak-fluence sensitivity that is necessary to observe and study non-linear interactions between XUV photons and these atomic energy levels.

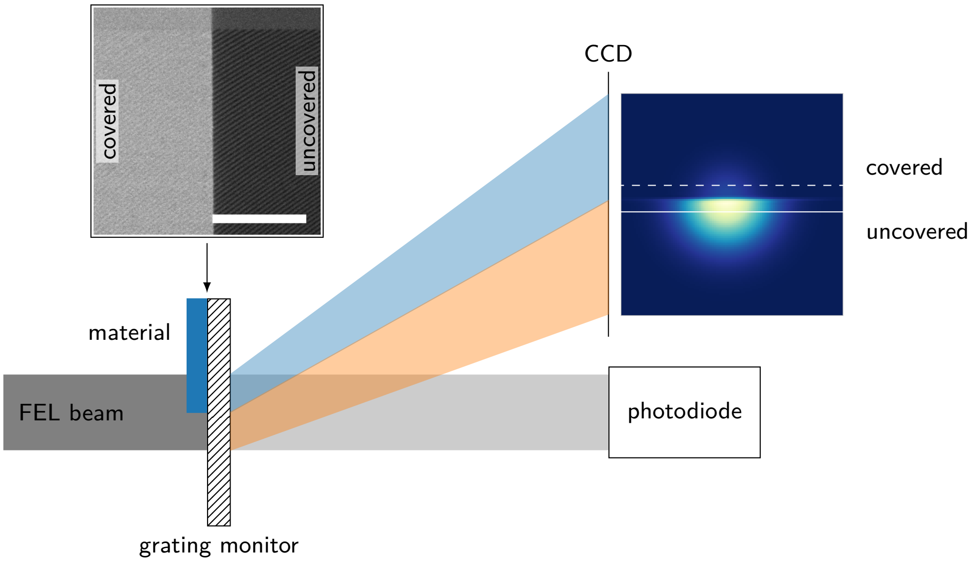

Figure 8.6.: Schematic sketch of a single-shot measurement of fluence-dependent absorption. The sample bears a grating monitor (hatched rectangle) that maps an image of its illumination to the detector. A lithographically fabricated patch of the material under study (blue) covers half of the sample. The left inset shows an SEM image of a fabricated sample with milled grating and thermally evaporated Al patch (bright area). The scale bar corresponds to 5 μm. In this example, the detector is placed off-center and a photo diode records the intensity of the directly transmitted beam. Dashed and solid lines in the simulated detector image mark the positions along which the exemplary analysis of Fig. 8.7 is performed.

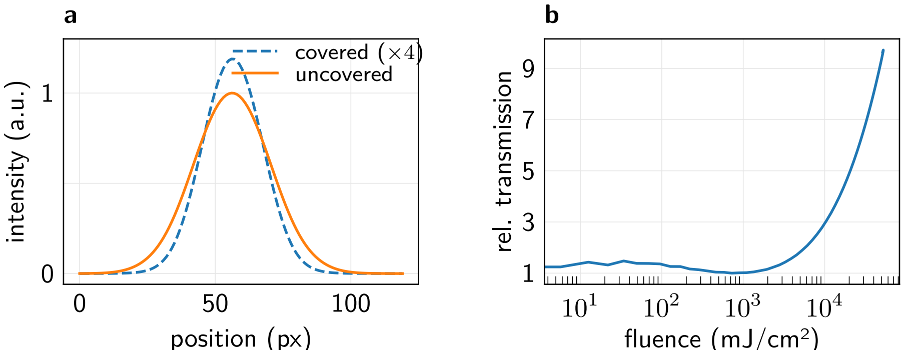

Figure 8.7.: Example calculation for a single-shot absorption cross-section measurement. a) Intensity along the marker lines in the covered and uncovered region of the detector image (dashed and solid, respectively). **b)** Transmission of the Al-layer, normalized to the low-fluence (linear) case and plotted over the incident fluence. All values – including the fluence-axis – are extracted from the simulated single-shot detector image in Fig. 8.6 and knowledge of the total shot energy of 10 μJ. The simulation assumes a Gaussian spot of 10 μm FWHM and uses values from the reported figures of fluence-dependent absorption in Al reported by Nagler *et al.* [61].

A. Source code of the demagnetization model

```python
#!, /usr/bin/env python3
# -*- coding: utf-8 -*-
"""
Created on Thu Jan 18 17:03:36 2018

Model magnetization during XUV pulse.

@author: Michael Schneider
"""

import numpy as np
import xarray as xr
from scipy.special import erf, erfinv


def gauss_pulse(t, t0, amp, fwhm):
    '''
    standard gaussian of width <fwhm> and (integrated) amplitude <amp>
    '''
    sigma = fwhm / (2 * np.sqrt(2 * np.log(2)))
    c = 1 / sigma / np.sqrt(2 * np.pi)
    pulse = c * np.exp(-(t - t0) ** 2 / (2 * sigma ** 2))
    pulse = pulse / pulse.sum()
    return amp * pulse



def sim_demag(fluence, pulse_fwhm, tau_m, E_sat, M_min=0, step_t=10, step_z=1):
    '''

    Parameters
    ----------
    fluence :
        integral pulse energy per unit area (mJ/cm²)

    pulse_fwhm :
        full width at half maximum of the pulse (fs)

    tau_m :
        time constant for ultra-fast demagnetization (fs)

    P_sat :
        Saturation energy density in mJ/cm³
    M_min :
        lower boundary of the magnetization. If zero (default), magnetization
        is allowed to quench completely

    step_t : default: 10
        temporal stepsize (fs)

    step_z : default: 1
        spatial stepsize (nm)
    '''
    samplesize = 18
    n_z = int(samplesize / step_z)
    z = np.linspace(0, samplesize - step_z, n_z)#[:, None, None]
    l_abs = 10.59  # Co72Pd28 @ 60eV (CXRO)
    absorb = (1 - np.exp(-step_z / l_abs)) / step_z  # fraction of absorbed E per slice
    z_intensity = xr.DataArray(np.exp(-z / l_abs), coords=[z], dims=['z'])  # remaining intensity at sli

#    sq2 = np.sqrt(2)
    sigma = pulse_fwhm / (2 * np.sqrt(2 * np.log(2)))
    # time at which accumulated energy exceeds 1e-3 * E_sat -> start modeling here
#    t_start = sq2 * sigma * erfinv(2e-3 * E_sat / (fluence * absorb) - 1)

    t = np.arange(-2 * pulse_fwhm, 2 * pulse_fwhm, step_t)
    t = xr.DataArray(t, coords=[t], dims=['t'])
    pulse = np.exp(-(t ** 2) / (2 * sigma ** 2))
    pulse *= fluence / pulse.sum()

    E_accum = (absorb * z_intensity * pulse).cumsum('t')
    delta_M_sum = (E_accum / E_sat).clip(0, 1 - M_min)
    delta_M = delta_M_sum.diff('t', label='lower')
    delta_M = delta_M.rename(t='t0')
    mag_initial = np.ones_like(E_accum) / n_z

    # t_demag is (t - t_0)
    t_demag = np.clip(t - delta_M.t0, 0, np.inf)
    demag_rel = delta_M - delta_M * np.exp(-t_demag / tau_m)
    demag_rel = demag_rel.sum('t0')
    magnetization = mag_initial * (1 - demag_rel)

    # the intensity profile cancels out, as the stronger signal from the upper
    # layers needs to pass through the remaining sample
    xmcd = (pulse * magnetization ** 2).sum()

    sim = dict(pulse=pulse, magnetization=magnetization, xmcd=xmcd.data)
    return sim


def sim_fluence_distribution(fluence_dist, pulselength, **sim_kw):
    '''
    Simulate xmcd signal for arbitrary spatial fluence distributions.
    To save computation time, the function calculates a histogram of the
    input fluence distribution with a configurable number of bins.
```

```
Parameters
----------
fluence_dist : 2d array
    Spatial fluence distribution in mJ/cm².

pulselength :
    FEL pulse duration (FWHM) in fs

sim_kw :
    keywords that get passed to sim_demag() function

Returns
-------
sig_xmcd :
    Integral XMCD signal
'''
from skimage.filters import threshold_li

sim_kwords = {'E_sat': 10, 'tau_m': 80}
sim_kwords.update(sim_kw)

thresh = threshold_li(fluence_dist)
sig_xmcd = 0.
for func_comp in [np.less, np.greater_equal]:
    sel = func_comp(fluence_dist, thresh)
    factor = fluence_dist[sel].sum() / fluence_dist.sum()
    hist, bins = np.histogram(fluence_dist[sel], bins='auto')
    for num_occurence, fluence in zip(hist, bins[:-1]):
        sim = sim_demag(fluence, pulselength, **sim_kwords)
```

Bibliography

1. Schneider, M., Günther, C. M., von Korff Schmising, C., Pfau, B. & Eisebitt, S. Curved gratings as an integrated photon fluence monitor in x-ray transmission scattering experiments. *Opt. Express* **24,** 13091 (2016) (cit. on pp. xv, 27, 29, 66).
2. Schneider, M., Günther, C. M., Pfau, B., Capotondi, F., Manfredda, M., Zangrando, M., Mahne, N., Raimondi, L., Pedersoli, E., Naumenko, D. & Eisebitt, S. In situ single-shot diffractive fluence mapping for X-ray free-electron laser pulses. *Nat. Commun.* **9,** 214 (2018) (cit. on p. xv).
3. Schneider, M., Günther, C. M., Pfau, B., Capotondi, F., Manfredda, M., Zangrando, M., Mahne, N., Raimondi, L., Pedersoli, E. & Eisebitt, S. In-situ single-shot diffractive fluence mapping for X-ray free-electron laser pulses. *Arxiv.* arXiv: `1705.03814` (2017) (cit. on p. xv).
4. Franken, P. A., Hill, A. E., Peters, C. W. & Weinreich, G. Generation of Optical Harmonics. *Phys. Rev. Lett.* **7,** 118–119 (1961) (cit. on p. 3).
5. Feldhaus, J., Arthur, J. & Hastings, J. B. X-ray free-electron lasers. *J. Phys. B At. Mol. Opt. Phys.* **38,** 799–819 (2005) (cit. on pp. 3, 5).
6. Gaffney, K. J. & Chapman, H. N. Imaging Atomic Structure and Dynamics with Ultrafast X-ray Scattering. *Science (80-.).* **316,** 1444–1448 (2007) (cit. on pp. 3, 61).
7. Chen, M. C., Arpin, P., Popmintchev, T., Gerrity, M., Zhang, B., Seaberg, M., Popmintchev, D., Murnane, M. M. & Kapteyn, H. C. Bright, coherent, ultrafast soft x-ray harmonics spanning the water window from a tabletop light source. *Phys. Rev. Lett.* **105,** 1–4. arXiv: `1006.3942` (2010) (cit. on p. 4).
8. Rupp, D., Monserud, N., Langbehn, B., Sauppe, M., Zimmermann, J., Ovcharenko, Y., Möller, T., Frassetto, F., Poletto, L., Trabattoni, A., Calegari, F., Nisoli, M., Sander, K., Peltz, C., Vrakking, M. J., Fennel, T. & Rouzée, A. Coherent diffractive imaging of single helium nanodroplets with a high harmonic generation source. *Nat. Commun.* **8,** 1–7. arXiv: `1610.05997` (2017) (cit. on p. 4).
9. Henke, B. L., Gullikson, E. M. & Davis, J. C. x-ray interactions: photoabsorption, scattering, transmission, and reflection at e = 50-30000eV, Z=1-92. *At. data Nucl. data tables* **54,** 181–342 (1993) (cit. on pp. 4, 9, 13, 18, 39, 61, 77).
10. Beye, M., Schreck, S., Sorgenfrei, F., Trabant, C., Pontius, N., Schüßler-Langeheine, C., Wurth, W. & Föhlisch, A. Stimulated X-ray emission for materials science. *Nature* **501,** 191–194 (2013) (cit. on pp. 4, 27, 101).

11. Young, L., Kanter, E. P., Kräsignssig, B., Li, Y., March, A. M., Pratt, S. T., Santra, R., Southworth, S. H., Rohringer, N., Dimauro, L. F., Doumy, G., Roedig, C. A., Berrah, N., Fang, L., Hoener, M., Bucksbaum, P. H., Cryan, J. P., Ghimire, S., Glownia, J. M., Reis, D. A., Bozek, J. D., Bostedt, C. & Messerschmidt, M. Femtosecond electronic response of atoms to ultra-intense X-rays. *Nature* **466,** 56–61 (2010) (cit. on p. 4).

12. Chapman, H., Barty, A., Bogan, M. J., Boutet, S., Frank, M., Hau-Riege, S. P., Marchesini, S., Woods, B. W., Bajt, S., Benner, W. H., London, R. A., Plönjes, E., Kuhlmann, M., Treusch, R., Düsterer, S., Tschentscher, T., Schneider, J. R., Spiller, E., Möller, T., Bostedt, C., Hoener, M., Shapiro, D. A., Hodgson, K. O., van der Spoel, D., Burmeister, F., Bergh, M., Caleman, C., Huldt, G., Seibert, M. M., Maia, F. R. N. C., Lee, R. W., Szöke, A., Timneanu, N., Hajdu, J., Stefan, P., Marchesini, S., Woods, B. W., Benner, W. H., London, R. A., Kuhlmann, M., Treusch, R., Tschentscher, T., Schneider, J. R., Spiller, E., Bostedt, C., Hoener, M., Shapiro, D. A., Hodgson, K. O., Spoel, D. V. D., Burmeister, F., Bergh, M., Caleman, C., Seibert, M. M., Lee, R. W., Timneanu, N., Hajdu, J., Hau-Riege, S. P., Bajt, S., Plönjes, E., Düsterer, S., Möller, T., van der Spoel, D., Huldt, G., Maia, F. R. N. C. & Szöke, A. Femtosecond diffractive imaging with a soft-X-ray free-electron laser. *Nat. Phys.* **2,** 839–843. arXiv: `0610044 [physics]` (2006) (cit. on pp. 4, 6, 64).

13. Allaria, E., Callegari, C., Cocco, D., Fawley, W. M., Kiskinova, M., Masciovecchio, C. & Parmigiani, F. The FERMI@Elettra free-electron-laser source for coherent x-ray physics: photon properties, beam transport system and applications. *New J. Phys.* **12,** 075002 (2010) (cit. on pp. 5, 13).

14. Tiedtke, K., Feldhaus, J., Hahn, U., Jastrow, U., Nunez, T., Tschentscher, T., Bobashev, S. V., Sorokin, A. A., Hastings, J. B., Möller, S., Cibik, L., Gottwald, A., Hoehl, A., Kroth, U., Krumrey, M., Schöppe, H., Ulm, G., Richter, M., Möller, S. & Schöppe, H. Gas detectors for x-ray lasers. *J. Appl. Phys.* **103,** 094511 (2008) (cit. on pp. 6, 13).

15. Keitel, B., Plönjes, E., Kreis, S., Kuhlmann, M., Tiedtke, K., Mey, T., Schäfer, B. & Mann, K. Hartmann wavefront sensors and their application at FLASH. *J. Synchrotron Radiat.* **23,** 43–49 (2016) (cit. on pp. 6, 13).

16. Le Pape, S., Zeitoun, P., Idir, M., Dhez, P., Rocca, J. J. & François, M. Electromagnetic-Field Distribution Measurements in the Soft X-Ray Range: Full Characterization of a Soft X-Ray Laser Beam. *Phys. Rev. Lett.* **88,** 183901 (2002) (cit. on pp. 6, 13).

17. Schäfer, B. & Mann, K. Determination of Beam Parameters and Coherence Properties of Laser Radiation by Use of an Extended Hartmann-Shack Wave-Front Sensor. *Appl. Opt.* **41,** 2809–2817 (2002) (cit. on pp. 6, 13).

18. Chalupsky, J., Krzywinski, J., Juha, L., Hájková, V., Cihelka, J., Burian, T., Vyšín, L., Gaudin, J., Gleeson, A., Jurek, M., Khorsand, a. R., Klinger, D., Wabnitz, H., Sobierajski, R., Störmer, M., Tiedtke, K. & Toleikis, S. Spot size characterization

of focused non-Gaussian X-ray laser beams. *Opt. Express* **18,** 27836 (2010) (cit. on pp. 6, 13, 17).

19. Nelson, A. J., Toleikis, S., Chapman, H., Bajt, S., Krzywinski, J., Chalupsky, J., Juha, L., Cihelka, J., Hajkova, V., Vyšín, L., Burian, T., Kozlova, M., Fäustlin, R., Nagler, B., Vinko, S., Whitcher, T., Dzelzainis, T., Renner, O., Saksl, K., Khorsand, A. R., Heimann, P. A., Sobierajski, R., Klinger, D., Jurek, M., Pelka, J., Iwan, B., Andreasson, J., Timneanu, N., Fajardo, M., Wark, J., Riley, D., Tschentscher, T., Hajdu, J. & Lee, R. W. Soft x-ray free electron laser microfocus for exploring matter under extreme conditions. *Opt. Express* **17,** 18271 (2009) (cit. on pp. 6, 13).
20. Yumoto, H., Mimura, H., Koyama, T., Matsuyama, S., Tono, K., Togashi, T., Inubushi, Y., Sato, T., Tanaka, T., Kimura, T., Yokoyama, H., Kim, J., Sano, Y., Hachisu, Y., Yabashi, M., Ohashi, H., Ohmori, H., Ishikawa, T. & Yamauchi, K. Focusing of X-ray free-electron laser pulses with reflective optics. *Nat. Photonics* **7,** 43–47 (2012) (cit. on pp. 6, 55).
21. Mimura, H., Yumoto, H., Matsuyama, S., Koyama, T., Tono, K., Inubushi, Y., Togashi, T., Sato, T., Kim, J., Fukui, R., Sano, Y., Yabashi, M., Ohashi, H., Ishikawa, T. & Yamauchi, K. Generation of 1020 W cm—2 hard X-ray laser pulses with two-stage reflective focusing system. *Nat. Commun.* **5** (2014) (cit. on pp. 6, 55).
22. Vartanyants, I. A., Singer, A., Mancuso, A. P., Yefanov, O. M., Sakdinawat, A., Liu, Y., Bang, E., Williams, G. J., Cadenazzi, G., Abbey, B., Sinn, H., Attwood, D. T., Nugent, K. A., Weckert, E., Wang, T., Zhu, D., Wu, B., Graves, C., Scherz, A. O., Turner, J. J., Schlotter, W. F., Messerschmidt, M., Lüning, J., Acremann, Y., Heimann, P., Mancini, D. C., Joshi, V., Krzywinski, J., Soufli, R., Fernandez-Perea, M., Hau-Riege, S., Peele, A. G., Feng, Y., Krupin, O., Moeller, S. & Wurth, W. Coherence Properties of Individual Femtosecond Pulses of an X-Ray Free-Electron Laser. *Phys. Rev. Lett.* **107,** 144801 (2011) (cit. on p. 6).
23. Seibert, M. M., Ekeberg, T., Maia, F. R. N. C., Svenda, M., Andreasson, J., Jönsson, O., Odić, D., Iwan, B., Rocker, A., Westphal, D., Hantke, M., DePonte, D. P., Barty, A., Schulz, J., Gumprecht, L., Coppola, N., Aquila, A. L., Liang, M., White, T. A., Martin, A., Caleman, C., Stern, S., Abergel, C., Seltzer, V., Claverie, J.-M., Bostedt, C., Bozek, J. D., Boutet, S., Miahnahri, A. A., Messerschmidt, M., Krzywinski, J., Williams, G., Hodgson, K. O., Bogan, M. J., Hampton, C. Y., Sierra, R. G., Starodub, D., Andersson, I., Bajt, S., Barthelmess, M., Spence, J. C. H., Fromme, P., Weierstall, U., Kirian, R., Hunter, M., Doak, R. B., Marchesini, S., Hau-Riege, S. P., Frank, M., Shoeman, R. L., Lomb, L., Epp, S. W., Hartmann, R., Rolles, D., Rudenko, A., Schmidt, C., Foucar, L., Kimmel, N., Holl, P., Rudek, B., Erk, B., Hömke, A., Reich, C., Pietschner, D., Weidenspointner, G., Strüder, L., Hauser, G., Gorke, H., Ullrich, J., Schlichting, I., Herrmann, S., Schaller, G., Schopper, F., Soltau, H., Kühnel, K.-U., Andritschke, R., Schröter, C.-D., Krasniqi, F., Bott, M., Schorb, S., Rupp, D., Adolph, M., Gorkhover, T., Hirsemann, H., Potdevin, G., Graafsma, H., Nilsson, B., Chapman, H. & Hajdu, J. Single mimivirus

particles intercepted and imaged with an X-ray laser. *Nature* **470,** 78–81 (2011) (cit. on p. 6).

24. Vodungbo, B., Gautier, J., Lambert, G., Sardinha, A. B., Lozano, M., Sebban, S., Ducousso, M., Boutu, W., Li, K., Tudu, B., Tortarolo, M., Hawaldar, R., Delaunay, R., López-Flores, V., Arabski, J., Boeglin, C., Merdji, H., Zeitoun, P. & Lüning, J. Laser-induced ultrafast demagnetization in the presence of a nanoscale magnetic domain network. *Nat. Commun.* **3,** 999 (2012) (cit. on pp. 6, 75, 77, 82, 84).

25. von Korff Schmising, C., Pfau, B., Schneider, M., Günther, C. M., Giovannella, M., Perron, J., Vodungbo, B., Müller, L., Capotondi, F., Pedersoli, E., Mahne, N., Lüning, J. & Eisebitt, S. Imaging Ultrafast Demagnetization Dynamics after a Spatially Localized Optical Excitation. *Phys. Rev. Lett.* **112,** 217203 (2014) (cit. on pp. 6, 19, 75, 77, 84).

26. Ostler, T. a., Barker, J., Evans, R. F. L., Chantrell, R. W., Atxitia, U., Chubykalo-Fesenko, O., El Moussaoui, S., Le Guyader, L., Mengotti, E., Heyderman, L. J., Nolting, F., Tsukamoto, A., Itoh, A., Afanasiev, D., Ivanov, B. a., Kalashnikova, A. M., Vahaplar, K., Mentink, J., Kirilyuk, A., Rasing, T. & Kimel, A. V. Ultrafast heating as a sufficient stimulus for magnetization reversal in a ferrimagnet. *Nat. Commun.* **3,** 666. arXiv: `arXiv:1011.1669v3` (2012) (cit. on p. 6).

27. Büttner, F., Moutafis, C., Schneider, M., Krüger, B., Günther, C. M., Geilhufe, J., Schmising, C. v. K., Mohanty, J., Pfau, B., Schaffert, S., Bisig, A., Foerster, M., Schulz, T., Vaz, C. A. F., Franken, J. H., Swagten, H. J. M., Kläui, M. & Eisebitt, S. Dynamics and inertia of skyrmionic spin structures. *Nat. Phys.* **11,** 225–228 (2015) (cit. on p. 6).

28. Wang, T., Zhu, D., Wu, B., Graves, C., Schaffert, S., Rander, T., Müller, L., Vodungbo, B., Baumier, C., Bernstein, D. P., Bräuer, B., Cros, V., de Jong, S., Delaunay, R., Fognini, A., Kukreja, R., Lee, S., López-Flores, V., Mohanty, J., Pfau, B., Popescu, H., Sacchi, M., Sardinha, A. B., Sirotti, F., Zeitoun, P., Messerschmidt, M., Turner, J. J., Schlotter, W. F., Hellwig, O., Mattana, R., Jaouen, N., Fortuna, F., Acremann, Y., Gutt, C., Dürr, H. A., Beaurepaire, E., Boeglin, C., Eisebitt, S., Grübel, G., Lüning, J., Stöhr, J. & Scherz, A. O. Femtosecond Single-Shot Imaging of Nanoscale Ferromagnetic Order in Co/Pd Multilayers Using Resonant X-Ray Holography. *Phys. Rev. Lett.* **108,** 267403 (2012) (cit. on pp. 6, 59, 61, 65, 75, 76).

29. Müller, L., Gutt, C., Pfau, B., Schaffert, S., Geilhufe, J., Büttner, F., Mohanty, J., Flewett, S., Treusch, R., Düsterer, S., Redlin, H., Al-Shemmary, A., Hille, M., Kobs, a., Frömter, R., Oepen, H. P., Ziaja, B., Medvedev, N., Son, S.-K., Thiele, R., Santra, R., Vodungbo, B., Lüning, J., Eisebitt, S. & Grübel, G. Breakdown of the X-Ray Resonant Magnetic Scattering Signal during Intense Pulses of Extreme Ultraviolet Free-Electron-Laser Radiation. *Phys. Rev. Lett.* **110,** 234801 (2013) (cit. on pp. 6, 7, 59, 65, 95).

30. Wu, B., Wang, T., Graves, C. E., Zhu, D., Schlotter, W. F., Turner, J. J., Hellwig, O., Chen, Z., Dürr, H. A., Scherz, A. O. & Stöhr, J. Elimination of X-Ray Diffraction through Stimulated X-Ray Transmission. *Phys. Rev. Lett.* **117,** 027401 (2016) (cit. on pp. 6, 7, 59, 65, 85, 89, 90, 92).
31. Suzuki, K., Matsui, J. & Torikai, T. SiN membrane masks for x?ray lithography. *J. Vac. Sci. Technol.* **20,** 191–194 (1982) (cit. on p. 9).
32. Seshan, K. *Handbook of Thin-Film Deposition Processes and Techniques - Principles, Methods, Equipment and Applications (2nd Edition)* 312 (2002) (cit. on pp. 9, 19).
33. Goodman, J. W. *Introduction To Fourier Optics* 3rd ed., 491 (Roberts & Company Publishers, 2007) (cit. on pp. 10, 21, 22, 23, 29, 37, 38, 49).
34. Stöhr, J. & Siegmann, H. C. *Magnetism* (Springer Berlin Heidelberg, Berlin, Heidelberg, 2006) (cit. on pp. 10, 12).
35. Valencia, S., Gaupp, A., Gudat, W., Mertins, H. C., Oppeneer, P. M., Abramsohn, D. & Schneider, C. M. Faraday rotation spectra at shallow core levels: 3p edges of Fe, Co, and Ni. *New J. Phys.* **8** (2006) (cit. on p. 10).
36. Eisebitt, S., Lüning, J., Schlotter, W. F., Lörgen, M., Hellwig, O., Eberhardt, W. & Stöhr, J. Lensless imaging of magnetic nanostructures by X-ray spectro-holography. *Nature* **432,** 885–888. arXiv: `0411074 [cond-mat]` (2004) (cit. on p. 10).
37. Schaffert, S., Pfau, B., Geilhufe, J., Günther, C. M., Schneider, M., Korff Schmising, C. V. & Eisebitt, S. High-resolution magnetic-domain imaging by Fourier transform holography at 21 nm wavelength. *New J. Phys.* **15** (2013) (cit. on p. 10).
38. Willems, F., von Korff Schmising, C., Weder, D., Günther, C. M., Schneider, M., Pfau, B., Meise, S., Guehrs, E., Geilhufe, J., Merhe, A. E. D., Jal, E., Vodungbo, B., Lüning, J., Mahieu, B., Capotondi, F., Pedersoli, E., Gauthier, D., Manfredda, M. & Eisebitt, S. Multi-color imaging of magnetic Co/Pt heterostructures. *Struct. Dyn.* **4,** 014301 (2017) (cit. on p. 10).
39. Kortright, J. B., Kim, S.-K. K., Denbeaux, G. P., Zeltzer, G., Takano, K. & Fullerton, E. E. Soft-x-ray small-angle scattering as a sensitive probe of magnetic and charge heterogeneity. *Phys. Rev. B - Condens. Matter Mater. Phys.* **64,** 924011–924014 (2001) (cit. on pp. 10, 12, 75).
40. Thole, B. T., Carra, P., Sette, F. & van der Laan, G. X-ray circular dichroism as a probe of orbital magnetization. *Phys. Rev. Lett.* **68,** 1943–1946 (1992) (cit. on p. 10).
41. Chen, C., Idzerda, Y., Lin, H.-J., Smith, N., Meigs, G., Chaban, E., Ho, G., Pellegrin, E. & Sette, F. Experimental Confirmation of the X-Ray Magnetic Circular Dichroism Sum Rules for Iron and Cobalt. *Phys. Rev. Lett.* **75,** 152–155 (1995) (cit. on p. 10).

42. Zusin, D., Tengdin, P. M., Gopalakrishnan, M., Gentry, C., Blonsky, A., Gerrity, M., Legut, D., Shaw, J. M., Nembach, H. T., Silva, T. J., Oppeneer, P. M., Kapteyn, H. C. & Murnane, M. M. Direct measurement of the static and transient magneto-optical permittivity of cobalt across the entire M -edge in reflection geometry by use of polarization scanning. *Phys. Rev. B* **97,** 1–11 (2018) (cit. on p. 10).

43. Vaz, C. A. F., Bland, J. A. C. & Lauhoff, G. Magnetism in ultrathin film structures. *Reports Prog. Phys.* **71,** 056501 (2008) (cit. on p. 12).

44. Johnson, M. T., Bloemen, P. J. H., den Broeder, F. J. A. & de Vries, J. J. Magnetic anisotropy in metallic multilayers. *Reports Prog. Phys.* **59,** 1409–1458 (1996) (cit. on p. 12).

45. PI. *PI-MTE 2048B data sheet* (cit. on p. 13).

46. Pedersoli, E., Capotondi, F., Cocco, D., Zangrando, M., Kaulich, B., Menk, R. H., Locatelli, A., Mentes, T. O., Spezzani, C., Sandrin, G., Bacescu, D. M., Kiskinova, M., Bajt, S., Barthelmess, M., Barty, A., Schulz, J., Gumprecht, L., Chapman, H., Nelson, A. J., Frank, M., Pivovaroff, M. J., Woods, B. W., Bogan, M. J. & Hajdu, J. Multipurpose modular experimental station for the DiProI beamline of Fermi@Elettra free electron laser. *Rev. Sci. Instrum.* **82** (2011) (cit. on p. 13).

47. Capotondi, F., Pedersoli, E., Bencivenga, F., Manfredda, M., Mahne, N., Raimondi, L., Svetina, C., Zangrando, M., Demidovich, A., Nikolov, I., Danailov, M. B., Masciovecchio, C. & Kiskinova, M. Multipurpose end-station for coherent diffraction imaging and scattering at FERMI@Elettra free-electron laser facility. *J. Synchrotron Radiat.* **22,** 544–552 (2015) (cit. on p. 13).

48. Zangrando, M., Abrami, A., Bacescu, D. M., Cudin, I., Fava, C., Frassetto, F., Galimberti, A., Godnig, R., Giuressi, D., Poletto, L., Rumiz, L., Sergo, R., Svetina, C. & Cocco, D. The photon analysis, delivery, and reduction system at the FERMI@Elettra free electron laser user facility. *Rev. Sci. Instrum.* **80,** 113110 (2009) (cit. on p. 13).

49. Raimondi, L., Svetina, C., Mahne, N., Cocco, D., Abrami, A., De Marco, M., Fava, C., Gerusina, S., Gobessi, R., Capotondi, F., Pedersoli, E., Kiskinova, M., De Ninno, G., Zeitoun, P., Dovillaire, G., Lambert, G., Boutu, W., Merdji, H., Gonzalez, A., Gauthier, D. & Zangrando, M. Microfocusing of the FERMI@Elettra FEL beam with a K–B active optics system: Spot size predictions by application of the WISE code. *Nucl. Instruments Methods Phys. Res. Sect. A* **710,** 131–138 (2013) (cit. on pp. 13, 15).

50. Finetti, P., Höppner, H., Allaria, E., Callegari, C., Capotondi, F., Cinquegrana, P., Coreno, M., Cucini, R., Danailov, M. B., Demidovich, A., Ninno, G. D., Fraia, M. D., Feifel, R., Ferrari, E., Fröhlich, L., Gauthier, D., Golz, T., Grazioli, C., Kai, Y., Kurdi, G., Mahne, N., Manfredda, M., Medvedev, N., Nikolov, I. P., Pedersoli, E., Penco, G., Plekan, O., Prandolini, M. J., Prince, K. C., Raimondi, L., Rebernik, P., Riedel, R., Roussel, E., Sigalotti, P., Squibb, R., Stojanovic, N., Stranges, S., Svetina, C., Tanikawa, T., Teubner, U., Tkachenko, V., Toleikis, S., Zangrando,

M., Ziaja, B., Tavella, F. & Giannessi, L. Pulse duration of seeded free-electron lasers. *Phys. Rev. X* **7,** 1–19 (2017) (cit. on pp. 15, 83).

51. Flöter, B., Juranic, P., Kapitzki, S., Keitel, B., Mann, K., Plönjes, E., Schäfer, B. & Tiedtke, K. EUV Hartmann sensor for wavefront measurements at the Free-electron LASer in Hamburg. *New J. Phys.* **12** (2010) (cit. on p. 16).
52. Weidenspointner, G., Epp, S. W., Hartmann, A., Hartmann, R., Hauser, G., Holl, P., Kimmel, N., Rolles, D., Str?der, L. & Ullrich, J. *Practical experience from operating the imaging pnCCD instrument of the CAMP chamber at LCLS* in (eds Tschentscher, T. & Cocco, D.) (2011), 80780U (cit. on p. 16).
53. Strüder, L., Epp, S. W., Rolles, D., Hartmann, R., Holl, P., Lutz, G., Soltau, H., Eckart, R., Reich, C., Heinzinger, K., Thamm, C., Rudenko, A., Krasniqi, F., Kühnel, K.-U., Bauer, C., Schröter, C.-D., Moshammer, R., Techert, S., Miessner, D., Porro, M., Hälker, O., Meidinger, N., Kimmel, N., Andritschke, R., Schopper, F., Weidenspointner, G., Ziegler, A., Pietschner, D., Herrmann, S., Pietsch, U., Walenta, A., Leitenberger, W., Bostedt, C., Möller, T., Rupp, D., Adolph, M., Graafsma, H., Hirsemann, H., Gärtner, K., Richter, R., Foucar, L., Shoeman, R. L., Schlichting, I. & Ullrich, J. Large-format, high-speed, X-ray pnCCDs combined with electron and ion imaging spectrometers in a multipurpose chamber for experiments at 4th generation light sources. *Nucl. Instruments Methods Phys. Res. Sect. A Accel. Spectrometers, Detect. Assoc. Equip.* **614,** 483–496 (2010) (cit. on p. 16).
54. Stojanovic, N., Von Der Linde, D., Sokolowski-Tinten, K., Zastrau, U., Perner, F., Förster, E., Sobierajski, R., Nietubyc, R., Jurek, M., Klinger, D., Pelka, J., Krzywinski, J., Juha, L., Cihelka, J., Velyhan, A., Koptyaev, S., Hajkova, V., Chalupsky, J., Kuba, J., Tschentscher, T., Toleikis, S., Düsterer, S. & Redlin, H. Ablation of solids using a femtosecond extreme ultraviolet free electron laser. *Appl. Phys. Lett.* **89,** 89–91 (2006) (cit. on pp. 16, 68).
55. Hau-Riege, S. P., London, R. A., Bionta, R. M., McKernan, M. A., Baker, S. L., Krzywinski, J., Sobierajski, R., Nietubyc, R., Pelka, J. B., Jurek, M., Juha, L., Chalupsky, J., Cihelka, J., Hájková, V., Velyhan, A., Krása, J., Kuba, J., Tiedtke, K., Toleikis, S., Tschentscher, T., Wabnitz, H., Bergh, M., Caleman, C., Sokolowski-Tinten, K., Stojanovic, N. & Zastrau, U. Damage threshold of inorganic solids under free-electron-laser irradiation at 32.5 nm wavelength. *Appl. Phys. Lett.* **90,** 46–48 (2007) (cit. on p. 16).
56. Büttner, F. Topological mass of magnetic Skyrmions probed by ultrafast dynamic imaging. *PhD Thesis* (2013) (cit. on p. 19).
57. Tseng, A. Recent developments in micromilling using focused ion beam technology. *J. Micromechanics Microengineering* **14,** R15–R34 (2004) (cit. on p. 20).
58. Ziegler, J. F., Ziegler, M. D. & Biersack, J. P. SRIM - The stopping and range of ions in matter (2010). *Nucl. Instruments Methods Phys. Res. Sect. B Beam Interact. with Mater. Atoms* **268,** 1818–1823 (2010) (cit. on p. 20).
59. Paganin, D. *Coherent X-Ray Optics* (Oxford University Press, 2006) (cit. on p. 21).

60. Moshammer, R., Jiang, Y. H., Foucar, L., Rudenko, A., Ergler, T., Schröter, C. D., Lüdemann, S., Zrost, K., Fischer, D., Titze, J., Jahnke, T., Schöffler, M., Weber, T., Dörner, R., Zouros, T. J. M., Dorn, A., Ferger, T., Kühnel, K. U., Düsterer, S., Treusch, R., Radcliffe, P., Plönjes, E. & Ullrich, J. Few-photon multiple ionization of Ne and Ar by strong free-electron-laser pulses. *Phys. Rev. Lett.* **98,** 1–4 (2007) (cit. on p. 27).

61. Nagler, B., Zastrau, U., Fäustlin, R. R., Vinko, S. M., Whitcher, T., Nelson, a. J., Sobierajski, R., Krzywinski, J., Chalupsky, J., Abreu, E., Bajt, S., Bornath, T., Burian, T., Chapman, H., Cihelka, J., Döppner, T., Düsterer, S., Dzelzainis, T., Fajardo, M., Förster, E., Fortmann, C., Galtier, E., Glenzer, S. H., Göde, S., Gregori, G., Hajkova, V., Heimann, P., Juha, L., Jurek, M., Khattak, F. Y., Khorsand, A. R., Klinger, D., Kozlova, M., Laarmann, T., Lee, H. J., Lee, R. W., Meiwes-Broer, K.-H., Mercere, P., Murphy, W. J., Przystawik, A., Redmer, R., Reinholz, H., Riley, D., Röpke, G., Rosmej, F., Saksl, K., Schott, R., Thiele, R., Tiggesbäumker, J., Toleikis, S., Tschentscher, T., Uschmann, I., Vollmer, H. J. & Wark, J. S. Turning solid aluminium transparent by intense soft X-ray photoionization. *Nat. Phys.* **5,** 693–696 (2009) (cit. on pp. 27, 85, 90, 101, 102).

62. Janicijevic, L. Diffraction of Gaussian beams through different types of zone plates. *J. Opt.* **18,** 23–42 (1987) (cit. on p. 27).

63. Thompson, A. C., Attwood, D. T., Gullikson, E. M., Howells, M. R., Kortright, J. B., Robinson, A. L., Underwood, J. H., Kim, K.-J., Kirz, J., Lindau, I., Pianetta, P., Winick, H., Williams, G. P. & Scofield, J. H. *X-ray Data Booklet* 2nd ed. (Center for X-ray Optics and Advanced Light Source, Berkeley, 2001) (cit. on p. 32).

64. Miedema, P. S., Quevedo, W. & Fondell, M. The variable polarization undulator beamline UE52 SGM at BESSY II. *J. large-scale Res. Facil. JLSRF* **2,** A70 (2016) (cit. on p. 46).

65. Huang, J.-S., Callegari, V., Geisler, P., Brüning, C., Kern, J., Prangsma, J. C., Wu, X., Feichtner, T., Ziegler, J., Weinmann, P., Kamp, M., Forchel, A., Biagioni, P., Sennhauser, U. & Hecht, B. Atomically flat single-crystalline gold nanostructures for plasmonic nanocircuitry. *Nat. Commun.* **1,** 150. arXiv: `1004.1961` (2010) (cit. on p. 46).

66. Keskinbora, K., Grévent, C., Bechtel, M., Weigand, M., Goering, E., Nadzeyka, A., Peto, L., Rehbein, S., Schneider, G., Follath, R., Vila-Comamala, J., Yan, H. & Schütz, G. Ion beam lithography for Fresnel zone plates in X-ray microscopy. *Opt. Express* **21,** 11747–11756 (2013) (cit. on p. 47).

67. Mayer, M., Grévent, C., Szeghalmi, A., Knez, M., Weigand, M., Rehbein, S., Schneider, G., Baretzky, B. & Schütz, G. Multilayer Fresnel zone plate for soft X-ray microscopy resolves sub-39nm structures. *Ultramicroscopy* **111,** 1706–1711 (2011) (cit. on p. 47).

68. Mohacsi, I., Vartiainen, I., Rösner, B., Guizar-Sicairos, M., Guzenko, V. A., McNulty, I., Winarski, R., Holt, M. V. & David, C. Interlaced zone plate optics for hard X-ray imaging in the 10 nm range. *Sci. Rep.* **7,** 43624 (2017) (cit. on p. 55).

69. Roseker, W., Franz, H., Schulte-Schrepping, H., Ehnes, A., Leupold, O., Zontone, F., Lee, S., Robert, A. & Grübel, G. Development of a hard X-ray delay line for X-ray photon correlation spectroscopy and jitter-free pump–probe experiments at X-ray free-electron laser sources. *J. Synchrotron Radiat.* **18,** 481–491 (2011) (cit. on p. 55).

70. Osaka, T., Hirano, T., Sano, Y., Inubushi, Y., Matsuyama, S., Tono, K., Ishikawa, T., Yamauchi, K. & Yabashi, M. Wavelength-tunable split-and-delay optical system for hard X-ray free-electron lasers. *Opt. Express* **24,** 9187 (2016) (cit. on p. 55).

71. Mastrangelo, C. H., Tai, Y.-C. & Muller, R. S. Thermophysical properties of low-residual stress, Silicon-rich, LPCVD silicon nitride films. *Sensors Actuators A Phys.* **23,** 856–860 (1990) (cit. on p. 60).

72. Barkusky, F., Bayer, A., Döring, S., Grossmann, P. & Mann, K. Damage threshold measurements on EUV optics using focused radiation from a table-top laser produced plasma source. *Opt. Express* **18,** 4346–55 (2010) (cit. on p. 68).

73. Li, C. H. & Lee, C. K. Minimum cross entropy thresholding. *Pattern Recognit.* **26,** 617–625 (1993) (cit. on p. 70).

74. Li, C. H. & Tam, P. K. An iterative algorithm for minimum cross entropy thresholding. *Pattern Recognit. Lett.* **19,** 771–776 (1998) (cit. on p. 70).

75. Kortright, J. B. Resonant soft X-ray and extreme ultraviolet magnetic scattering in nanostructured magnetic materials: Fundamentals and directions. *J. Electron Spectros. Relat. Phenomena* **189,** 178–186 (2013) (cit. on p. 75).

76. Koopmans, B., Malinowski, G., Dalla Longa, F., Steiauf, D., Fähnle, M., Roth, T., Cinchetti, M. & Aeschlimann, M. Explaining the paradoxical diversity of ultrafast laser-induced demagnetization. *Nat. Mater.* **9,** 259–265 (2010) (cit. on pp. 75, 77).

77. Moisan, N., Malinowski, G., Mauchain, J., Hehn, M., Vodungbo, B., Lüning, J., Mangin, S., Fullerton, E. E. & Thiaville, a. Investigating the role of superdiffusive currents in laser induced demagnetization of ferromagnets with nanoscale magnetic domains. *Sci. Rep.* **4,** 4658 (2014) (cit. on pp. 75, 77, 84).

78. Pfau, B., Schaffert, S., Müller, L., Gutt, C., Al-Shemmary, A., Büttner, F., Delaunay, R., Düsterer, S., Flewett, S., Frömter, R., Geilhufe, J., Guehrs, E., Günther, C. M., Hawaldar, R., Hille, M., Jaouen, N., Kobs, A., Li, K., Mohanty, J., Redlin, H., Schlotter, W. F., Stickler, D., Treusch, R., Vodungbo, B., Kläui, M., Oepen, H. P., Lüning, J., Grübel, G. & Eisebitt, S. Ultrafast optical demagnetization manipulates nanoscale spin structure in domain walls. *Nat. Commun.* **3** (2012) (cit. on pp. 75, 77, 84).

79. Battiato, M., Carva, K. & Oppeneer, P. M. Superdiffusive Spin Transport as a Mechanism of Ultrafast Demagnetization. *Phys. Rev. Lett.* **105,** 027203. arXiv: `1106.2117` (2010) (cit. on p. 75).
80. Zhang, G. P., Bai, Y. & George, T. F. Energy- and crystal momentum-resolved study of laser-induced femtosecond magnetism. *Phys. Rev. B* **80,** 214415 (2009) (cit. on p. 75).
81. Fähnle, M. & Illg, C. Electron theory of fast and ultrafast dissipative magnetization dynamics. *J. Phys. Condens. Matter* **23,** 493201 (2011) (cit. on p. 75).
82. Gražulis, S., Chateigner, D., Downs, R. T., Yokochi, A. F. T., Quirós, M., Lutterotti, L., Manakova, E., Butkus, J., Moeck, P. & Le Bail, A. Crystallography Open Database – an open-access collection of crystal structures. *J. Appl. Crystallogr.* **42,** 726–729 (2009) (cit. on p. 76).
83. Boeglin, C., Beaurepaire, E., Halté, V., López-Flores, V., Stamm, C., Pontius, N., Dürr, H. A. & Bigot, J. Y. Distinguishing the ultrafast dynamics of spin and orbital moments in solids. *Nature* **465,** 458–461 (2010) (cit. on p. 82).
84. Mitzner, R., Sorokin, A. A., Siemer, B., Roling, S., Rutkowski, M., Zacharias, H., Neeb, M., Noll, T., Siewert, F., Eberhardt, W., Richter, M., Juranic, P., Tiedtke, K. & Feldhaus, J. Direct autocorrelation of soft-x-ray free-electron-laser pulses by time-resolved two-photon double ionization of He. *Phys. Rev. A* **80,** 025402 (2009) (cit. on p. 84).
85. Ferrari, E., Spezzani, C., Fortuna, F., Delaunay, R., Vidal, F., Nikolov, I., Cinquegrana, P., Diviacco, B., Gauthier, D., Penco, G., Ribic, P. R., Roussel, E., Trovo, M., Moussy, J. B., Pincelli, T., Lounis, L., Manfredda, M., Pedersoli, E., Capotondi, F., Svetina, C., Mahne, N., Zangrando, M., Raimondi, L., Demidovich, A., Giannessi, L., De Ninno, G., Danailov, M. B., Allaria, E. & Sacchi, M. Widely tunable two-colour seeded free-electron laser source for resonant-pump resonant-probe magnetic scattering. *Nat. Commun.* **7,** 1–8 (2016) (cit. on p. 84).
86. Stöhr, J. & Scherz, A. O. Creation of X-Ray Transparency of Matter by Stimulated Elastic Forward Scattering. *Phys. Rev. Lett.* **115,** 107402. arXiv: `1504.04544` (2015) (cit. on p. 85).
87. Campbell, J. & Papp, T. Widths of the atomic K-N7 levels. *At. Data Nucl. Data Tables* **77,** 1–56 (2001) (cit. on p. 89).
88. Hatada, K. & Di Cicco, A. Modeling saturable absorption for ultra short X-ray pulses. *J. Electron Spectros. Relat. Phenomena* **196,** 177–180 (2014) (cit. on p. 90).
89. Schneider, M., Pfau, B., Günther, C. M., Capotondi, F. & von Korff Schmising, C. Self-normalizing, simultaneous measurement of fluence-dependent absorption and diffraction in a single FEL shot. *Beamtime Appl. FLASH2* (2017) (cit. on p. 101).

90. Mincigrucci, R., Bencivenga, F., Capotondi, F., Principi, E., Giangrisostomi, E., Battistoni, A., Caputo, M., Casolari, F., Gessini, A., Manfredda, M., Pedersoli, E. & Masciovecchio, C. Role of the ionization potential in nonequilibrium metals driven to absorption saturation. *Phys. Rev. E* **92,** 011101 (2015) (cit. on p. 101).

List of own publications

. Schneider, M., Günther, C. M., Pfau, B., Capotondi, F., Manfredda, M., Zangrando, M., Mahne, N., Raimondi, L., Pedersoli, E., Naumenko, D. & Eisebitt, S. In situ single-shot diffractive fluence mapping for X-ray free-electron laser pulses. *Nat. Commun.* **9,** 214. arXiv: `1705.03814` (2018).

. Vidas, L., Günther, C. M., Miller, T. A., Pfau, B., Perez-Salinas, D., Martínez, E., Schneider, M., Gührs, E., Gargiani, P., Valvidares, M., Marvel, R. E., Hallman, K. A., Haglund, R. F., Eisebitt, S. & Wall, S. Imaging Nanometer Phase Coexistence at Defects During the Insulator–Metal Phase Transformation in VO 2 Thin Films by Resonant Soft X-ray Holography. *Nano Lett.* acs.nanolett.8b00458 (2018).

. Büttner, F., Lemesh, I., Schneider, M., Pfau, B., Günther, C. M., Hessing, P., Geilhufe, J., Caretta, L., Engel, D., Krüger, B., Viefhaus, J., Eisebitt, S. & Beach, G. S. D. Field-free deterministic ultrafast creation of magnetic skyrmions by spin–orbit torques. *Nat. Nanotechnol.* **12,** 1040–1044 (2017).

. Fohler, M., Frömmel, S., Schneider, M., Pfau, B., Günther, C. M., Hennecke, M., Guehrs, E., Shemilt, L., Mishra, D., Berger, D., Selve, S., Mitin, D., Albrecht, M. & Eisebitt, S. A general approach to obtain soft x-ray transparency for thin films grown on bulk substrates. *Rev. Sci. Instrum.* **88,** 103701 (2017).

. Guehrs, E., Schneider, M., Günther, C. M., Hessing, P., Heitz, K., Wittke, D., López-Serrano Oliver, A., Jakubowski, N., Plendl, J., Eisebitt, S. & Haase, A. Quantification of silver nanoparticle uptake and distribution within individual human macrophages by FIB/SEM slice and view. *J. Nanobiotechnology* **15,** 1–11 (2017).

. Günther, C. M., Guehrs, E., Schneider, M., Pfau, B., Von Korff Schmising, C., Geilhufe, J., Schaffert, S. & Eisebitt, S. Experimental evaluation of signal-to-noise in spectro-holography via modified uniformly redundant arrays in the soft x-ray and extreme ultraviolet spectral regime. *J. Opt. (United Kingdom)* **19** (2017).

. von Korff Schmising, C., Weder, D., Noll, T., Pfau, B., Hennecke, M., Strüber, C., Radu, I., Schneider, M., Staeck, S., Günther, C. M., Lüning, J., el dine Merhe, A., Buck, J., Hartmann, G., Viefhaus, J., Treusch, R. & Eisebitt, S. Generating circularly polarized radiation in the extreme ultraviolet spectral range at the free-electron laser FLASH. *Rev. Sci. Instrum.* **88,** 053903 (2017).

. Willems, F., von Korff Schmising, C., Weder, D., Günther, C. M., Schneider, M., Pfau, B., Meise, S., Guehrs, E., Geilhufe, J., Merhe, A. E. D., Jal, E., Vodungbo, B., Lüning, J., Mahieu, B., Capotondi, F., Pedersoli, E., Gauthier, D., Manfredda,

M. & Eisebitt, S. Multi-color imaging of magnetic Co/Pt heterostructures. *Struct. Dyn.* **4,** 014301 (2017).

. Hessing, P., Pfau, B., Guehrs, E., Schneider, M., Shemilt, L., Geilhufe, J. & Eisebitt, S. Holography-guided ptychography with soft X-rays. *Opt. Express* **24,** 1840 (2016).

. Schneider, M., Günther, C. M., von Korff Schmising, C., Pfau, B. & Eisebitt, S. Curved gratings as an integrated photon fluence monitor in x-ray transmission scattering experiments. *Opt. Express* **24,** 13091 (2016).

. Vodungbo, B., Tudu, B., Perron, J., Delaunay, R., Müller, L., Berntsen, M. H., Grübel, G., Malinowski, G., Weier, C., Gautier, J., Lambert, G., Zeitoun, P., Gutt, C., Jal, E., Reid, A. H., Granitzka, P. W., Jaouen, N., Dakovski, G. L., Moeller, S., Minitti, M. P., Mitra, A., Carron, S., Pfau, B., Von Korff Schmising, C., Schneider, M., Eisebitt, S. & Lüning, J. Indirect excitation of ultrafast demagnetization. *Sci. Rep.* **6,** 1–9 (2016).

. von Korff Schmising, C., Pfau, B., Schneider, M., Günther, C. M., Weder, D., Willems, F., Geilhufe, J., Malm, E., Müller, L., Vodungbo, B., Capotondi, F., Pedersoli, E., Manfredda, M., Lüning, J. & Eisebitt, S. Imaging Non-Local Magnetization Dynamics. *Synchrotron Radiat. News* **29,** 26–31 (2016).

. Bergeard, N., Schaffert, S., López-Flores, V., Jaouen, N., Geilhufe, J., Günther, C. M., Schneider, M., Graves, C., Wang, T., Wu, B., Scherz, A. O., Baumier, C., Delaunay, R., Fortuna, F., Tortarolo, M., Tudu, B., Krupin, O., Minitti, M. P., Robinson, J., Schlotter, W. F., Turner, J. J., Lüning, J., Eisebitt, S. & Boeglin, C. Irreversible transformation of ferromagnetic ordered stripe domains in single-shot infrared-pump/resonant-x-ray-scattering-probe experiments. *Phys. Rev. B* **91,** 054416. arXiv: `1502.0786` (2015).

. Büttner, F., Moutafis, C., Schneider, M., Krüger, B., Günther, C. M., Geilhufe, J., Schmising, C. v. K., Mohanty, J., Pfau, B., Schaffert, S., Bisig, A., Foerster, M., Schulz, T., Vaz, C. A. F., Franken, J. H., Swagten, H. J. M., Kläui, M. & Eisebitt, S. Dynamics and inertia of skyrmionic spin structures. *Nat. Phys.* **11,** 225–228 (2015).

. Guehrs, E., Fohler, M., Frömmel, S., Günther, C. M., Hessing, P., Schneider, M., Shemilt, L. & Eisebitt, S. Mask-based dual-axes tomoholography using soft x-rays. *New J. Phys.* **17** (2015).

. Geilhufe, J., Pfau, B., Schneider, M., Büttner, F., Günther, C. M., Werner, S., Schaffert, S., Guehrs, E., Frömmel, S., Kläui, M. & Eisebitt, S. Monolithic focused reference beam X-ray holography. *Nat. Commun.* **5,** 1–6 (2014).

. von Korff Schmising, C., Pfau, B., Schneider, M., Günther, C. M., Giovannella, M., Perron, J., Vodungbo, B., Müller, L., Capotondi, F., Pedersoli, E., Mahne, N., Lüning, J. & Eisebitt, S. Imaging Ultrafast Demagnetization Dynamics after a Spatially Localized Optical Excitation. *Phys. Rev. Lett.* **112,** 217203 (2014).

. Büttner, F., Moutafis, C., Bisig, A., Wohlhüter, P., Günther, C. M., Mohanty, J., Geilhufe, J., Schneider, M., Korff Schmising, C. V., Schaffert, S., Pfau, B., Hantschmann, M., Riemeier, M., Emmel, M., Finizio, S., Jakob, G., Weigand, M., Rhensius, J., Franken, J. H., Lavrijsen, R., Swagten, H. J. M., Stoll, H., Eisebitt, S. & Kläui, M. Magnetic states in low-pinning high-anisotropy material nanostructures suitable for dynamic imaging. *Phys. Rev. B* **87,** 134422 (2013).

. Büttner, F., Schneider, M., Günther, C. M., Vaz, C. A. F., Lägel, B., Berger, D., Selve, S., Kläui, M. & Eisebitt, S. Automatable sample fabrication process for pump-probe X-ray holographic imaging. *Opt. Express* **21,** 30563 (2013).

. Müller, L., Schleitzer, S., Gutt, C., Pfau, B., Schaffert, S., Geilhufe, J., von Korff Schmising, C., Schneider, M., Günther, C. M., Büttner, F., Capotondi, F., Pedersoli, E., Düsterer, S., Redlin, H., Al-Shemmary, A., Treusch, R., Bach, J., Frömter, R., Vodungbo, B., Gautier, J., Zeitoun, P., Popescu, H., Lopez-Flores, V., Beaulieu, N., Sirotti, F., Jaouen, N., Malinowski, G., Tudu, B., Li, K., Lüning, J., Oepen, H. P., Kiskinova, M., Eisebitt, S. & Grübel, G. Ultrafast Dynamics of Magnetic Domain Structures Probed by Coherent Free-Electron Laser Light. *Synchrotron Radiat. News* **26,** 27–32 (2013).

. Schaffert, S., Pfau, B., Geilhufe, J., Günther, C. M., Schneider, M., Korff Schmising, C. V. & Eisebitt, S. High-resolution magnetic-domain imaging by Fourier transform holography at 21 nm wavelength. *New J. Phys.* **15** (2013).